

ISSN 0038-531X

Russian Original Vol. 59, No. 5, November, 1985

May, 1986

SATEAZ 59(5) 877-956 (1985)

SOVIET ATOMIC ENERGY

АТОМНАЯ ЭНЕРГИЯ
(ATOMNAYA ÉNERGIYA)

TRANSLATED FROM RUSSIAN



CONSULTANTS BUREAU, NEW YORK

SOVIET ATOMIC ENERGY

Soviet Atomic Energy is abstracted or indexed in *Chemical Abstracts*, *Chemical Titles*, *Pollution Abstracts*, *Science Research Abstracts*, *Parts A and B*, *Safety Science Abstracts Journal*, *Current Contents*, *Energy Research Abstracts*, and *Engineering Index*.

Soviet Atomic Energy is a translation of *Atomnaya Energiya*, a publication of the Academy of Sciences of the USSR.

An agreement with the Copyright Agency of the USSR (VAAP) makes available both advance copies of the Russian journal and original glossy photographs and artwork. This serves to decrease the necessary time lag between publication of the original and publication of the translation and helps to improve the quality of the latter. The translation began with the first issue of the Russian journal.

Editorial Board of *Atomnaya Energiya*:

Editor: O. D. Kazachkovskii

Associate Editors: A. I. Artemov, N. N. Ponomarev-Stepnoi, and N. A. Vlasov

I. A. Arkhangel'skii

I. V. Chuvilo

I. Ya. Emel'yanov

I. N. Golovin

V. I. Il'ichev

P. L. Kirillov

Yu. I. Koryakin

E. V. Kulov

B. N. Laskorin

V. V. Matveev

A. M. Petras'yants

E. P. Ryazantsev

A. S. Shtan

B. A. Sidorenko

Yu. V. Sivintsev

M. F. Troyano

V. A. Tsykanov

E. I. Vorob'ev

V. F. Zelenskii

Copyright © 1986, Plenum Publishing Corporation. *Soviet Atomic Energy* participates in the Copyright Clearance Center (CCC) Transactional Reporting Service. The appearance of a code line at the bottom of the first page of an article in this journal indicates the copyright owner's consent that copies of the article may be made for personal or internal use. However, this consent is given on the condition that the copier pay the flat fee of \$9.50 per article (no additional per-page fees) directly to the Copyright Clearance Center, Inc., 27 Congress Street, Salem, Massachusetts 01970, for all copying not explicitly permitted by Sections 107 or 108 of the U.S. Copyright Law. The CCC is a nonprofit clearinghouse for the payment of photocopying fees by libraries and other users registered with the CCC. Therefore, this consent does not extend to other kinds of copying, such as copying for general distribution, for advertising or promotional purposes, for creating new collective works, or for resale, nor to the reprinting of figures, tables, and text excerpts. 0038-531X/85/\$09.50

Consultants Bureau journals appear about six months after the publication of the original Russian issue. For bibliographic accuracy, the English issue published by Consultants Bureau carries the same number and date as the original Russian from which it was translated. For example, a Russian issue published in December will appear in a Consultants Bureau English translation about the following June, but the translation issue will carry the December date. When ordering any volume or particular issue of a Consultants Bureau journal, please specify the date and, where applicable, the volume and issue numbers of the original Russian. The material you will receive will be a translation of that Russian volume or issue.

Subscription (2 volumes per year)

Vols. 58 & 59: \$645 (domestic); \$715 (foreign)

Vols. 60 & 61: \$695 (domestic); \$770 (foreign)

Single Issue: \$100

Single Article: \$9.50

CONSULTANTS BUREAU, NEW YORK AND LONDON



233 Spring Street
New York, New York 10013

Published monthly. Second-class postage paid at Jamaica, New York 11431.

Mailed in the USA by Publications Expediting, Inc., 200 Meacham Avenue, Elmont, NY 11003.

POSTMASTER: Send address changes to *Soviet Atomic Energy*, Plenum Publishing Corporation, 233 Spring Street, New York, NY 10013.

SOVIET ATOMIC ENERGY

A translation of *Atomnaya Énergiya*

May, 1986

Volume 59, Number 5

November, 1985

CONTENTS

Engl./Russ.

ARTICLES

Calculating the Startup-Sensor Readings of the Control and Safety System of a BN-600 Reactor on the Basis of Simultaneous Solution of the Direct and Conjugate Neutron-Transfer Equations — V. I. Usanov and V. V. Korobeinikov.....	877	323
Acoustic Noise from Steam Generators in the BOR-60 Reactor during Simulation of Leaks by Argon and Steam — V. M. Sokolov, V. V. Golushko, V. A. Afanas'ev, Yu. P. Grebenkin, and A. B. Muralev.....	882	327
Anisotropic Turbulent Heat Transfer in Channels of Nuclear Power Reactors — V. P. Bobkov.....	886	330
Prompt Neutrons from the Low-Energy Fission of Atomic Nuclei — B. F. Gerasimenko and V. A. Rubchenya.....	893	335
Measurement of the Fast-Neutron Fission Cross Sections of ^{231}Pa and ^{243}Am — B. I. Fursov, E. Yu. Baranov, M. P. Klemyshev, B. F. Samylin, G. N. Smirenkin, and Yu. M. Turchin.....	899	339
Measurement of the Mean-Energy Differences in the Fission-Neutron Spectra of ^{233}U , ^{235}U , ^{239}Pu , and ^{252}Cf — V. I. Vol'shov and G. N. Smirenkin.....	903	343
Study of the Changes in the Electrical Resistivity and Microhardness of Vanadium and Niobium Under Separate and Successive Irradiation with Neutrons, α -Particles, and Electrons — P. K. Khabibullaev, T. B. Ashrapov, A. K. Kakabadze, I. M. Neklyudov, V. N. Tkach, A. I. Fedorenko, Kh. R. Yunusov, and V. A. Yamnitskii.....	906	345
Model of Fission-Product Diffusion in the Cores of Fuel Microassemblies — V. I. Arkhipov, A. N. Gudkov, V. A. Kashparov, V. M. Kolobashkin, M. A. Koptev, A. A. Kotlyarov, V. M. Login, and A. I. Rudenko.....	909	348
Contribution of Dislocation Creep to the Radiational Creep of Materials — V. A. Borodin and A. I. Ryazanov	912	350
A Comparative Study of the Corrosion Resistance of an Austenitic Steel in Lithium and the Eutectic Lead-Lithium Alloy — G. M. Gryaznov, V. A. Evtikhin, L. P. Zavyal'skii, A. Ya. Kosukhin, I. E. Lyublinskii, N. V. Samsonov, and A. A. Gusakov.....	918	355
Materialogical Aspects Related to the Application of Lithium in the Thermonuclear Reactor Blankets — G. M. Gryaznov, L. G. Golubchikov, V. A. Evtikhin, L. P. Zavyal'skii, A. Ya. Kosukhin, and I. E. Lyublinskii.....	922	358
Thermodynamics of the Interaction of UO_2 with Carbon in the Presence of the Additives Al_2O_3 , SiO_2 , SiC , and UC_2 — Yu. F. Khromov, D. E. Svistunov, and S. A. Zhmurov.....	928	363
Determination of the Temperature Dependence of the Demixing of an Emulsion — S. M. Karpacheva, T. N. Shepeleva, and S. N. Mel'nikova.....	933	366

(continued)

Engl./Russ.

Radiation Decomposition of Surface-Active Substances in Aqueous Solutions — M. V. Vladimirova, V. P. Kermanov, I. A. Kulikov, and M. N. Maslova.....	936	368
Hybrid Radiation Background Monitoring in Operational Control and Forecasting of Environmental Contamination by Nuclear Power Station Discharges — I. S. Ereemeev, V. A. Eremenko, V. S. Zhernov, Yu. A. Makarov, V. V. Matveev, N. V. Ryzhov, V. V. Ryazanov, and V. M. Skatkin.....	938	370
Characteristics of the Propagation in the Ground Layer of the Atmosphere of the Radionuclides Emitted During the Regeneration of Fuel Elements — I. N. Ruzhentsova, R. V. Semova, E. N. Teverovskii, and I. A. Ternovskii.....	941	373
LETTERS TO THE EDITOR		
Possibility of Determining Nuclear-Fuel Characteristics by Mass Spectrometry without Chemical Separation of the Elements — V. V. Kalygin, V. Ya. Gabeskiriya, and V. I. Borisenkov.....	945	378
System of Computation of the Reactivity Balance for the BOR-60 Reactor — V. N. Efimov, S. N. Eshchenko, V. A. Kachalin, A. S. Nikol'skii, and V. N. Pridachin.....	947	379
Influence of Neutrons on the Rotation of the Polarization Plane of Quartz — I. Kh. Abdukadyrova.....	950	381
Plutonium Content of Soils in the Soviet Union — F. I. Pavlotskaya, Z. M. Fedorova, V. V. Emel'yanov, B. F. Myasoedov, and I. G. Vodovozova.....	952	382
TLD Monitoring of Emergency Gaseous Fission Product Discharges from Nuclear Power Plants — I. A. Bochvar, T. I. Gimadova, A. A. Drozdov, I. B. Keirim-Markus, V. A. Kiyazev, and N. A. Sergeeva.....	954	383

The Russian press date (podpisano k pechati) of this issue was 11/5/1985. Publication therefore did not occur prior to this date, but must be assumed to have taken place reasonably soon thereafter.

CALCULATING THE STARTUP-SENSOR READINGS OF THE CONTROL AND SAFETY
SYSTEM OF A BN-600 REACTOR ON THE BASIS OF SIMULTANEOUS SOLUTION
OF THE DIRECT AND CONJUGATE NEUTRON-TRANSFER EQUATIONS

V. I. Usanov and V. V. Korobeinikov

UDC 621.039.51.15:
621.039.526

To monitor the neutron flux in the course of fuel-assembly loading and physical investigations and also for emergency protection in all stages of physical startup in a BN-600 reactor, provision is made for an additional set of startup equipment (ASSE). In its operational state, the detector unit of the ASSE is established under the sodium level in a hermetic steel chest which passes through the rotatable sample in an eccentric manner relative to the vertical axis of the reactor and is cooled by air to a temperature of $\sim 80^\circ\text{C}$ (Fig. 1).

The location, construction, and composition of the sensors in the unit are chosen so as to take account of the theoretical characteristics of the neutron field. The theoretical dependence of the detector count on the number of fuel assemblies is used to analyze experimental methods of bringing the reactor to critical conditions and to write physical-investigation programs.

Reliable prediction of the startup-sensor readings of the control and safety system is complicated by a number of factors: the complex three-dimensional geometry of the calcula-

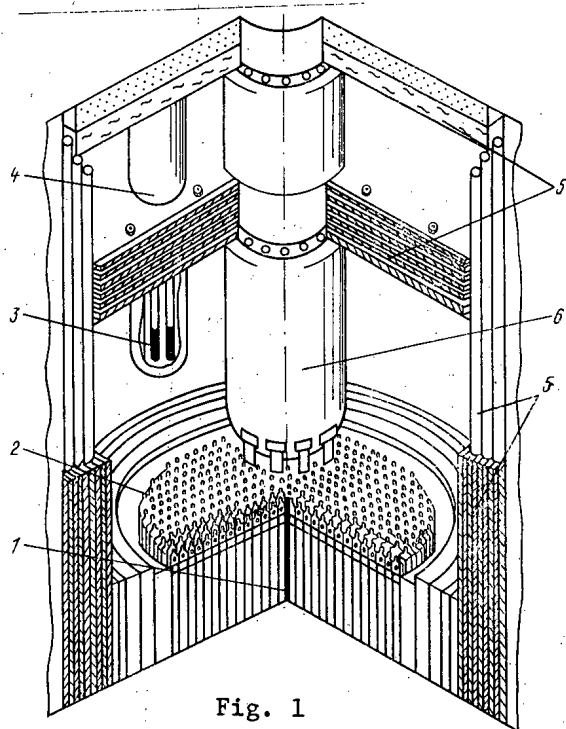


Fig. 1

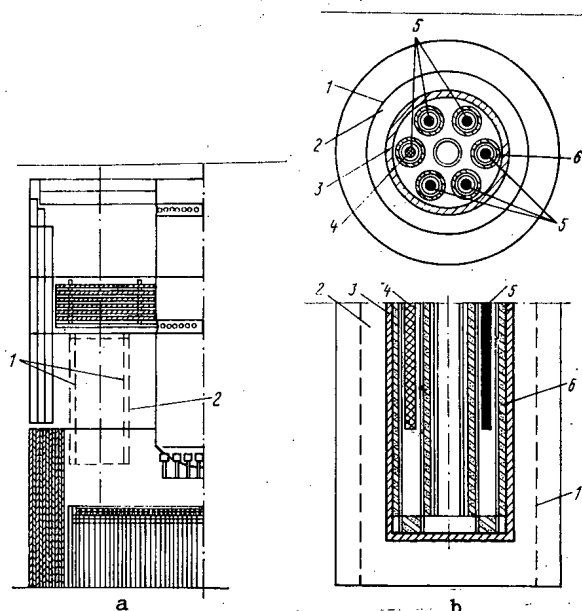


Fig. 2

Fig. 1. Position of ASSE detector unit in BN-600 reactor: 1) actuating source; 2) fuel-assembly simulators, which may be dismantled on loading the reactor with the regular fuel assemblies; 3) detector unit; 4) hermetic steel chamber; 5) shielding; 6) central column of control and safety system.

Fig. 2. Calculation region for direct (a) and conjugate (b) problems: 1) surface-integration contour; 2) sodium boundary layer; 3) steel chamber; 4) conjugate source; 5) sensors; 6) moderator.

Translated from *Atomnaya Énergiya*, Vol. 59, No. 5, pp. 323-327, November, 1985. Original article submitted January 25, 1985.

In addition, it would be impossible to produce a full-scale experimental model. In these conditions, a theoretical-experimental approach is used; the basic concept is to calculate the neutron field at the sensor location and determine experimentally the correction coefficients for the perturbation of the field by the detector unit itself. This approach is widely used to determine the neutron-physics characteristics of key reactor components, including sensors in the control and safety system, both in the Soviet Union and elsewhere [1, 2].

Calculations taking account of modeling of startup sensors of the BN-600 reactor on the BFS-2 teststand [3] gave underestimates of the sensor reading by a factor of approximately 3-4 in comparison with measurements obtained in startup [4].* Although these discrepancies did not require modification of the apparatus and movement of the sensors over the height, the power of the expensive startup source could be reduced by a factor of 2-3 with more precise calculation.

In the present work, an attempt is made to improve the quality of calculation of ASSE sensor readings using a trend that has developed in perturbation theory [5-8]. The general idea is the same as in the theoretical-experimental approach, i.e., to split the complex initial problem into two simpler problems: calculation of the reactor without a detector unit (unperturbed problem) and calculation of the detector unit, regarded as a perturbation, separately from the reactor (Fig. 2).

The distinctive feature of the second problem is that retaining simple boundary conditions entails solving not the direct but the conjugate transfer equation. The detector readings in each of six measuring channels are estimated from the formula

$$N_k = - \int dv \oint dr_F \left(n \frac{v}{|v|} \right) \varphi(r_F, v) \varphi_k^+(r_F, v), \quad (1)$$

where k is the number of the measuring chamber; $\varphi(r_F, v)$, $\varphi^+(r_F, v)$ are the direct and conjugate neutron fluxes, with velocity v at point r on some general surface F surrounding the detector unit; n is the unit vector of the normal to F .

At present, this method has been used to calculate such functionals as the activation of the second-loop sodium in the design of a fast reactor at Clinch River [9], the dose from neutron radiation in the building above the lid of the FFTF reactor [7], the dose from γ radiation of a commercial fuel-reprocessing plant [10], and so on. Regrettably, there is practically no information on some important details of the method, such as the choice of an optimal integration contour, the accuracy of the method, the features of matching the different geometries, and so on. These problems were partially discussed in [8, 11], individual results of which are used in sensor calculation.

The direct problem (finding the distribution of neutron flux density in the volume above the reactor), taking account of the reactor symmetry and its large dimensions, has been solved according to the DD program [12] in the P_1 approximation and R - Z geometry, and the conjugate problem (finding the distribution of the pseudoneutron density around a complex detector unit) has been solved by the Monte Carlo method using an SMK-10 program [13]. In both cases, a 26-group system of constants is used [14].

The surface of integration F is chosen in the boundary region common to the direct and conjugate problems (Fig. 2a, b). Since it was established in [8] that neither the configuration of F nor its position in the boundary region affects the accuracy of the calculation, only those factors which are associated with the specifics of the programs employed will be considered.

Analysis of the general formula obtained from Eq. (1) on series expansion of the direct and conjugate fluxes in terms of spherical functions shows that, if the P_L approximation is used in the direct problem, attention may be confined to the first $L + 2$ moments of the expansion of the conjugate flux in integrating over the surface F , without loss of accuracy. Since the direct problem is solved in the P_1 approximation, taking the first three moments of the series expansion of the conjugate flux in terms of spherical functions is sufficient

*Results from direct calculation in P_1 approximation (in two- and one-dimensional geometry) appear even higher than the experimental results.

Declassified and Approved For Release 2013/02/20 : CIA-RDP10-02196R000300070005-0
in order to obtain an accurate result. The standard modification of the program permits the calculation of φ_0^+ and a special modification gives φ_1^* . Having decided to limit consideration to this approximation, the "working" conjugate formula obtained takes the form

$$N_h = \sum_{g=1}^{26} \oint dr_F [\varphi_0^{(g)}(n\varphi_{1,h}^{+(g)}) + \varphi_{0,h}^{+(g)}(n, \varphi_1^{(g)})], \quad (2)$$

where g is the number of the energy group; $\varphi_0^{(g)}, \varphi_{0,h}^{+(g)}$ is the complete group of direct and conjugate fluxes; $\varphi_1^{(g)}, \varphi_{1,h}^{+(g)}$ are the vectors of the direct and conjugate currents.

The program realizing the calculation of the sensor readings according to Eq. (2) with matching of R-Z geometry of the reactor and three-dimensional geometry of the sensor unit was written in Fortran for a BESM-6 computer. The data masses corresponding to the neutron fluxes and currents obtained from the DD program and the conjugate fluxes and currents from the SMK-10 program form the input. The basic elements of the program are a geometric unit for determining the coordinates of points on the matching surface, an interpolation unit which prepares the flux and current values at these points, and an integration unit performing calculation according to Eq. (2).

The neutron fluxes have been calculated for seven reactor loadings [15]. For three of them, the reactor is considered both with all the control rods immersed in the active zone and with the central rod and the emergency-protection rods withdrawn. The states investigated are chosen so that the rows of fuel assemblies are totally complete; the system of control rods consists of homogenized annular layers. One advantage of this approach is that, in order to calculate the sensor readings in the course of reactor loading, it is sufficient to introduce changes in the composition of the physical zones and simply recalculate the direct problem. Note one more simplifying factor. To obtain the sensor readings in each measuring channel, it is unnecessary to solve k conjugate equations. In view of the detector-

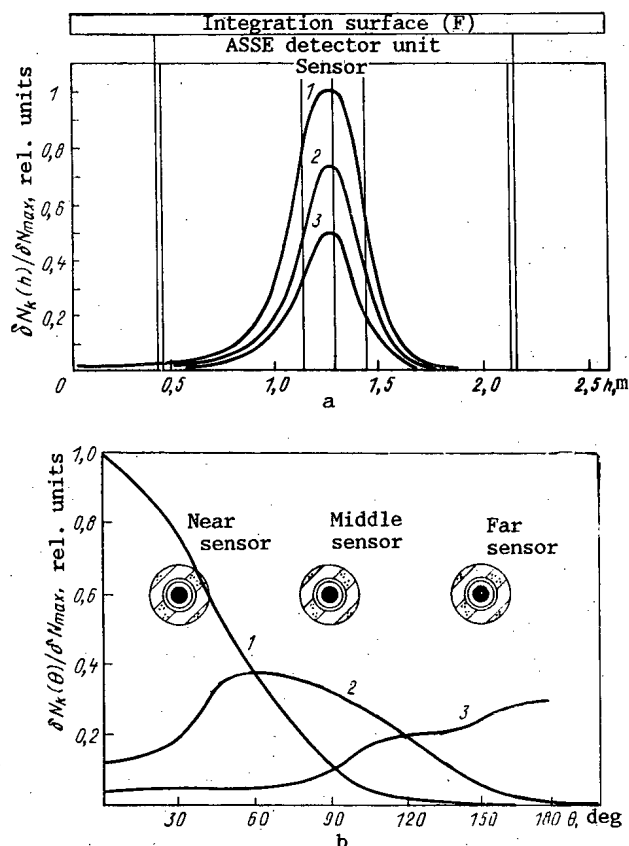


Fig. 3. Relative distribution of the contribution of individual sections of the surface to the readings over the height (a) and the azimuthal angle at the level of the center of the sensors (b); 1-3) near, middle, and far rows of sensors, respectively.

TABLE 1. Experimental and theoretical readings of counter channels during the loading of fuel assemblies in the active zone of the BN-600 reactor

Loading conditions	Counter readings, pulses/sec								
	near-source measuring channels			middle measuring channels			far measuring channels		
	N_e	N_t	$\frac{ N_t - N_e }{N_e} 100\%$	N_e	N_t	$\frac{ N_t - N_e }{N_e} 100\%$	N_e	N_t	$\frac{ N_t - N_e }{N_e} 100\%$
SNS; FA simulators; ILS	2502±2	2590	4	1643±3	1810	10	1184±2	1250	6
SNS; 46 FA, LEZ; ILS	4155±1	5380	29	2760±2	3680	33	1957±3	2640	35
SNS; 118 FA, LEZ; FA simulators; ILS	6839±1	7590	11	4682±3	5330	14	3293±3	3890	18
SNS; 148 FA; LEZ; FA simulators; ILS	7842±4	9410	20	5423±3	6680	23	3884±5	4820	24
SNS; 216 FA, LEZ; FA simulators; ILS	125 *±1	112 *	10	7414±9	8030	8	5298±5	5950	12
SNS; 216 FA, LEZ; 25 FA, HEZ	161 *±1	155 *	4	9549±5	10690	12	6962±5	8010	15
SNS; 216 FA, LEZ; 40 FA, HEZ; ILS	190 *±2	195 *	3	11390±7	12290	8	8334±9	9380	13

Note. SNS, startup neutron source; ILS, internal lateral screen; LEZ, low-enrichment zone; HEZ, high-enrichment zone; FA, fuel assembly.

unit symmetry, a conjugate source may be specified in only one of the channels and the readings of a particular sensor may be obtained by "turning" the rate field so that the conjugate source is in the required position with respect to the active zone. This permits one-time solution of the conjugate problem.

Thus, the variation in neutron field in the course of reactor loading is described by ten two-dimensional variants obtained from the DD program. On an EC-1060 computer, ~50 min is required to calculate one variant. To obtain the rate field in a single variant (with a standard deviation in group fluxes of ~5%) in a single variant calculated by the SMK-10 program on a BESM-6 computer, around 3-h machine time is required.

Table 1 gives the theoretical readings (N_t) and those recorded in the course of startup (N_e) [4] for ASSE sensors in assembling the critical mass of a BN-600 reactor with all the control rods immersed in the active zone. As is evident from Table 1, the discrepancy between the theoretical and experimental data is 3-35%, which satisfies the requirements imposed on the calculation accuracy for such systems. The results indicate the importance of correct description of the apparatus geometry and neutron-transfer effects, taking account of inhomogeneities in the ASSE detector unit. The best agreement of the theoretical and experimental results would hardly be expected because of indeterminacies in the intensity of the startup source and the sensitivity of the sensors, as well as constant and methodological errors. A somewhat greater discrepancy (30-40%) is obtained on withdrawing the control rods. In this case, the absorbing elements of the control system are in the path of the neutrons from the source to the sensor and a homogenized representation of the rod system in the form of annular layers in R-Z geometry overestimates the real screening action of the absorber. The theoretical value of the blocking factor is 0.5-0.6, as against the experimental value of 0.85.

The accuracy is higher for relative results of the calculations. Thus, the error in the nonuniformity coefficient of the detector count over the measuring channels is no more than 7%; the smoothing of the nonuniformity coefficient as fuel-assembly loading proceeds practically coincides with the experimental data. Better agreement is observed between the experimental and theoretical curves of the inverse multiplication for the case with inserted control rods.

Calculations not only allow the readings of each sensor to be obtained but also allow the features of neutron transfer to be estimated. This may be done simply by introducing the value of N_k on each section of surface F (δN_k) in Eq. (2) prior to the final integration over F . The relative distribution of the contribution of individual sections of F to the sensor

readings over the height and azimuthal angle at the level of the sensor center is shown in Fig. 3. As is evident from Fig. 3a, the determining contribution is observed in the section of the surface opposite the sensor. Beyond the limits of the detector unit, there is practically no leakage of the neutrons being recorded. Asymmetry of the neutron contributions to the sensor readings is observed over the height relative to the center of the detector height: neutrons passing through the lower part make a large contribution. The character of the contribution over the vertical is practically independent of the measuring channel in which the sensor is placed: near, middle, or far. The distribution over the azimuth is different, however (Fig. 3b). The maximum contribution for near and middle sensors is shifted from their centers toward the neutron source and for far sensors in the opposite direction. This indicates that the transfer of the neutrons making the basic contribution to the readings of the far row of sensors occurs through the rear wall of the steel tube in which they are placed, since the usual path — through the wall closer to the neutron source — is blocked by the effective absorption in the near sensors and the surrounding structures.

Distributions similar to those obtained may prove useful for directed variation in detector-unit structure with the aim of improving the efficiency of neutron-recording. To test a particular structural variant, only the conjugate problem need be recalculated here, which significantly reduces the bulk of optimizational investigations.

Thus, the method used to calculate the startup-sensor readings of the control and safety system of a BN-600 reactor allows the calculation scheme to be brought into closer agreement with the initial physical model than in the traditional approach and allows the resources of the DD and SMK-10 calculation programs to be more optimally distributed. As a result, not only economies of machine time are obtained, but there arises the possibility, in principle, of studying a complex inhomogeneous section of shielding using relatively limited computational means.

Comparison of the theoretical results with experimental data obtained in the course of BN-600 reactor startup confirms the practical applicability and efficiency of the method.

The given problem, together with the existing non-Soviet experience in calculating the functionals of shielding using "surface binding" of the solutions of the direct and conjugate equations, leads to the conclusion that it is expedient to include a matching program (with broad possibilities regarding methods of solution and geometries of the program units being matched) in packets of applied problems now being produced for the complex calculation of shielding.

It remains to thank M. F. Troyanov, E. I. Inyutin, and V. I. Savitskii, for useful discussions and also Yu. N. Mironovich and V. B. Polev for assistance in using the DD and SMK-10 programs.

LITERATURE CITED

1. N. I. Bugakov et al., in: Radiation Safety and Shielding of Atomic Power Plants [in Russian], No. 1, Atomizdat, Moscow (1975), p. 159.
2. F. B. Hemming and Dzh. U. Levellen, in: Radiation Safety and Shielding of Atomic Power Plants [in Russian], No. 5, Atomizdat, Moscow (1981), p. 183.
3. A. T. Bakov, et al., in: Abstracts of the Proceedings of the Second All-Union Conference on Protection against Ionizing Radiation [in Russian], Moscow (1978), p. 38.
4. E. I. Inyutin et al., in: Abstracts of the Proceedings of the Third All-Union Conference on Protection against Ionizing Radiation [in Russian], Tbilisi (1981), p. 131.
5. G. I. Marchuk and V. V. Orlov, in: Neutron Physics [in Russian], Atomizdat, Moscow (1961), p. 35.
6. G. Hansen and H. Sandmeier, Nucl. Sci. Eng., 22, 315 (1965).
7. M. Williams and W. Engle, Nucl. Sci. Eng., 62, 92 (1977).
8. V. I. Usanov and V. I. Savitskii, "Methods of calculating radiation-field functionals over inhomogeneous regions of shielding," At. Énerg., 52, No. 5, 344-346 (1982).
9. Te-Chang Chan, Trans. Am. Nucl. Soc., 26, 469 (1977).
10. S. Cramer, Nucl. Sci. Eng., 79, 417 (1981).
11. V. I. Usanov, Preprint FEI-1333, Power Physics Institute, Obninsk (1982).
12. Zh. N. Bel'skaya et al., Preprint FEI-387, Power Physics Institute, Obninsk (1973).
13. V. B. Polevoi, Vopr. At. Nauk. Tekh., Ser. Fiz. Tekh. Yad. Reakt., No. 9(22), 15 (1981).
14. L. P. Abagyan et al., Group Constants for Calculating Reactors and Shielding [in Russian], Énergoizdat, Moscow (1981).

ACOUSTIC NOISE FROM STEAM GENERATORS IN THE BOR-60 REACTOR
 DURING SIMULATION OF LEAKS BY ARGON AND STEAM

V. M. Sokolov, V. V. Golushko,
 V. A. Afanas'ev, Yu. P. Grebenkin,
 and A. B. Muralev

UDC 621.039.564.22:534.83

Studies of accident conditions in the presence of small and large leaks of water into sodium were carried out on the micromodular 30-MW sodium-water steam generator, developed in the Czechoslovak SSR and tested on the BOR-60 reactor [1]. We tested established systems for discovering leaks and promising new systems, including those based on an analysis of acoustic noise generated by the leak. We also studied acoustic noise on a 20-MW enclosed steam generator.

To study noise in the micromodular steam generator, several acoustic sensors were mounted on one of eight sections (Fig. 1). Submersible transducers, constructed in the GDR, were fabricated from lithium niobate crystals 6 mm in diameter. They were separated from the sodium by a stainless steel membrane 0.1 mm thick. The waveguide acoustic transducers were fabricated in the form of stainless steel rods 10 mm in diameter and 500 mm long. The rods were

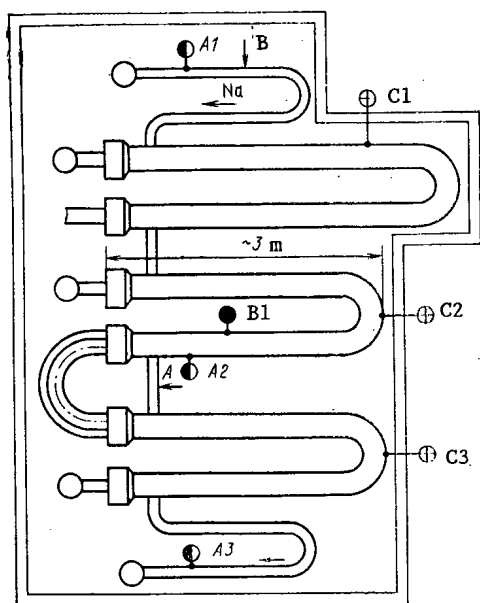


Fig. 1

Fig. 1. Arrangement of the transducers in the micromodular steam generator: A1, A2, A3) submersible transducers; C1, C2, and C3) wave-guide transducers; B1) high-temperature accelerometer; A and B) units for injection of argon (steam).

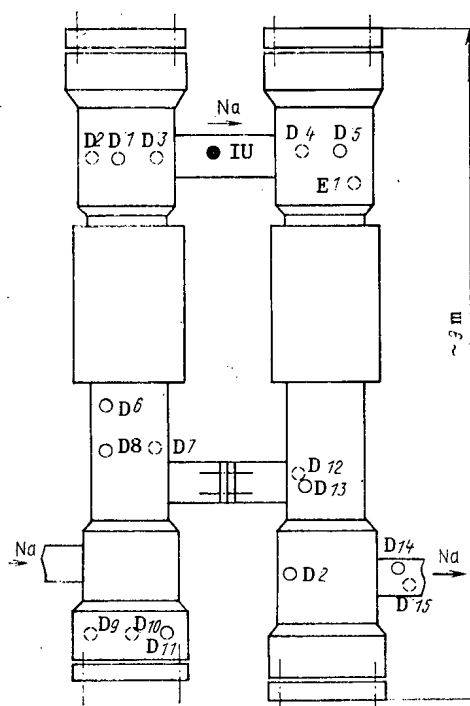


Fig. 2

Fig. 2. Arrangement of the transducers on the enclosed steam generator: D1-D15) waveguide transducers; E1, E2) submersible transducers; IU) argon injection unit.

Translated from Atomnaya Énergiya, Vol. 59, No. 5, pp. 327-330, November, 1985. Original article submitted November 19, 1984; revision submitted March 25, 1985.

welded at one end to the housing of the steam generator. Rings made of TsTS-19 piezoceramic were placed on the cold ends of the rods. In addition, three waveguide sensors were placed on parallel sections of the steam generator, but we did not analyze their signals because of their insensitivity to noise generated by small leaks. The signals from the sensors were recorded on a seven-channel magnetograph in the frequency band 0.2-150 kHz. In some cases, we analyzed the signals in real time with the help of a system for digital processing of stochastic processes [2] using algorithms for calculating the variance and the power spectral density of the signals.

To imitate water leaks into the sodium in a steam generator, we inserted two injection units A and B between the evaporator modules and in front of the superheater module (see Fig. 1).

Fifteen waveguide and two submersible acoustic sensors were mounted on the enclosed steam generator (Fig. 2). The submersible sensors are analogous to those described previously, but the waveguide sensors were fabricated from tubes 6 mm in diameter and 250 mm long. To imitate the leak, an injection unit was mounted on the overflow pipe of the steam generator.

To check the working capacity of the injection units and the adjustment of the detection systems we injected argon into the steam generator. At the same time, we pursued another goal: to obtain data for possible replacement of steam by argon in the investigations and to check the established leak-detection systems.

Spectral analysis of the background noise of the steam generator and the noise generated by argon and steam leaks (Fig. 3) enables drawing a conclusion regarding the possibility of such a replacement; however, the data obtained are characteristic only for this type of steam

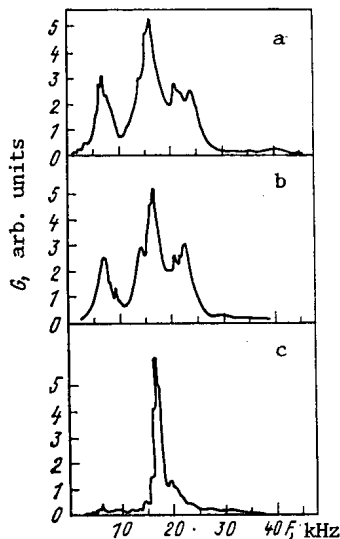


Fig. 3

Fig. 3. Power spectral density of the noise of a micromodular steam generator (A2 sensor): a) with steam flow through the nozzle A at a rate of 0.04 g/sec; b) with argon flow at a rate of 0.032 g/sec; c) background noise.

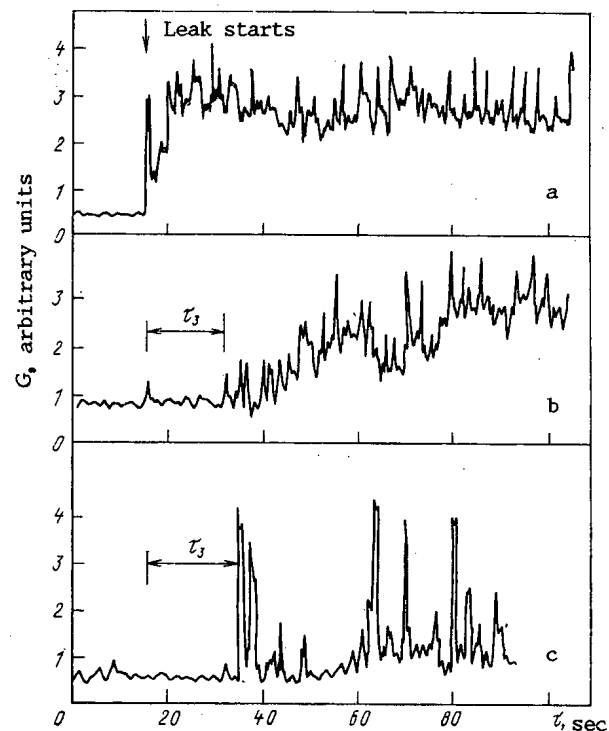


Fig. 4

Fig. 4. Change in the variance of the acoustic noise of a micromodular steam generator accompanying injection of steam (with a flow rate of 0.08 g/sec) through the nozzle B: a) A1 sensor; b) C3 sensor; c) A3 sensor.

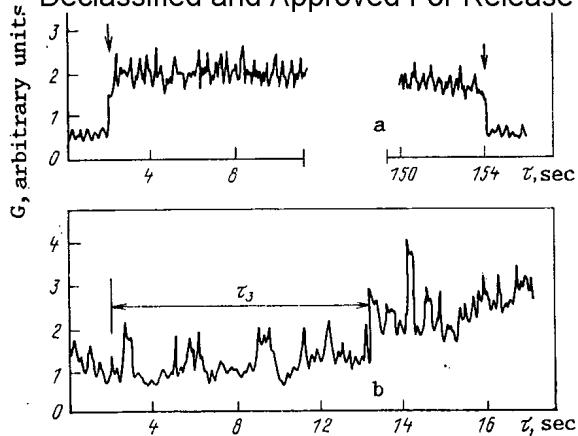


Fig. 5

Fig. 5. Change in the variance of the acoustic noise of an enclosed steam generator accompanying injection of argon (the flow rate is equal to 0.11 g/sec): a) sensor D2; b) sensor D14.

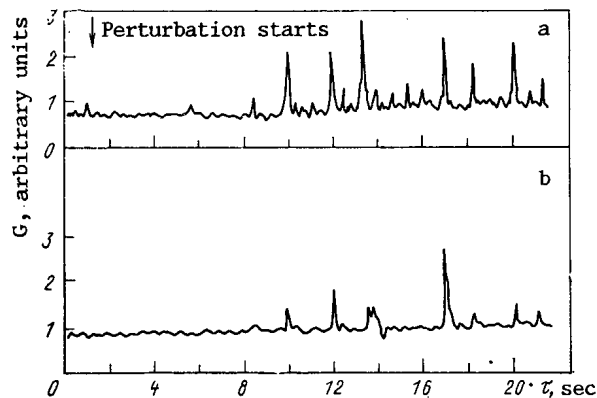


Fig. 6

Fig. 6. Change in the variance of the acoustic noise of an enclosed steam generator accompanying a 10% drop in the sodium flow rate: a) sensor D5; b) sensor D1.

generator with injection in its low-temperature part. When the temperature of the superheater is raised, the relative fraction of the hydrogen reacting with the sodium increases significantly, and the intensity of the acoustic noise becomes significantly lower than for argon. The possibility of replacing steam by argon in a different type of steam generator can be confirmed only experimentally because of the complexity of the mathematical description of the efflux of a jet and its interaction with the elements of the structure of the steam generator. A leak in the presence of obstacles creates a louder noise than the same leak (or even a larger leak) in the absence of obstacles.

The spectral composition of the recorded signals is determined not only by the noise generated by the leak, but also by resonance properties of the object on which the sensor is placed, the properties of the sensor itself, and its connection joint. When studying the spectra of signals from the submersible sensors with known characteristics, none of the enumerated factors can be excluded in practice, because in order to obtain an airtight seal at high sodium temperatures the bond between the sensor and the steam-generator vessel must be rigid. In reality, the steam-generator — connecting joint — sensor system is an electro-mechanical filter with variable characteristics depending on the conditions under which the experiments are performed. The reaction of the system to the background noise of the steam generator (see Fig. 3) is determined, in addition, by the presence of a high-frequency filter, which lowers the signal amplitude at frequencies ≤ 5 kHz. It is inserted into the recording system because of the high background noise level of the steam generator at low frequencies in order to separate out the information on the leak at higher frequencies, since the recording apparatus has a limited dynamic range.

Figure 3 shows that the noise band generated by the leak is wider than the background noise band generated by the steam generator; in addition, both high and low frequencies appear in the spectrum. It is possible that the drop in the power spectral density of the noise at 17 kHz is caused by a change in the resonance properties of the steam generator or screening of part of the acoustic energy by a cloud of argon or hydrogen bubbles. An analogous situation is also characteristic for other sensors.

Figure 4 shows the dependence of the change in the variance of the signals as a function of time for sensors placed at different heights in the steam generator with steam injected through the upper nozzle B. The sensor A1, positioned above the location of the leak along the sodium path, reacts practically instantaneously to the appearance of the leak; the delay in the signals from the leak at the bottom sensors corresponds to the propagation time of hydrogen bubbles with the sodium flow into the region where the sensors are located. The sensor A1 receives more noise from the steam jet and less noise from the motion of the hydrogen bubbles. The sensor B1, on the other hand, receives more noise generated by the motion of the hydrogen bubbles. Moreover, the cloud of bubbles in a quite developed flow can screen the noise from the steam jet. The lower sensors C3 and A3 react only to the appearance of

To confirm what was said above we can add the fact that the injection of argon (steam) with a flow rate of ≤ 0.9 g/sec in the bottom nozzle A can be recorded above the location of the leak only by the nearest sensors A2, B1, and C2 and by the transducers C3 and A3 positioned below the leak.

Analogous results were obtained in a study of the noise generated by an argon leak in an enclosed steam generator. The noise from the leak with a relatively low flow rate (< 0.15 g/sec) is recorded only by the sensors D1-D5 and E1, positioned approximately at the same level as the injection unit (Fig. 5). The sensors D6-D11, positioned above the leak along the sodium path, do not react to the leak because of the high attenuation of the sound energy during its propagation along the steam generator. It should be noted that the sensor D6 is situated approximately at the same distance (~ 3 m) from the location of the leak as the sensor C2 in the micromodular steam generator, which reacted reliably to all leaks implemented through the nozzle A. For comparison, we point out that the line in the micromodular steam generator has a diameter of 160 mm while the diameter of the vessel is equal to ~ 1 m. The signal from the leak can be distinguished on the sensors D14 and D15, situated 8 m from the location of the injection, with a delay of about 12.5 sec relative to the onset of the leak and only at high frequencies 40-60 kHz. The sodium velocity in the steam generator is not high enough to entrain downwards large argon bubbles, so that only very small bubbles, which have a high resonance frequency, contribute to the signal spectrum.

A comparison of the results obtained with the help of different sensors leads to the same conclusions regarding the nature of the background noise and the leak signals (spectral density, signal-to-noise ratio, etc.) in the case when the transmission band of the transducers is the same.

The investigations showed that the efficiency with which the leaks are detected depends on the background noise level of the steam generator. We studied the background noise in an enclosed steam generator for different power levels and by perturbing its operation by changing the parameters by several percent. The intensity of the noise generated by the steam generator is determined primarily by the boiling of the water and the motion of the steam-water mixture and of steam. Disturbances which can accompany operational changes in the operating conditions of the system or actuation of systems for regulating the parameters of the steam generator both increase and decrease the background acoustic noise level. For example, when the sodium flow rate is changed rapidly (Fig. 6) the background noise level increases after some time interval; in addition, as a rule, impulsive components appear in the signal, independently of the construction of the sensor used. The time interval within which the noise reaches a new stationary level is determined by the type of perturbation and can constitute several tens of minutes. Analogous results were also obtained for the micromodular steam generator.

In spite of the fact that we studied the noise from steam generators with different constructions, we can point out several common features. In both types of steam generators, changes in the operating conditions produce changes in the background noise level which can be comparable to the reaction of the sensors to small leaks. The quite strong attenuation of the sound energy as it propagates along the steam generator, which makes it more difficult to separate the signals generated by a leak at distant sensors, should be noted.

LITERATURE CITED

1. V. A. Tsykanov, G. K. Antipin, V. V. Borisov, et al., "Study of the interaction of sodium with water in the BOR-60 micromodular steam generator," *At. Énerg.*, 51, No. 1, 3-6 (1981).
2. V. V. Golushko, V. S. Dunaev, and A. B. Muralev, "System for digital processing of stochastic processes (software)," Preprint NIIAR, P-18 (352), Dimitrovgrad (1978).

ANISOTROPIC TURBULENT HEAT TRANSFER IN CHANNELS OF NUCLEAR POWER
REACTORS

V. P. Bobkov

UDC 621.039.534.25

Great significance is attached to computational methods, based on the use of differential energy equations, for substantiation of the operating temperature conditions of fuel cells in reactors cooled by homogeneous coolants in the presence of turbulent flow in channels with a complicated profile. To close this system of equations it is necessary to know, in particular, the characteristics of the heat transfer. Heat transfer in channels with a complicated profile has the following characteristics: the velocity field and the temperature field are three-dimensional; the temperature field in the flow and in the fuel element is a function of the properties and geometry of the fuel element as well as the properties of the flow (adjoint problem).

In order to take these features into account, it is necessary to know the laws of turbulent transport along the normal to the wall and in the azimuthal (tangential) direction; in longitudinal runs the laws of transfer along the average motion must also be known.

The existence of a significant difference in the intensity of turbulent heat transfer in the flow near the wall in different directions relative to an exothermic wall has now been established. It is well known that the intensity of turbulent heat transfer is characterized by the coefficient of turbulent heat transfer (CTHT) introduced in analogy to Boussinesq's hypothesis.

We shall write the system of energy equations in a somewhat simplified form for the region of the fuel element and for the region of fluid flow, respectively:

$$\alpha_w \frac{\partial^2 T_w}{\partial x_i \partial x_i} = \left(\frac{q_v}{\rho C_p} \right)_w; \quad (1)$$

$$\alpha_f \frac{\partial^2 T_f}{\partial x_i \partial x_i} + \frac{\partial}{\partial x_i} (-\overline{u_i' T'}) = u_i \frac{\partial T_f}{\partial x_i} + \left(\frac{q_v}{\rho C_p} \right)_f, \quad (2)$$

where α_w and α_f are the coefficients of thermal diffusivity for the wall and the liquid, respectively; T , temperature; T' , temperature pulsation; q_v , specific volume liberation of heat; x , coordinate; ρ , density; C_p , heat capacity; u , velocity; u' , pulsation of the velocity; $i = 1, 2$, and 3 ($i = 1$ corresponds to the direction along the average motion; $i = 2$ to the direction along the normal to the wall; and $i = 3$ to the tangential direction).

The condition for interaction between the regions consists of the equality of the temperatures and heat fluxes at the interaction boundary. The system of energy equations becomes closed, if the velocity field u_i and the turbulent heat fluxes $u_i' T'$ are known. We shall express the latter in terms of the CTHT α^T . We shall assume that for three-dimensional problems α^T is a tensor of at least rank two, since

$$\overline{u_i' T'} = \alpha_{ik}^T \frac{\partial T}{\partial x_k}; \quad k = 1, 2, 3. \quad (3)$$

Then the CTHT tensor assumes the form

$$\alpha_{ik}^T = \begin{Bmatrix} a_{11} & a_{12} & a_{13} \\ a_{21} & a_{22} & a_{23} \\ a_{31} & a_{32} & a_{33} \end{Bmatrix}. \quad (4)$$

In practical engineering calculations the secondary off-diagonal terms are neglected in order to simplify the problem. Then Eq. (2) assumes the form

$$\frac{\partial}{\partial x_i} \left[(a + \delta_{ik} \alpha_{kj}^T) \frac{\partial T_f}{\partial x_j} \right] = u_i \frac{\partial T_f}{\partial x_i} + \left(\frac{q_v}{\rho C_p} \right)_f, \quad (5)$$

Translated from *Atomnaya Énergiya*, Vol. 59, No. 5, pp. 330-335, November, 1985. Original article submitted October 30, 1984.

TABLE 1. Variants of the Computational Experiment

Channels (number of variants)	Pr	Re	$\theta = r_1/r_2; S/d$	Coeff. of approximate thermal modeling ϵk_0
Cylindrical tubes (44)	0-100	10^4-10^5	—	—
Ring-shaped channels (256)	0-100	—	0,06-1,0	—
Triangular rod bundles (3000)	0-10	—	1,0-2,0	0,01-1000
Tetragonal rod bundles (1200)	0,02	—	—	0,1-100
	0,7			
	5.0			

Note. r_1 and r_2 are the inner and outer radii of the ring-shaped channel; S is the spacing of the fuel elements in the bundle; d is the tube diameter.

TABLE 2. Error in the Computational Data Relative to the Experimental Data for Nu

Channels	Coolant	Re	Error, %	
			rms	arithmetic mean
Cylindrical tubes	Liquid metals, water, air, ethylene glycol	5000-100000	7	3
Ring-shaped channels	Liquid metals, water, air	—	10	4
Triangular rod bundles, $S/d = 1, S/d > 1.1$	—	—	10-15	3-10
Triangular rod bundles, $1.02 \leq S/d \leq 1.06$	Water	2000-80000	—	40
Triangular rod bundles, $1.0 \leq S/d \leq 1.1$	Liquid metals, gases	5000-100000	10-15	3-10
Assemblies of fuel elements with a shell and a plunger	Liquid metals	2000-75000	~ 10	~ 5-10

where δ_{ijk} is the unit tensor of rank two; $j = 1, 2$, and 3 .

A method for directly measuring α^T for flow in channels with a complicated profile has still not been developed because of the difficulties associated with the complexity of the concept of the coefficient of turbulent transfer. The well-known trace method, used for studies in anisotropic inhomogeneous flow, gives very approximate results. The lack of accurate direct measurements does not permit checking the existing semiempirical models, for example, the model of N. I. Buleev [1].

A new computational-experimental approach to the determination of the CTHT, which can be used for flow in channels with a complicated profile and which reveals the anisotropic nature of the transfer, was proposed and developed in the works of this author and his colleagues [2, 4]. The method is based on the development of the theory of homogeneous diffusion, and it makes use of the experimental values of the statistical characteristics of the velocity and temperature fields [2]. Methods for improving this approach, the substantiation of the approach, and the results obtained by using it are demonstrated in different publications. The purpose of this paper is to summarize all work performed and to present some new results.

The essence of the new approach to determining α^T in channels consists of the following. Under the assumption that the turbulent flow in the channels obeys the hypothesis of local homogeneity, the relation obtained in the theory of homogeneous diffusion for the coefficient of turbulent transfer of flow particles v_T for long diffusion times is used:

$$v_T = \bar{y}^2 / (2T) = \sigma^2 \int_0^\infty R(\tau) d\tau = \sigma^2 T,$$

where y is the distance from the wall; σ , intensity of the velocity pulsations; $R(\tau)$, autocorrelation coefficient; τ , time displacement; and T , macro time scale of the pulsations.

The value of σ is taken from the generalization presented in [3], and the validity of this approach is justified in [4]. It is more difficult to determine the Lagrange macro time scale T , which determines the heat transfer.

First of all, in a turbulent flow with displacement, especially in channels with a complicated profile, the Lagrange macro time scale must exhibit a directional variation just as does the intensity of the velocity pulsations. Characterizing the average lifetime of a disturbance, T must reflect the fact that the instantaneous pulsational motion near the wall may turn out to be and indeed is substantially two-dimensional (in a plane) or one-dimen-

Declassified and Approved For Release 2013/02/20 : CIA-RDP10-02196R000300070005-0
sional (along one axis). The pulsational motion could be the result of rotational or translational motion of the flow in a plane parallel to the wall, when the motion in a direction along the normal to the wall is prevented by its proximity. Thus T_2 (for motion in a direction along the normal to the wall) is much shorter than T_3 and T_1 (for motion in the tangential direction and in a direction along the average motion, respectively). An exact determination of the Lagrange macro time scale in terms of measurable Euler correlations cannot be made at the present time. We therefore introduce [2] the concept of the macro time scale T_i which determines the magnitude of the turbulent transfer in a given direction and replaces the concept of the Lagrange macro scale. Then, for $k = 1$

$$a_{ih}^T = \sigma_i^2 T_i. \quad (6)$$

Second, in order to determine the macro time scale determining the heat transfer, it is not the velocity correlation functions that must be used, but rather the correlation functions obtained from studies of the temperature pulsations. We assume that in this case the molecular diffusion of heat is taken into account automatically. As a result, a model for turbulent Pr need not be constructed. We obtain the value of Pr_T with the help of the method proposed in [4]. The method for determining the macro time scale determining heat transfer is described in [2, 5]. The calculations performed enabled obtaining generalized dependences for T_i [6], which are used in the relations for a_{22}^T and a_{33}^T [7, 8]:

$$\frac{a_{22}^T}{a} = 0.16 \operatorname{Re} \operatorname{Pr} [1 - \exp(-0.62 \cdot 10^{-4} \operatorname{Re} \sqrt[3]{\operatorname{Pr}})] \left(\frac{u}{u_0}\right)^6 \left(\frac{\bar{u}}{u_0}\right)^2 \left(1 - \frac{\bar{u}}{u_0}\right)^2 \exp\left(-1.54 \frac{y}{y_{0\max}}\right); \quad (7)$$

$$\frac{a_{33}^T}{a} = 0.36 \operatorname{Re} \operatorname{Pr} [1 - \exp(-0.62 \cdot 10^{-4} \operatorname{Re} \sqrt[3]{\operatorname{Pr}})] \left(\frac{u}{u_0}\right)^3 \left(\frac{\bar{u}}{u_0}\right)^2 \left(1 - \frac{\bar{u}}{u_0}\right)^2 \exp\left(-2.34 \frac{y}{y_{0\max}}\right), \quad (8)$$

where u_0 is the maximum velocity; \bar{u} is the average velocity; and $y_{0\max}$ is the maximum distance from the wall to the line of the maximum velocity.

In the relation (7), as also in the relation (8), all constants, with the exception of one, were obtained from generalizations of the intensity of the components of the velocity pulsations and the time scales of temperature perturbations; the dependence on the Re and Pr numbers is also determined from these generalizations. We refined only the exponents of u/\bar{u} from the condition that they satisfy the average temperature fields for coolants with large values of Pr , when it is very important to have an accurate field of a^T in the zone near the wall. All constants are universal for typical cells of channels whose transverse cross section has a complicated shape for values of Re varying from 5000 to 100,000 and values of Pr varying from 0 to ~ 10 (100).

These relations for a_{22}^T and a_{33}^T are widely known [9-11]. In recent years they have been checked with the help of a computational experiment, as a result of which the temperature fields and the values of Nu for flows of liquid metals, gases, and water in ring-shaped channels [12], triangular and tetragonal rod bundles [13-16], and other channels with a more complicated transverse cross section (Table 1) were calculated. The error with respect to the experiment is in most cases small (Table 2).

In the past, only the two principle components of the tensor (a_{22}^T and a_{33}^T) were combined by this method and used. Because of the practical value of the third component this author calculated the relation for the component along the average motion a_{11}^T .

In the calculation of the macro time scale for transfer in the transverse direction, along which there is no average motion, we assumed that it is necessary to take into account the displacement of particles precisely in the direction of transport, and we determined the spatial displacement in terms of the intensity of the velocity pulsations ($\delta_i = \sigma_i^T$). For transport in a direction along the average motion, the particle displacement is determined primarily by the value of the average velocity u_1 . Then

$$T_1 = \int_0^\infty R(\tau, \delta), \dots, \quad (9)$$

where δ is the displacement in space, i.e., the lifetime of the temperature perturbation for a displacement along the average motion is determined by the space-time correlation coefficient with an optimal displacement $\delta = u\tau$. In this case,

$$T_1 \sigma_1 \approx T_E u_1. \quad (10)$$

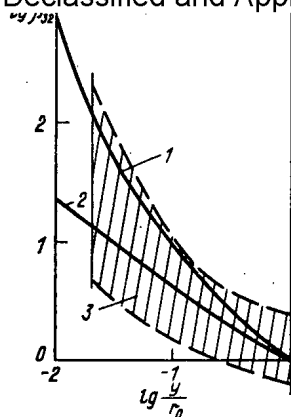


Fig. 1

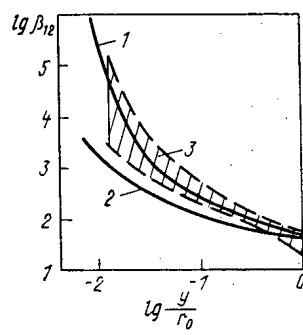


Fig. 2

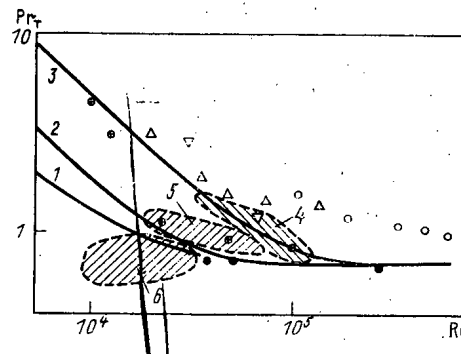


Fig. 3

Fig. 1. Variation of β_{32} over the cross section of the flow in the tube. The calculations based on formula (14): 1) $Re = 10^4$; 2) $Re = 10^5$; 3) experimental data from [18, 19] for $Re = 10^4 - 2 \cdot 10^5$; $Pr(Sc) = 0.7 - 1200$.

Fig. 2. Variation of β_{12} over the cross section of the flow in the tube. Calculations based on the formula (15): 1) $Re = 10^4$; 2) $Re = 10^5$; 3) data from [20], $Re = 10^4 - 2 \cdot 10^5$.

Fig. 3. Pr_T versus Re and Pr . Calculations using the formula (18): 1) $Pr = 3$; 2) $Pr = 0.7$; 3) $Pr = 0.023$; experimental data: 4) [25]; 5) [26]; 6) [27]; ●) [10, 32]; ○) [28]; ⊕) [29]; △) [30]; ▽) [31]; 4, 5, 6, ○, ⊕, △) $Pr \approx 0.02$; ●) $Pr \approx 0.07$.

More accurately, $T_1 \sigma_1 \approx T_E (u_1 + \sigma_1)$, where T_E is Euler's macro time scale.

The relation (10) enables evaluating approximately the macro time scale T_1 , determining the turbulent transport of heat in a direction along the average motion. Using the results of [6, 17] for the description of Euler's macroscopic time scale for temperature pulsations and the results of [3] on the generalization of the intensity of velocity pulsations, we obtain an approximate relation for T_1 in the form

$$T_1 = \frac{1.05 d_0}{u} [1 - \exp(-0.62 \cdot 10^{-4} Re \sqrt[3]{Pr})] \frac{u}{\sigma_1}, \quad (11)$$

where d_0 is the diameter of the fuel element in the bundle.

Using (6) and (11), we obtain

$$a_{11}^T = \sigma_1^2 T_1 \approx 1.05 \cdot 0.95 \frac{d_0}{u} \times \\ \times u [1 - \exp(-0.62 \cdot 10^{-4} Re \sqrt[3]{Pr})] \left(1 - \frac{\bar{u}}{u_0}\right) \exp\left(-1.48 \frac{y}{y_{0\max}}\right). \quad (12)$$

After some transformations, we obtain

$$\frac{a_{11}^T}{a} \approx 6.7 Re Pr [1 - \exp(-0.62 \cdot 10^{-4} Re \sqrt[3]{Pr})] \left(1 - \frac{\bar{u}}{u_0}\right)^2 \left(\frac{u}{u_0}\right)^2 \left(\frac{u_0}{u}\right)^2 \exp\left(-1.48 \frac{y}{y_{0\max}}\right). \quad (13)$$

From (7), (8), and (13) we obtain a relation for the anisotropy coefficients, i.e., for ratios of the GHTT in different directions to the value of the transfer in a direction along the normal to the wall:

$$\beta_{32} = \frac{a_{33}^T}{a_{22}^T} \approx 2.25 \left(\frac{u_0}{u}\right)^3 \exp\left(-0.8 \frac{y}{y_{0\max}}\right); \quad (14)$$

$$\beta_{12} = \frac{a_{11}^T}{a_{33}^T} \approx 42 \left(\frac{u_0}{u}\right)^2 \left(\frac{u_0}{u}\right)^4. \quad (15)$$

We shall compare these results with the experimental data for flow in circular tubes. Within the limits of error of the experiment, the values of β_{32} from the formula (14) are in agreement with the data from [18, 19], obtained by the approximate trace method, which gives a spread of an order of magnitude in the data (Fig. 1), i.e., our method actually predicts

Declassified and Approved For Release 2013/02/20 : CIA-RDP10-02196R000300070005-0
the previously obtained experimental results. The calculation using the values of $\beta_{1,2}$ close to the correct data of [20], obtained by rescaling the results from [20-23] (Fig. 2).

Let us analyze the different theoretical approaches to the interpretation of the anisotropy of turbulent transfer. N. I. Buleev asserts in his works, for example [23], that the degree of anisotropy of the coefficients of turbulent transfer is determined only by the degree of anisotropy of the intensity of velocity pulsations:

$$\beta_{32} = \frac{\sigma_3^2}{\sigma_2^2}; \quad \beta_{12} = \frac{\sigma_1^2}{\sigma_2^2}. \quad (16)$$

It is assumed that the macro time scales determining turbulent transfer are the same in all directions. It was shown above that this is not always the case, but is valid only when the real picture of the motion of separate vortices is ignored.

N. M. Galin proposes in [20] that the anisotropy of transfer is determined by the anisotropy of the squares of the spatial hydrodynamic scales:

$$\beta_{32} = \left(\frac{L_3}{L_2}\right)^2; \quad \beta_{12} = \left(\frac{L_1}{L_2}\right)^2. \quad (17)$$

This interaction gives more correct results. However, it requires the construction of some model for describing Pr_T .

It follows from calculations using the formulas (14) and (15) that the degree of anisotropy decreases at the same distance from the wall as Re increases. This is consistent with the well-known fact that for very high Re the turbulence is close to being isotropic and homogeneous.

The approach generalized in this paper enabled objective estimation of the behavior of Pr_T for flows of different coolants in pipes as a function of Re and over the cross section of the flow [4] (Fig. 3):

$$Pr_T = \frac{v_T}{a^T} = \frac{\sigma_T^2 T_v}{\sigma_v^2 T_r} = 0.69 \left(\frac{u_0}{u}\right)^{0.5} [1 - \exp(-0.62 \cdot 10^{-4} Re^3 \sqrt{Pr})]^{-1}. \quad (18)$$

For small values of Re and Pr , the values of Pr_T can be much greater than one. As Re and Pr increase, the values of Pr_T decrease and approach a constant value close to 0.7. The latest quite numerous and reliable data confirm this behavior, obtained back in 1970.

We note that the foregoing approach to the determination of a^T shows that the coefficient of heat transfer can be changed by changing the properties of the exothermic surface, because the pulsations of the temperature in the coolant flow and in the wall depend on the properties of the flow and on the properties of the wall (adjoint problem). Because of this mutual effect, a change should be expected in the spectrum of the temperature pulsations in the flow and therefore of the integral macro time scale, determining the heat transfer in the flow accompanying a change, for example, in the thermal conductivity of the wall.

When anisotropic CHT are used in calculations of the temperature conditions in fuel elements, located in complicated flow conditions, it is important to determine the orientation of the principal components of the tensor a^T , i.e., the orientations of the principal axes of anisotropy, along which a^T assumes extremal values. There are no theoretical suggestions regarding this in the literature. From statistical studies of pulsations of the velocity and temperature, however, the following can be asserted quite reliably. The maximum values of a^T are observed along the direction of the average flow velocity (this is one of the principal axes); the minimum value of a^T is observed in the direction of the maximum gradient of the average velocity; the third axis is the direction along the isotachs. These directions are mutually perpendicular. When the coordinate axes are rotated relative to the orientation of the principal axes of anisotropy, the use of a three-dimensional elliptical law for the variation of a^T as a function of the angle of rotation gives good results in the calculations.

Other questions regarding the use of a^T in calculations of three-dimensional temperature fields are presented in detail in the references.

LITERATURE CITED

1. N. I. Buleev and G. A. Zinina, "Correction of starting hypotheses in a three-dimensional model of turbulent diffusion," *Vopr. At. Nauki Tekh., Ser. Fiz. Tekh. Yad. Reaktorov*, No. 2(24), 26-35 (1982).
2. V. P. Bobkov, M. Kh. Ibragimov, and V. I. Subbotin, "Calculation of the coefficients of turbulent transport of heat during fluid flow in a pipe," *At. Énerg.*, 24, No. 5, 442-447 (1968).
3. V. P. Bobkov, M. Kh. Ibragimov, and G. I. Sabelev, "Generalization of experimental data on the intensity of velocity pulsations in the turbulent fluid flow in channels with different shape," *Teplofiz. Vys. Temp.*, 6, No. 4, 162-165 (1968).
4. V. P. Bobkov and M. Kh. Ibragimov, "Application of the model of homogeneous diffusion to the calculation of tangential stresses and the velocity field in a turbulent fluid flow in a pipe," *Teplofiz. Vys. Temp.*, 8, No. 2, 326-329 (1970).
5. V. P. Bobkov, M. Kh. Ibragimov, and G. I. Sabelev, "Method for calculating the coefficient of turbulent diffusion of heat in channels with an irregular transverse cross section," *Teplofiz. Vys. Temp.*, 6, No. 4, 674-681 (1968).
6. V. P. Bobkov, M. Kh. Ibragimov, and G. I. Sabelev, "Calculation of the coefficients of turbulent heat transport in fluid flow in channels," Preprint FEI-113, Obninsk (1968).
7. V. P. Bobkov, M. Kh. Ibragimov, and V. I. Subbotin, "Method for calculating the coefficients of turbulent transport of heat in channels with a complicated shape," in: *Modeling of Thermodynamic Phenomena in the Active Zone of Fast Reactors*, Czechoslovakian Atomic Energy Commission, Sbraslav (1971), pp. 8-17.
8. M. Kh. Ibragimov, V. I. Subbotin, and V. P. Bobkov, "Calculation of temperature fields in channels with noncircular transverse cross section," *ibid.*, pp. 104-111.
9. V. I. Subbotin, M. Kh. Ibragimov, P. A. Ushakov, et al., *Hydrodynamics and Heat Transfer in Nuclear Power Plants* [in Russian], Atomizdat, Moscow (1975).
10. M. Kh. Ibragimov, V. I. Subbotin, V. P. Bobkov, et al., *Structure of the Turbulent Flow and the Mechanism of Heat Transfer in Channels* [in Russian], Atomizdat, Moscow (1978).
11. B. S. Petukhov, L. G. Genin, and S. A. Kovalev, *Heat Transfer in Nuclear Power Plants* [in Russian], Atomizdat, Moscow (1974).
12. V. P. Bobkov, M. Kh. Ibragimov, and N. K. Savanin, "Heat transfer in turbulent flow of different heat-transfer agents in ring-shaped gaps," *Teplofiz. Vys. Temp.*, 13, No. 4, 779-786 (1975).
13. V. P. Bobkov, M. Kh. Ibragimov, and V. I. Subbotin, "Generalizing dependences for heat transfer in the fuel assemblies of liquid-metal cooled nuclear reactors," *Teplofiz. Vys. Temp.*, 10, No. 4, 795-803 (1972).
14. V. P. Bobkov and N. K. Savanin, "Calculation of heat transfer in turbulent water flow in the channels of an infinite tetragonal array of cylindrical fuel elements," Preprint FEI-602, Obninsk (1975).
15. V. P. Bobkov and N. K. Savanin, "Calculation of heat transfer in turbulent gas flow in the channels of an infinite tetragonal array of cylindrical fuel elements," Preprint FEI-633, Obninsk (1975).
16. V. P. Bobkov and N. K. Savanin, "Calculation of heat transfer in turbulent flow of liquid metals in the channels of an infinite tetragonal array of cylindrical fuel elements," Preprint FEI-644, Obninsk (1975).
17. V. P. Bobkov, M. Kh. Ibragimov, V. I. Subbotin, et al., "Time-dependent characteristics and the spectrum of temperature pulsations in turbulent fluid flow in a pipe," *Teplofiz. Vys. Temp.*, 6, No. 1, 97-102 (1968).
18. A. Quarmby, "Axisymmetric and nonaxisymmetric turbulent diffusion in a circular tube at high Schmidt number," *Int. J. Heat Mass Transfer*, 17, No. 1, 143-147 (1974).
19. A. Quarmby and R. Quirk, "Measurement of the radial and tangential eddy diffusivities of heat and mass in turbulent flow in a plain tube," *ibid.*, 15, 2309 (1972).
20. N. M. Galin, "Coefficients of diffusion in anisotropic turbulence," *Izv. Akad. Nauk SSSR, Énerg. Transport*, No. 6, 130-139 (1980).
21. M. Kh. Ibragimov, V. I. Subbotin, and G. S. Taranov, "Velocity and temperature pulsations and their correlations in a turbulent air flow in a pipe," *Inzh.-Fiz. Zh.*, 19, No. 6, 1060 (1970).
22. K. Bremhorst and K. Bullock, "Spectral measurements of temperature and longitudinal velocity fluctuations in full developed pipe flow," *Int. J. Heat Mass Transfer*, 13, No. 8, 1313-1329 (1970).

23. M. Liem, "Etude expérimentale de la turbulence au voisinage de la paroi d'un tube legerement chauffe," Int. J. Heat Mass Transfer, 20, No. 9, 935-944 (1977).
24. N. I. Buleev and L. S. Sukhomlin, "Hydrodynamics and heat transfer in turbulent fluid flows in ring-shaped concentric gaps," Vopr. At. Nauki Tekh. Ser. Fiz. Tekh. Yad. Reaktorov, No. 2(24), 3-16 (1982).
25. Sh. E. Isakov and T. B. Dryu, "Heat exchange and momentum in turbulent flow of mercury," in: Problems in Heat Transfer [in Russian], Gosenergoizdat, Moscow (1959), pp. 107-113.
26. V. I. Subbotin, M. Kh. Ibragimov, and M. I. Ivanovskii, "Turbulent heat transfer in liquid-metal flow," At. Énerg., 10, No. 4, 334-386 (1961).
27. L. G. Genin, T. E. Krasnoshchekova, S. P. Manchka, et al., "Problem of the structure of the temperature field in turbulent flow in pipes," Teplofiz. Vys. Temp., 17, No. 3, 531-538 (1979).
28. H. Brown, B. Amstead, and B. Short, "Temperature and velocity distribution and transfer of heat in a liquid metal," Trans. ASME, 79, No. 2, 279-285 (1957).
29. T. Mizushima and T. Sasano, "The ratio of the eddy diffusivities for heat and momentum and its effect on liquid metal heat transfer coefficients," in: Int. Development in Heat Transfer, Colorado (1961), pp. 662-668.
30. C. Sleicher, A. Awad, and R. Notter, "Temperature and eddy diffusivity profiles in Na-K," Int. J. Heat Mass Transfer, 16, No. 8, 1565-1575 (1973).
31. R. Lyon, "Liquid metal heat-transfer coefficients," Chem. Eng. Progress, 47, No. 2, 75-79 (1951).
32. R. Gowen and J. Smith, "Turbulent heat transfer from smooth and rough surface," Int. J. Heat Mass Transfer, 11, No. 11, 1657 (1968).

PROMPT NEUTRONS FROM THE LOW-ENERGY FISSION OF ATOMIC NUCLEI

B. F. Gerasimenko and V. A. Rubchenya

UDC 539.173.84

The characteristics of prompt fission neutrons (PFN) — spectra, average number of neutrons — are important for nuclear reactor calculations. It is necessary to know the characteristics of PFN of various nuclides and the excitation energies, which are very difficult to measure. The available experimental data [1] are rather limited and inadequate for practical requirements. In view of this, it is important to develop theoretical methods for calculating PFN characteristics in order to supply the missing data or to increase the reliability of the estimates and extrapolations. On the other hand, the study of PFN makes it possible to investigate the fission of atomic nuclei and the mechanism of the deexcitation of highly excited states of fragment nuclei with a neutron excess.

Studies show that the PFN are emitted by the fragment nuclei, and that the probability of the formation of neutrons in the separation process is very small and apparently close to the probability of the emission of light charged particles in ternary fission. Most of the PFN are emitted by strongly heated fragments in accordance with the laws of equilibrium statistics. The so-called isotropic fraction of the PFN in the laboratory coordinate system observed in [2] may be due to a nonequilibrium mechanism of particle emission. The ratio of the contributions of equilibrium and nonequilibrium mechanisms is determined by the rate of transformation of the deformation energy of fragments, in which the main part of their excitation energy is concentrated, for low-energy fission, into thermal energy. On the basis of the model of the nonequilibrium mechanism of emission of PFN [3] as a result of a nonadiabatic change of shape of fragments directly after separation, it can be concluded that the contribution of such neutrons is $\leq 10\%$ under reasonable assumption of the distribution of the fragment deformations and the coefficient of viscosity. The characteristic time of emission of neutrons determined by the nonequilibrium mechanism is shorter than the time of acceleration of the fragment nuclei, and therefore the angular distribution of these neutrons is not distorted by the velocity of the fragments. Separating out the nonequilibrium mechanisms of the emission of PFN requires detailed calculations of the equilibrium component in order to draw reliable conclusions about the properties of the nonequilibrium component from a comparison with experimental data. In addition to taking account of possible mechanisms of the deexcitation of fragment nuclei, a theoretical analysis must correctly account for the distributions of excitation energy, kinetic energy, charge, and mass. These calculations are made difficult by the inadequate knowledge of the properties of the fragment nuclei.

Many theoretical calculations of the characteristics of PFN have been performed in the statistical approximation, but these calculations did not take account of special features associated with the characteristics of the fission fragments. Analysis [4] showed that agreement of the calculated and experimental values requires a refinement of the description of the level densities of fragment nuclei and the cross section for the process inverse to the radiation of a neutron. A simple version of the evaporation model was used in [5] in which averaging over the distribution of fragment parameters was replaced by averaging over the triangular distribution of the temperature for two fragments belonging to the light and heavy groups. Consistent calculations within the framework of the cascade-evaporation model were performed in [6]. The soundest approach is the use of the Hauser-Feshbach statistical theory to calculate the characteristics of PFN [7]. We also use this method in the present article, but with the following differences from [7]: a more accurate account of the cascade nature of neutron emission, a different method of determining the average excitation energy of the fragments, an expression for the level density which takes account of the shell structure of nuclei [8]. We present the results of a calculation of the spectra and multiplicity distribution of PFN for the most important cases, namely the spontaneous fission of ^{252}Cf and the thermal-neutron fission of ^{235}U .

Translated from *Atomnaya Énergiya*, Vol. 59, No. 5, pp. 335-339, November, 1985. Original article submitted October 16, 1984; revision submitted March 21, 1985.

The integral spectrum of PFN of the compound nucleus of mass number A_c , charge Z_c , and excitation energy E_c^* is formed from the individual fragments:

$$N(E, A_c, Z_c, E_c^*) = \sum_{A, Z} Y(A, Z, A_c, Z_c, E_c^*) N(E, A, Z), \quad (1)$$

where the $Y(A, Z, A_c, Z_c, E_c^*)$ are the independent yields of fragments with mass number A and charge Z , normalized to unity. The energy spectrum of the PFN of individual fragments $N(E, A, Z)$ consists of two components:

$$N(E, A, Z) = \bar{v}_s N_s(E, A, Z) + \bar{v}_d N_d(E, A, Z), \quad (2)$$

where $N_s(E, A, Z)$ is the spectrum of PFN emitted statistically from completely accelerated fragments, N_d is the spectrum of PFN emitted either from incompletely accelerated fragments statistically, or as a result of nonequilibrium mechanisms; \bar{v}_s and \bar{v}_d are the average numbers of equilibrium and nonequilibrium PFN from individual fragments, and $\bar{v}(A, Z) = \bar{v}_s + \bar{v}_d$. When the nonequilibrium component N_d was first discovered it was estimated that it contributed up to 20% to the integral spectrum [2]. However, the value of \bar{v}_d has still not been determined; the latest measurements [9] showed that \bar{v}_d/\bar{v} is smaller than estimated in [2]. In the present article we do not consider the nonequilibrium component N_d , and assume that the equilibrium component of the PFN is emitted isotropically from completely accelerated fragments. In this case the spectrum in the laboratory coordinate system is simply related to the spectrum in the center of mass system for a given kinetic energy E_k of a fragment:

$$N_s(E, A, Z, E_k) = \frac{1}{\bar{v}_s} \int_{(\sqrt{E} - \sqrt{E_f})^2}^{(\sqrt{E} + \sqrt{E_f})^2} \frac{\Phi_s(\epsilon, A, Z, E_k)}{4\sqrt{\epsilon E_f}} d\epsilon, \quad (3)$$

where $E_f = E_k A$; $\Phi_s(\epsilon, A, Z, E_k)$ is the PFN spectrum in the center of mass system for a given E_k , normalized to \bar{v}_s . In calculating the integral spectrum it is necessary to average over the E_k distribution:

$$N_s(E, A, Z) = \int_{E_k^{\min}}^{E_k^{\max}} P(A, Z, E_k) N_s(E, A, Z, E_k) dE_k. \quad (4)$$

During the emission of neutrons the initial E_k distribution is distorted as a result of recoil, but this can be neglected in the approximation we are considering.

The spectrum in the center of mass system is formed as a result of the cascade emission of neutrons from excited states of fragments with an initial Gaussian distribution of the excitation energy $P_0(E^*, A, Z, E_k)$:

$$P_0(E^*, A, Z, E_k) = \frac{1}{\sqrt{2\pi\sigma_{E^*}^2}} \exp\left[-\frac{(E^* - \bar{E}^*)^2}{2\sigma_{E^*}^2(A, Z, E_k)}\right]. \quad (5)$$

Here \bar{E}^* is the average excitation energy of a fragment for a given value of E_k , and σ_{E^*} is the variance of the E^* distribution. The averaging over the distribution (5) must be limited by the maximum value E_{\max}^* :

$$E_{\max}^* = \bar{E}^*(A, Z, E_k) + 3\sigma_{E^*}(A, Z, E_k). \quad (6)$$

E_{\max}^* determines the maximum possible number v_{\max} of neutrons emitted by a given fragment in accordance with the inequality

$$E_{\max}^*(A, Z, E_k) - \sum_{i=1}^{v_{\max}} B_n(A-i+1, Z) \leq B_n(A-v_{\max}, Z), \quad (7)$$

where $B_n(A, Z)$ is the binding energy of a neutron. In using Eq. (6) the probability of emission of the v_{\max} -th neutron is < 0.01 . If the distribution of neutron multiplicity $W(v)$ is normalized to unity, the PFN spectrum in the center of mass system is given by the expression

$$\Phi(\epsilon, A, Z, E_k) = \sum_{v=1}^{v_{\max}} \left[1 - \sum_{i=0}^{v-1} W(i)\right] n_v(\epsilon), \quad (8)$$

where $n_v(\epsilon)$ is the energy spectrum of the v -th neutron, normalized to unity.

$$n_1(\varepsilon) = \int_{B_n + \varepsilon}^{E_{\max}^*} P_0(E^*, A, Z, E_k) \varphi(\varepsilon, E^*, A, Z) dE^*, \quad (9)$$

where $\varphi(\varepsilon, E^*, A, Z)$ is the probability of the emission of a neutron of kinetic energy ε from a state with excitation energy E^* . After the emission of the first neutron the new excitation energy distribution can be found from the relation

$$P_1(E^*, A-1, Z, E_k) = \int_{B_n + E^*}^{E_{\max}^*} P_0(E_1^*, A, Z) \varphi(E_1^* - E^* - B_n, E_1^*, A, Z) dE_1^*. \quad (10)$$

In a similar way the spectrum of the v -th neutron is given by the expression

$$n_v(\varepsilon) = \int_{B_n(A-v+1, Z) + \varepsilon}^{E_{\max}^* - \sum_{i=1}^{v-1} B_n(A-i, Z)} P_{v-1}(E^*, A-v+1, Z) \varphi(\varepsilon, E^*, A-v+1, Z) dE^*; \quad (11)$$

$$P_{v-1}(E^*, A-v+1, Z) = \int_{E^* + B_n(A-v+2, Z)}^{E_{\max}^* - \sum_{i=1}^{v-1} B_n(A-i, Z)} P_{v-2}(E_1^*, A-v+2, Z) \varphi[E_1^* - E^* - B_n(A-v+2, Z), E_1^*, A-v+2, Z] dE_1^*. \quad (12)$$

The multiplicity distribution of the PFN for $\Gamma_\gamma/\Gamma_n \ll 1$ is given by the relations

$$W(0) = \int_0^{B_n(A, Z)} P_0(E^*, A, Z) dE^*; \quad (13)$$

$$W(1) = [1 - W(0)] \int_0^{B_n(A-1, Z)} P_1(E^*, A-1, Z) dE^*; \quad (14)$$

$$W(v) = \left[1 - \sum_{i=0}^{v-1} W(i) \right] \int_0^{B_n(A-v, Z)} P_v(E^*, A-v, Z) dE^* \quad (15)$$

The probability of the emission of a neutron, taking account of the distribution of states of the compound nucleus with spin I , can be written in the form

$$\varphi(\varepsilon, E^*, A, Z) = \sum_I \omega(I, E^*, A, Z) \frac{\Gamma_n(\varepsilon, A, Z, E^*, I)}{\Gamma_n^t(A, Z, E^*, I) + \Gamma_\gamma^t(A, Z, E^*, I)}, \quad (16)$$

where Γ_n^t and Γ_γ^t are the total neutron and radiation widths, and $\omega(I, E^*, A, Z)$ is the spin distribution function. The partial neutron width is given by the expression

$$\Gamma_n(\varepsilon, A, Z, E^*, I) = \sum_{I'} \rho[E^* - B_n(A, Z) - \varepsilon, A-1, Z, I'] \sum_{l,j} T_{lj}(\varepsilon), \quad (17)$$

where ρ is the level density of the compound nucleus, and the $T_{lj}(\varepsilon)$ are the sticking coefficients of neutrons. The total radiation width is calculated with the formula

$$\Gamma_\gamma^t(A, Z, E^*, I) = \int_0^{E^*} dU \sum_{I'} T_\gamma(E^* - U, I') \rho(U, A, Z, I'), \quad (18)$$

where T_γ is the sticking coefficient of gamma quanta. The total neutron width is obtained by integrating the partial width (17) over the excitation energy of the daughter nucleus.

The level density ρ was calculated with the formula in [8] which takes account of the effect of nucleon shells and pair correlations. The spin distribution in Eq. (16) was taken the same as that for the level density [8]. The coefficients T_{lj} were calculated with the optical model, using the potential parameters from [10], and the T_γ were calculated by assuming dipole gamma radiation [11].

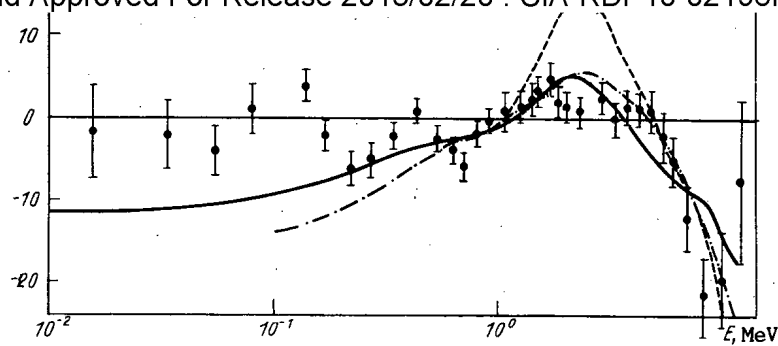


Fig. 1. PFN spectra for the spontaneous fission of ^{252}Cf relative to the Maxwellian spectrum with $T = 1.42$ MeV: —) our calculation; ---) calculated in [6]; -.-) calculated in [15]; ●) experiment [16], $D = [N(E, A_c, Z_c, E_c^*), N(E)]$, $N(E)$ is the Maxwellian spectrum with temperature T .

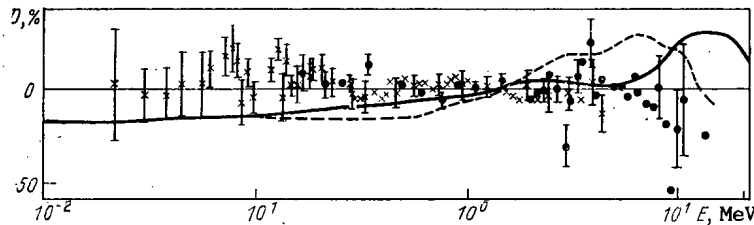


Fig. 2. Calculated integral and experimental PFN spectra for the thermal-neutron fission of ^{235}U relative to the Maxwellian spectrum with $T = 1.31$ MeV: ×, ●) experiment [18], [19]; —) our calculation; ---) calculated in [5].

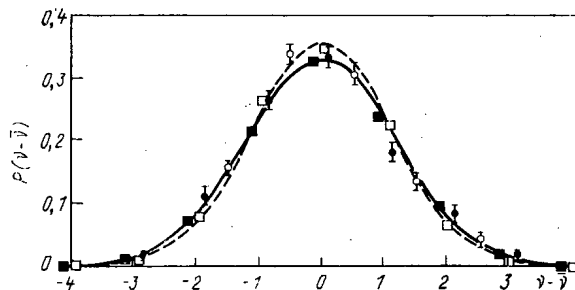


Fig. 3. Multiplicity distribution of PFN for the spontaneous fission of ^{252}Cf (■, calculated, ●, experiment [22]); —) Gaussian distribution with calculated σ_v and the thermal-neutron fission of ^{235}U (□, calculated, ○, experiment [22]); ---) Gaussian distribution with calculated σ_v , \bar{v}) average number of PFN per fission.

The average value of the excitation energy of a fragment in Eq. (5) was taken proportional to the average multiplicity of the PFN:

$$\bar{E}^*(A, Z, E_k) = \bar{v}(A, Z, E_k)(\bar{B}_n + \bar{\epsilon} + \bar{\delta}) + B_n/2, \quad (19)$$

where \bar{v} and $\bar{\epsilon}$ are the average values of the number and kinetic energy of PFN, which for the calculations were taken from experimental data, \bar{B}_n and $\bar{\delta}$ are the cascade average values of the binding energy of a neutron and the correction for parity in the semiempirical mass formula. In this determination of \bar{E}^* the calculated values of \bar{v} agree with the experimental values within the limits of error of the measurements. If the experimental values of the variance of the excitation energy σ_{E^*} were known, they were used in the calculations; other-

$$\sigma^2 = \sigma_{E^*}^2(A_H, Z_H, \bar{E}_k^H) + \sigma_{E^*}^2(A_L, Z_L, \bar{E}_k^L);$$

$$\sigma_{E^*}(A_H, Z_H, \bar{E}_k^H) / \sigma_{E^*}(A_L, Z_L, \bar{E}_k^L) = \bar{E}_H^* / \bar{E}_L^*, \quad (20)$$

where σ^2 is the variance of the kinetic energy of a fragment pair, and \bar{E}_k^H and \bar{E}_k^L are the average values of the kinetic energy of the fragments.

The multiplicity distribution of neutrons for a fragment pair was calculated by assuming the statistical independence of neutron emission from fragment pairs, since the correlation coefficients derived in [12] are small:

$$P_p(v) = \sum_{v_1}^v W_L(v_1) W_H(v - v_1). \quad (21)$$

The total multiplicity distribution $P(v)$ per fission was determined by using its average over the mass distribution in a manner similar to Eq. (1).

Since the results of the calculation depend on the choice of the necessary model parameters, we performed calculations to determine the effect of the parameters used on various characteristics of the PFN. In [13] PFN spectra calculated in the center of mass system were compared with experimental values for separate fragment masses and kinetic energies, which showed that within the limits of experimental error the model considered describes the PFN spectra without the nonequilibrium component. Calculations [14] showed that the probability of the emission of neutrons with $E > 10$ MeV depends strongly on the variation of the parameters of the initial distribution of the excitation energy of the fragments (5). For example, a change of the average value of the excitation energy of a fragment by ± 1 MeV leads to a change of the probability of the emission of fragments with $E = 10$ MeV by $\sim \pm 30\%$. But since the uncertainty of the input parameters has a random character, the average over many fragments in the calculation of the integral spectrum decreases the error of the final result.

To shorten the machine time for the calculation of the PFN integral spectrum, the averaging over the distribution of the kinetic energy of the fragments was replaced by selecting the parameters of the initial excitation energy distribution corresponding to \bar{E}_k (Fig. 1). The average values of the kinetic energy of the fragments \bar{E}_k , the number of neutrons, and their energy \bar{E} in the center of mass system were taken from [17], and the variance σ^2 of the kinetic energy of a fragment pair and the excitation energy of the light fragment were taken from [12]. The variance of the excitation energy of the heavy fragment was determined from the first of Eqs. (20). Figure 1 shows that the theoretical spectrum is below the Maxwellian for $E < 0.5$ MeV and $E > 5$ MeV, but within the limits of error of the measurements it describes the experimental results well. We extended our calculations to lower neutron energies, and found them closer to the experimental data than [15]. The results for the thermal-neutron fission of ^{235}U are shown in Fig. 2. The necessary input data for \bar{E}_k and σ^2 were taken from [20], and $\bar{\nu}(A, Z)$ was taken from [21]. The variance of the excitation energy of the fragments was determined from Eq. (20). Our calculations agree with the results in [5], but give a better description of the experimental data for PFN energies from 10 keV to 10 MeV. The fact that the theoretical spectrum is above the Maxwellian for energies > 10 MeV is apparently due to the uncertainty of the input data. Using the same input parameters, we calculated the multiplicity distributions of PFN for the spontaneous fission of ^{252}Cf and the thermal-neutron fission of ^{235}U (Fig. 3), and compared them with the experimental data [22]. The calculated distributions of the multiplicity of PFN are well described by Gaussian distributions with $\sigma_v^2 = 1.46$ for the spontaneous fission of ^{252}Cf , and $\sigma_v^2 = 1.23$ for the thermal-neutron fission of ^{235}U .

A comparison with experimental data shows that the calculation of the characteristics of PFN within the framework of the Hauser-Feshbach model of the emission of neutrons from completely accelerated fragments gives a good description of the PFN spectra for $E < 15$ MeV. The increased neutron yield for $E > 20$ MeV observed in [23] is not explained in the statistical model under the usual assumptions of the characteristics of fission fragments. Within the framework of the method described it is possible to calculate the characteristics of PFN from the low-energy fission of nuclei, when the lifetime of excited fragments is longer than their acceleration time. A comparison of our calculations of PFN spectra with those calculated in [5, 6] by simplified methods, shows that all three calculations give nearly the same result, but the Hauser-Feshbach statistical method is more general, and permits more reliable

LITERATURE CITED

1. V. M. Gorbachev, Yu. S. Zamyatnin, and A. A. Lbov, The Interaction of Radiation with Heavy Nuclei (Handbook) [in Russian], Atomizdat, Moscow (1976).
2. H. Bowman, J. Milton, S. Tompson, and W. Swiatecki, Phys. Rev., 126, 2120-2136 (1962).
3. V. A. Rubchenya, "On a possible mechanism of the emission of prompt fission neutrons," Preprint RI-28 [in Russian], (1974).
4. V. P. Zommer, A. E. Savel'ev, and S. V. Zhikhareva, "Prompt fission neutrons and γ rays and level density parameters of fragment nuclei from the spontaneous fission of ^{252}Cf ," At. Energ., 23, 327-333 (1967).
5. D. Madland and J. Nix, Nucl. Sci. Eng., 81, 213-271 (1982).
6. H. Merten, D. Neumann, and D. Seeliger, in: Proc. of IAEA Consultants' Meeting on the ^{252}Cf Fission Neutron Spectrum, Vienna, IAEA (1983), pp. 199-212.
7. J. Browne and F. Dietrich, Phys. Rev., 10C, 2545-2549 (1974).
8. A. V. Ignatyuk, G. N. Smirenkin, and A. S. Tishin, "Phenomenological description of the energy dependence of the level density parameter," Yad. Fiz., 21, 485-490 (1975).
9. O. I. Batenkov, A. B. Blinov, M. V. Bainov, and S. N. Smirnov, "Correlation of the angular and energy distributions of neutrons in the spontaneous fission of ^{252}Cf ," in: Neutron Physics, Part 1 [in Russian], TsNIIatominform, Moscow (1984), pp. 339-343.
10. F. Becchetti and G. Greenlees, Phys. Rev., 182, 1190-1209 (1969).
11. F. Dietrich, J. Browne, W. O'Connell, and M. Kay, Phys. Rev., 10C, 795-802 (1974).
12. H. Nifenecker, C. Signarbieux, and J. Poitou, in: Proc. of the Symposium on Physics and Chemistry of Fission, Vienna: IAEA, 2, 117 (1974).
13. O. I. Batenkov, A. B. Blinov, M. V. Blinov, et al., "Differentiated energy spectra of neutrons in the spontaneous fission of ^{252}Cf ," in: Neutron Physics, Part 1 [in Russian], TsNIIatominform, Moscow (1984), pp. 344-349.
14. B. F. Gerasimenko and V. A. Rubchenya, "Statistical calculation of prompt neutron spectra in the spontaneous fission of ^{252}Cf : Preprint RI-183 [in Russian], (1984).
15. D. Madland and R. LaBauve, Preprint LA-UR-84-129.
16. M. V. Blinov, G. S. Boykov, and V. A. Vitenko, in: Nuclear Data for Science and Technology, Antwerp, Sept. 6-10, 1982. Reidel Publ. Co. (1983), pp. 161-173.
17. V. M. Piksaikin, P. P. D'yachenko, and L. S. Kutsaeva, "Number and spectra of neutrons for specified fragments in the spontaneous fission of ^{252}Cf ," Yad. Fiz., 25, 723-731 (1977).
18. A. A. Boitsov, A. F. Semenov, and B. I. Starostov, "Relative measurements of the spectra of prompt fission neutrons for $^{235}\text{U} + n_T$, $^{235}\text{U} + n_T$, $^{239}\text{Pu} + n_T$ in the energy range 0.01-5 MeV," in: Neutron Physics, Part 2 [in Russian], TsNIIatominform, Moscow (1984), pp. 294-297.
19. L. Cranberg, G. Frye, N. Nereson, and L. Rosen, Phys. Rev., 103, 662-670 (1956).
20. J. Milton and J. Fraser, Can. J. Phys., 40, 1626-1663 (1962).
21. J. Milton and J. Fraser, in: Proc. of the Symposium on Physics and Chemistry of Fission, Vol. 2, Vienna: IAEA (1965), pp. 39-53.
22. J. Terrell, *ibid.*, pp. 3-24.
23. H. Merten, D. Seeliger, and B. Stobinski, in: Proc. of IAEA Consultants' Meeting on the ^{252}Cf Fission Neutron Spectrum, Vienna, IAEA (1983), pp. 195-198.

MEASUREMENT OF THE FAST-NEUTRON FISSION CROSS SECTIONS OF ^{231}Pa AND ^{243}Am

B. I. Fursov, E. Yu. Baranov,
M. P. Klemyshev, B. F. Samylin,
G. N. Smirenkin, and Yu. M. Turchin

UDC 539.173.84

We have measured the fission cross section ratios $^{231}\text{Pa}/^{239}\text{Pu}$ and $^{243}\text{Am}/^{239}\text{Pu}$ in the energy range $E_n = 0.135\text{--}7.4$ MeV by the method described in [1]. We felt it urgent to measure the ^{243}Am fission cross section because of the considerable (up to 30%) divergence of the results in [2-6] in the "plateau" region ($E_n = 2\text{--}5$ MeV). Detailed measurements of the energy dependence of the ^{231}Pa fission cross section were made in [7] with high resolution for neutron energies from 0.1 to 10 MeV. These data, normalized to the results in [8], differ substantially from earlier data of other experimenters in magnitude and in the shape of the energy dependence.

The measurements were performed with neutrons from the ^7Li (p, n) ^7Be , T (p, n) ^3He , and D (d, n) ^3He reactions at electrostatic accelerators. Solid targets of lithium fluoride or scandium hydride were used. Fission fragments were recorded by an ionization chamber. The fission cross section ratios $^{231}\text{Pa}/^{239}\text{Pu}$ and $^{243}\text{Am}/^{239}\text{Pu}$ were measured simultaneously by using two back-to-back ionization chambers. Layers of ^{239}Pu , ^{231}Pa , and ^{243}Am oxides were deposited on aluminum and platinum (Pa) backings of diameter 12 (Am/Pu) and 15 mm (Pa/Pu). The layer thicknesses were, respectively, 220, 212, and 129 $\mu\text{g}/\text{cm}^2$. The isotopic purity was 100% for ^{231}Pa , 99.891% (0.109% ^{240}Pu) for ^{239}Pu , and $97.3 \pm 0.1\%$ (2.7% ^{241}Am) for ^{243}Am . The last sample contained additional small admixtures of ^{242}Cm ($\sim 8.5 \times 10^{-6}\%$) and ^{244}Cm ($9.1 \times 10^{-3}\%$), which determined the spontaneous fission background. The spontaneous fission rate was measured with an error of 0.4%, determined from the scatter of results during the whole period of operation at the accelerators. The spontaneous fission in the layer of ^{243}Am contributed up to 40% of the total number of fissions for $E_n = 135$ keV, but not over 1-2% for $E_n > 1$ MeV.

The ratio of the numbers of fissile nuclei in the layers was determined by comparing their alpha activities in "good" geometry with a surface barrier semiconductor detector. The values of the half-lives in years were taken from [9]: ^{239}Pu , 24110 ± 30 ; ^{231}Pa , 32760 ± 110 ; ^{243}Am , 7380 ± 40 . The total error of the determination of the ratio of the numbers of fissile nuclei was: $^{231}\text{Pa}/^{239}\text{Pu}$, 0.9%; $^{243}\text{Am}/^{239}\text{Pu}$, 1%, including the uncertainties in the alpha decay constants. The efficiency of recording fission fragments was estimated by extrapolating the amplitude spectra to a zero level of discrimination. The efficiency was 92% for ^{231}Pa , 98% for ^{243}Am , and 97.5% for ^{239}Pu .

The estimates of the efficiency of recording fission fragments for neutron energies of 2 and 2.5 MeV were checked by measuring the ratios of the fission cross sections with cylindrical glass detectors [1]. In this case the efficiency of recording fragments is determined by geometrical factors which were maintained identical to a high degree of accuracy. A small correction for the dependence of the recording efficiency on the angular anisotropy of the fission fragments was introduced by taking account of the values of the anisotropy obtained in the same experiment. For $E_n = 2$ MeV, $W(0^\circ)/W(90^\circ) = 1.133 \pm 0.010$ for ^{239}Pu ; 1.067 ± 0.013 for ^{231}Pa ; 1.123 ± 0.011 for ^{243}Am . For $E_n = 2.5$ MeV, $W(0^\circ)/W(90^\circ) = 1.144 \pm 0.012$ for ^{239}Pu ; 1.099 ± 0.010 for ^{231}Pa ; 1.120 ± 0.014 for ^{243}Am .

The values of the fission cross section ratios measured by the two methods agreed to within 1% for $^{231}\text{Pa}/^{239}\text{Pu}$, and within 0.9% for $^{243}\text{Am}/^{239}\text{Pu}$. These uncertainties were taken as the error of the determination of the ratio of the ionization chamber efficiencies. The energy dependence of the efficiency associated with the change in the fraction of fragments absorbed in the fissile layer was taken into account by a small calculated correction (0.3-1.2%).

Translated from *Atomnaya Energiya*, Vol. 59, No. 5, pp. 339-343, November, 1985. Original article submitted January 25, 1985.

E_n , MeV	ΔE_n , keV	σ_{f1}/σ_{f0}	$\Delta\sigma_{f1}/\sigma_{f0}$, %	σ_{f2}/σ_{f0}	$\Delta\sigma_{f2}/\sigma_{f0}$, %	σ_{f2}^* , b	σ_{f1} , b	σ_{f2} , b
0.135	32	0.0036	5.3	0.0063	7.5	1.552	0.0056	0.0098
0.175	30	0.0087	5.1	0.0065	6.8	1.507	0.0131	0.0098
0.215	28	0.0090	5.2	0.0073	6.6	1.503	0.0135	0.0110
0.255	26	0.0082	5.8	0.0093	6.4	1.522	0.0125	0.0142
0.305	24	0.0296	4.7	0.0102	6.2	1.549	0.0458	0.0158
0.350	49	0.0363	3.4	0.0118	5.1	1.564	0.0568	0.0184
0.400	46	0.0416	4.0	0.0135	3.6	1.573	0.0654	0.0212
0.450	44	0.0858	3.7	0.0169	3.4	1.581	0.136	0.0267
0.500	43	0.193	2.4	0.0242	3.0	1.590	0.307	0.0385
0.550	41	0.270	2.3	0.0346	2.9	1.601	0.432	0.0554
0.600	40	0.253	2.2	0.0465	2.8	1.612	0.408	0.0750
0.650	39	0.252	2.1	0.0642	2.8	1.618	0.408	0.104
0.700	38	0.272	2.0	0.0962	2.6	1.638	0.446	0.158
0.750	38	0.299	2.1	0.138	2.8	1.681	0.503	0.232
0.800	37	0.376	2.0	0.193	2.3	1.717	0.646	0.331
0.850	36	0.456	2.1	0.263	2.2	1.716	0.782	0.451
0.900	36	0.459	2.1	0.365	2.1	1.705	0.782	0.622
0.950	36	0.460	2.0	0.466	2.2	1.710	0.787	0.797
1.00	35	0.468	1.9	0.572	2.0	1.724	0.807	0.986
1.05	35	0.483	1.9	0.642	2.1	1.736	0.838	1.114
1.10	35	0.496	1.9	0.687	2.0	1.754	0.870	1.205
1.15	35	0.493	1.8	0.717	2.0	1.784	0.880	1.279
1.20	35	0.505	1.8	0.729	1.9	1.817	0.918	1.325
1.25	35	0.512	1.8	0.725	1.9	1.848	0.946	1.340
1.30	35	0.516	1.8	0.734	1.9	1.876	0.968	1.377
1.35	35	0.515	1.8	0.736	1.8	1.903	0.980	1.401
1.40	36	0.518	1.8	0.740	1.8	1.924	0.997	1.424
1.45	36	0.520	1.8	0.742	1.8	1.935	1.006	1.436
1.50	36	0.533	1.8	0.739	1.7	1.939	1.033	1.433
1.60	75	0.549	1.8	0.729	1.7	1.933	1.061	1.409
1.70	74	0.573	1.7	0.721	1.6	1.934	1.108	1.394
1.80	73	0.582	1.7	0.716	1.6	1.949	1.134	1.395
1.90	72	0.586	1.7	0.722	1.7	1.959	1.148	1.414
2.00	71	0.591	1.7	0.729	1.6	1.963	1.160	1.431
2.10	70	0.588	1.7	0.740	1.7	1.962	1.154	1.452
2.20	69	0.595	1.7	0.740	1.7	1.953	1.162	1.445
2.30	68	0.598	1.7	0.754	1.7	1.938	1.159	1.461
2.40	68	0.596	1.7	0.760	1.7	1.917	1.142	1.457
2.50	67	0.596	1.7	0.769	1.7	1.898	1.131	1.459
2.60	66	0.596	1.7	0.765	1.7	1.884	1.123	1.441
2.70	66	0.591	1.7	0.773	1.7	1.874	1.108	1.449
2.80	65	0.592	1.7	0.776	1.7	1.864	1.103	1.446
2.90	65	0.589	1.8	0.780	1.7	1.854	1.092	1.446
3.00	65	0.580	1.7	0.779	1.8	1.844	1.070	1.436
3.10	65	0.575	1.8	0.781	1.8	1.833	1.054	1.432
3.20	65	0.572	1.8	0.787	1.8	1.823	1.043	1.435
3.30	65	0.573	1.8	0.787	1.7	1.817	1.041	1.430
3.40	66	0.569	1.8	0.792	1.8	1.812	1.031	1.435
3.50	66	0.572	1.9	0.794	1.8	1.801	1.030	1.430
3.60	66	0.572	1.9	0.800	1.8	1.783	1.020	1.426
3.80	240	0.570	1.9	0.813	1.7	1.756	1.001	1.428
4.00	174	0.569	1.8	0.819	1.6	1.739	0.989	1.424
4.20	161	0.565	1.8	0.822	1.7	1.732	0.978	1.424
4.40	142	0.560	1.8	0.829	1.7	1.723	0.965	1.428
4.60	133	0.558	1.8	0.832	1.7	1.709	0.954	1.422
4.80	118	0.559	1.9	0.847	1.7	1.690	0.945	1.431
5.00	112	0.553	1.9	0.855	1.8	1.673	0.925	1.430
5.20	106	0.546	2.0	0.858	1.8	1.667	0.910	1.430
5.40	104	0.533	2.0	0.866	1.8	1.669	0.890	1.445
5.60	102	0.512	2.0	0.857	1.9	1.684	0.862	1.443
5.80	125	0.516	2.1	0.845	2.1	1.724	0.890	1.457
6.00	122	0.565	2.3	0.834	2.2	1.786	1.001	1.489
6.20	120	0.632	2.5	0.870	2.3	1.864	1.178	1.622
6.40	117	0.674	2.4	0.919	2.4	1.937	1.306	1.780
6.60	116	0.718	2.5	0.929	2.4	1.992	1.430	1.851
6.80	116	0.755	2.5	0.952	2.4	2.023	1.527	1.926
7.00	117	0.809	2.6	0.959	2.5	2.075	1.679	1.990
7.20	118	0.831	2.8	0.974	2.6	2.123	1.764	2.068
7.40	119	0.866	2.8	0.980	2.6	2.169	1.878	2.126

*Reference values of σ_f for ^{239}Pu were taken from ENDF/B V, averaged over the energy resolution.

The components of the neutron background were measured experimentally as described in [1]. The correction for neutron scattering from the accelerator target reached 5-7% in the subthreshold region ($E_n = 0.135$ -1 MeV), but did not exceed 0.3-1.8% for $E_n > 1.5$ MeV. Taking account of the background in the laboratory led to a 0.4% correction of the cross section ratio for $^{243}\text{Am}/^{239}\text{Pu}$, and 0.7% for $^{231}\text{Pa}/^{239}\text{Pu}$. The background of the concomitant (d, n) reactions reached 35% for 7.4 MeV. The related correction of the fission cross section ratios

TABLE 2. Corrections and Errors of the
Measurement of Fission Cross Section
Ratios for an Energy of 2.5 MeV, %

Source of corrections and errors	$^{231}\text{Pa}/^{239}\text{Pu}$		$^{243}\text{Am}/^{239}\text{Pu}$	
	cor- rec- tion	error	cor- rec- tion	error
Measurement of ratio of numbers of fissile nuclei by a comparison of alpha activities	—	0,9	—	1,0
Determination of ratio of efficiencies of re- cording fission frag- ments	—	1,0	—	0,9
Difference of neutron fluxes through fissile layers	1,4	0,5	2,1	0,5
Systematic part of error		1,4		1,4
Statistical error	—	0,4	—	0,5
Allowance for spon- taneous fission	—	—	0,4	< 0,1
Fission of isotopes of admixture	< 0,1	< 0,1	3,4	0,3
Energy dependence of ratio of fission chamber efficiencies	0,8	0,3	0,6	0,3
Neutron background in laboratory	0,7	0,2	0,4	0,2
Background of neutrons scattered from target	0,6	0,2	0,8	0,3
Inelastic scattering of neutrons	—	0,5	—	0,5
Background of neutrons accompanying (p, n) reactions	2,3	0,5	2,0	0,5
Error of energy dependence		0,9		1,0
Total error		1,7		1,7

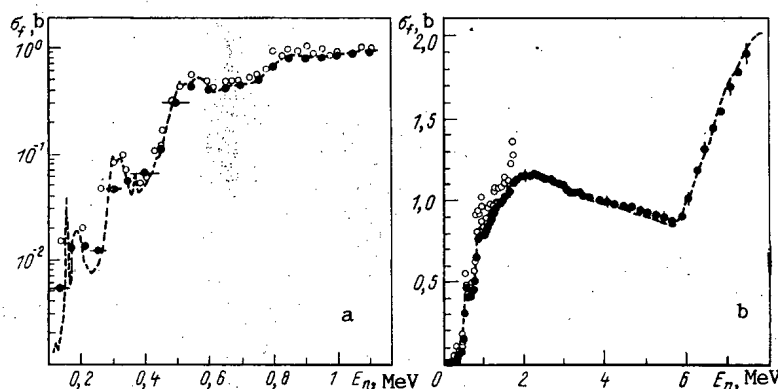


Fig. 1. Fast-neutron fission cross section of ^{231}Pa : a) subbarrier region b) plateau region; ●) our results; ○) [10]; ---) data averaged over many values [7].

in the range 3.8–7.4 MeV was 0.2–11.4%. The analogous correction for (p, n) reactions in the range 2–3.6 MeV was 0.3–4.9%. We did not introduce separate corrections for the inelastic scattering of neutrons from the detector walls, backings, and the electrodes of the ionization chamber, but included an upper estimate (0.5%) of the possible effect in the total error.

The results of the measurements are listed in Table 1. The total error shown is the rms sum of all the uncertainties determined. Table 2 shows the structure of the characteristic corrections and errors of the measurements performed at 2.5 MeV. The systematic part of

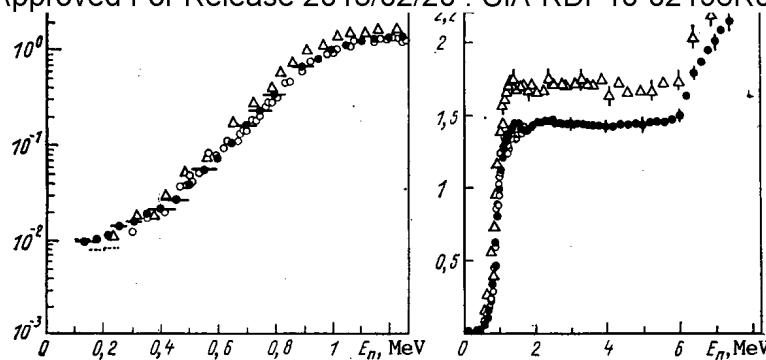


Fig. 2. Fast-neutron fission cross section of ^{243}Am
 ●) our results; Δ) [2]; \circ) [3]; ---) [11].

the error (1.4%) correlated with the whole energy range studied, and the error due to the uncertainty of the energy dependence (0.9 and 1%) are separated from the total error. The total error of the results is 1.7-2% in the range 1-5.6 MeV, 2.6-2.8% at 7.4 MeV as a result of corrections for the background of the (d, n) reactions, and 6-7.5% for $E_n < 0.3$ MeV because of the worsening of the statistical accuracy of the measurements, taking account of the spontaneous fission of ^{243}Am and the introduction of the maximum corrections for neutron scattering.

To compare the experimental results obtained we calculated the ^{243}Am and ^{231}Pa fission cross sections from the values of the ratios by using the ^{239}Pu fission cross sections from ENDF/B V averaged over the energy resolution.

Figure 1 compares our measured values of the ^{231}Pa fission cross section with data of other experimenters. Our data are in good agreement with those of [7] in absolute value and in the shape of the energy dependence over the whole range $E_n > 1.5$ MeV, which also confirms agreement with the results in [8], in terms of which the data in [7] were normalized. The appreciable divergences in the subbarrier region are accounted for by the large difference in energy resolution.

The results obtained for the shape of the energy dependence agree with those in [10], but the latter are 10-15% higher.

Figure 2 shows the ^{243}Am fission cross section. Our results agree with those in [3] in magnitude and in the shape of the energy dependence. The data in [2] are 15-20% higher than our values, but agree well with them in the shape of the energy dependence. A certain decrease of the divergence for $E_n > 6$ MeV may be related to a difference in the standards used: ^{239}Pu in our work, ^{235}U in [2, 3, 6, 7]. Our value of the ^{243}Am fission cross section is lower than that in [2], but it agrees with the estimate of the cross section in the plateau region (1.411 ± 0.067) b [6]. For $E_n < 250$ keV our results agree with those in [11] within the limits of combined errors.

The authors thank B. F. Myasoedov and L. A. Ivanovaya for assistance in the work, and S. E. Lavrov and V. I. Ivanov for help in preparing the fissile layers.

LITERATURE CITED

1. B. I. Fursov et al., *At. Énerg.*, **43**, 161, 261, (1977); **45**, 440 (1978); **55**, 31 (1983).
2. J. Behrens and J. Browne, *Nucl. Sci. Eng.*, **77**, 444 (1981).
3. D. Butler and R. Sjöblom, *Phys. Rev.*, **124**, 1129 (1961).
4. P. Seeger, Rep. LA-4420 (1970).
5. H. Britt and J. Wilhelmy, *Nucl. Sci. Eng.*, **72**, 222 (1979).
6. E. F. Fomushkin et al., *Problems of Atomic Science and Technology. Ser. Nuclear Constants No. 3* (57) [in Russian], (1984), p. 17.
7. S. Plattard et al., in: *Proc. Conf. on Nuclear Cross Sections and Technology*, Knoxville, NBS (1979), p. 491.
8. A. Sicre, Ph. D. Thesis, University of Bordeaux (1976), Report CENBG 7603.
9. A. Lorenz, "Proposed recommended list of heavy element radionuclide decay data," Rep. INDC(NDS)-149/NE (1983).
10. S. M. Dubrovina and V. A. Shigin, *Dokl. Akad. Nauk SSSR*, **157**, 561 (1964).
11. K. Wisshak and F. Kappeler, *Nucl. Sci. Eng.*, **85**, 251 (1983).

MEASUREMENT OF THE MEAN-ENERGY DIFFERENCES IN THE FISSION-NEUTRON SPECTRA
OF ^{233}U , ^{235}U , ^{239}Pu , AND ^{252}Cf

V. I. Vol'shov and G. N. Smirenkin

UDC 539.173.84

There are some inconsistencies among studies on the fission-neutron spectra of the principal nuclides, involving the spectrum shape and characteristic parameters, and primarily the mean spectrum energy \bar{E} . The discrepancies stem from experimental systematic errors which are difficult to take into account, but which, as a review of [1] and [2] shows, can largely be eliminated by relative measurements. Although this approach has been used earlier, it became well established in recent years when the spontaneous-fission spectrum of ^{252}Cf was adopted as a standard for fast-neutron spectra [3] thanks to the high-accuracy data compiled from the measurement results of various research groups. A fission-neutron spectrum can obviously be obtained with greater ease and reliability by reference to such a standard than by means of absolute measurements. As a case in point, consider the determination of the mean spectrum energy \bar{E} .

Experimental data on fission-neutron spectra are commonly described by Maxwell's distribution

$$N(E, \theta) = 2 \left(\frac{E}{\pi \theta^3} \right)^{1/2} \exp \left(-\frac{E}{\theta} \right), \quad (1)$$

where the temperature θ and the mean energy are related by $\bar{E} = 3/2 \theta$.

In the spontaneous fission of ^{252}Cf , $\theta_0 = 1.42$ MeV and $E = 2.13$ MeV [3]. The logarithm of the ratio between the standard and the studied spectrum is a linear function of the neutrons, i.e.,

$$\ln \frac{N(E, \theta_0)}{N(E, \theta)} = a(\theta, \theta_0) + b(\theta, \theta_0) E. \quad (2)$$

Given the coefficient $b(\theta, \theta_0) = \theta^{-1} - \theta_0^{-1}$, it is possible to determine the desired parameter or the parameter difference $\Delta\theta = \theta_0 - \theta$, viz.,

$$\theta = \frac{\theta_0}{1 + b\theta_0}, \quad \Delta\theta = \frac{b\theta_0^2}{1 + b\theta_0}, \quad (3)$$

TABLE 1. Calculated Values of $b(\theta, \theta_0)$, $\Delta\theta$, and $\Delta\bar{E}$

Series	^{233}U			^{235}U			^{239}Pu		
	$b(\theta, \theta_0)$, $\text{MeV}^{-1} \cdot 10^{-2}$	$\Delta\theta$, keV	$\Delta\bar{E}$, keV	$b(\theta, \theta_0)$, $\text{MeV}^{-1} \cdot 10^{-2}$	$\Delta\theta$, keV	$\Delta\bar{E}$, keV	$b(\theta, \theta_0)$, $\text{MeV}^{-1} \cdot 10^{-2}$	$\Delta\theta$, keV	$\Delta\bar{E}$, keV
I	—	—	—	5.97 ± 0.41 5.94 ± 0.42	112 ± 8 111 ± 8	168 ± 12 166 ± 12	2.95 ± 0.40 2.89 ± 0.40	59 ± 9 58 ± 9	88 ± 14 87 ± 14
II	—	—	—	5.74 ± 0.42 5.51 ± 0.44	108 ± 8 104 ± 9	162 ± 12 156 ± 14	2.25 ± 0.40 2.09 ± 0.48	46 ± 8 43 ± 10	69 ± 12 64 ± 15
III (stilbene)	4.10 ± 0.72 4.04 ± 0.74	80 ± 14 79 ± 15	120 ± 22 119 ± 23	6.26 ± 0.99 6.20 ± 1.13	117 ± 18 116 ± 20	175 ± 27 174 ± 30	2.15 ± 0.58 2.20 ± 0.58	44 ± 12 42 ± 12	66 ± 18 63 ± 18
III (anthracene)	3.54 ± 0.83	70 ± 16	105 ± 24	5.80 ± 0.82	109 ± 15	164 ± 22	1.62 ± 0.63	34 ± 13	51 ± 20
Mean-weighted value	—	80 ± 14 79 ± 15	120 ± 22 119 ± 23	—	110 ± 5 108 ± 5	165 ± 8 162 ± 8	—	51 ± 6 49 ± 6	76 ± 9 74 ± 9

Note. The energy interval in the numerator is 1-10.5 MeV, and in the denominator 1-8 MeV; for series III the interval is 1-6.5 MeV.

Translated from Atomnaya Energiya, Vol. 59, No. 5, pp. 343-345, November, 1985. Original article submitted February 1, 1985.

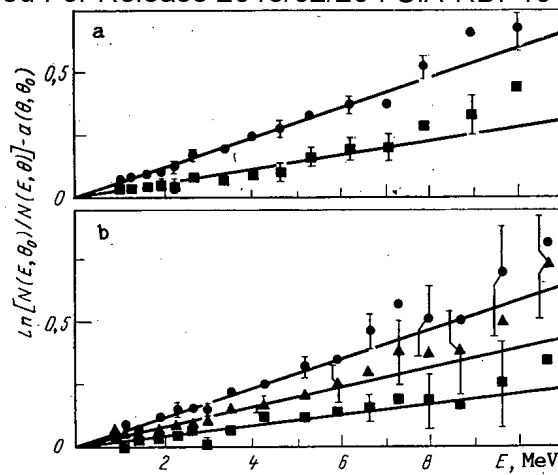


Fig. 1. Measurement results for series I and II combined (a) and series III (b): experimental data for ^{233}U (Δ), ^{235}U (\bullet), and ^{239}Pu (\blacksquare); the lines represent the experimental data plotted from (2) by the least-squares method.

TABLE 2. Comparison of Published Values of $\Delta\bar{E} = E_0 - \bar{E}$, keV, for $E_0 = 2.13$ MeV

Reference	^{233}U	^{235}U	^{239}Pu
This study	119 ± 23	162 ± 8	74 ± 9
[1]	114 ± 19	184 ± 12	58 ± 18
[2]	123 ± 30	157 ± 24	76 ± 29
ENDF/B V [3]	56,9	99,2	18,0
BNAB -78 [8]	153	160	107

Note. The energy interval is 1-8 MeV, and for ^{239}Pu [2], 1-10 MeV.

where

$$\Delta\theta/\theta_0 \approx b\theta_0 \ll 1. \quad (4)$$

When $N(E, \theta)$ is measured directly, the entire energy calibration error $\delta E/E$ figures in the error $\delta\theta/\theta$, while if the spectrum ratio is measured, the much smaller quantity $\frac{\Delta\theta}{\theta_0} \frac{\delta E}{E}$ is involved, as follows from (2) and (4). In relative measurements it is not necessary to know the efficiency of the neutron detector used to determine $N(E, \theta)$, and it is easy to take alternate readings of the studied and standard spectra in order to suppress the effects of any instability in the recording equipment.

We applied this technique for a number of years to the measurement of neutron spectra in the low-energy fission of ^{233}U , ^{235}U , and ^{239}Pu and in the spontaneous fission of ^{252}Cf , using a gamma-discriminating single-crystal scintillation spectrometer. Some of the results were published in the form of $N(E, \theta)$ spectra [4, 5]. This article gives the cumulative data, processed by means of (2) and (3).

The principle of single-crystal fast-neutron spectrometry is described in detail in [4-6]. We consequently discuss here only specific features of the different experiments, which have been designated as measurement series I, II, and III. The measurements in series I were made on ^{233}U , ^{239}Pu , and the standard, using an electrostatic generator [4]. Metal disks of 1-mm ^{235}U and ^{239}Pu were placed within a fairly narrow solid angle aligned with a neutron beam whose energy was chosen close to the (p, n) reaction threshold, in order to achieve kinematic collimation of the neutrons. A stilbene detector was placed in the rear hemisphere, which received only the fission neutrons and the beam neutrons ($E < 80$ -100 keV) scattered by the test samples, the target, and the room walls. Further measurements were carried out in a

Declassified and Approved For Release 2013/02/20 : CIA-RDP10-02196R000300070005-0
 similar setup, using a neutron generator (series 11). The tests in series III included the fission-neutron spectrum of ^{233}U in addition to the above nuclei. The measurements were made using the thermal-neutron beam of a BR-10 reactor with crystals of stilbene ($E \leq 11$ MeV) and anthracene ($E \leq 6.5$ MeV) [5].

The energy calibration of the spectrometers consisted essentially of determining the light yield as a function of the neutron energy; this was done by using monoenergetic neutrons in the range $E = 1\text{--}17$ MeV [5]. The crystals employed in the experiments were 30 mm in diameter and 30 mm high for stilbene, and 30 mm in diameter and 20 mm high for anthracene.

The spectrometrically recorded recoil-neutron energy (E_p) distribution

$$N(E_p) = C \int_{E_p}^{\infty} N(E, \theta) P(E_p, E) dE \quad (5)$$

was processed to obtain the neutron spectrum $N(E, \theta)$, either by solving Eq. (5) with a real line $P(E_p, \theta)$ or by straightforward differentiation with the line in step form, i.e.,

$$P(E_p, E) = \begin{cases} \frac{1}{E} \left\{ 1 - \exp \left[- \sum (E) h \right] \right\} & \text{for } E_p \leq E; \\ 0 & \text{for } E_p > E, \end{cases}$$

the results being similar in both cases [4]. The values given in this paper were obtained by the second, simpler, method for all the measurement series. Figure 1 shows the logarithm of the ratio between the standard and studied spectra. For the sake of compactness (to make the lines pass through the origin), the experimental data are represented with the ordinates plotted as $\ln N(E, \theta_0)/N(E, \theta) - \alpha(\theta, \theta_0)$. The slope of the lines, given by $b(\theta, \theta_0)$, defines the difference of the parameters θ , and thus the mean-energy difference in the spectra under comparison.

Table I lists the values calculated for all the series. Each series combines several measurements of $N(E, \theta)$ and $N(E, \theta_0)$ in fairly close agreement; the differences $\Delta\theta = \theta_0 - \theta$ were calculated from (3). Some small neutron-multiplication corrections were introduced in $\Delta\theta$, according to the relationship between θ (or \bar{E}) and the mean fission-neutron yield as given by Terrell [7]. The delayed-neutron contribution in the recorded distributions (above 1 MeV) was neglected. The measurement results obtained in different years under different conditions are in good agreement. We note that the parameter error fits well the counting statistics in the different series (between $2 \cdot 10^6$ and 10^7 events), and that there is no statistically significant variation of the parameters with the energy-interval width ΔE . The final result does not contain any appreciable systematic errors due either to possible deviations of the actual spectra from distribution (1) or to the characteristics of the procedure employed (Table 2).

The results of [1] and [2] are in good agreement, and they differ appreciably from the parameters in ENDF/B V and BNAB-78. In ENDF/B V the values for $\Delta\bar{E}$ are understated, though they fit the variations observed among the nuclei. In BNAB-78 the value of \bar{E} is determined from Terrell's semiempirical formula, which involves the parameter ν alone. This is a highly simplified representation of $\bar{E}(Z, A)$, and it should not be used in a well-designed study.

LITERATURE CITED

1. L. M. Andreichuk, B. G. Basova, and V. A. Korostylev, "Relative measurement of the mean energies in the fission-neutron spectra of ^{233}U , ^{235}U , and ^{239}Pu ," *At. Énerg.*, **42**, No. 1, 23-25 (1977).
2. Smith et al., *Nucl. Sci. Eng.*, **76**, 357 (1980).
3. J. Grundl and C. Eisenhauer, *Natl. Bur. Stand. Publ.*, NB5-493 (1977).
4. Z. A. Aleksandrova, V. I. Bol'shov, and V. F. Kuznetsov, "Secondary-neutron spectra in the fission of ^{233}U and ^{239}Pu with 0.1-MeV neutrons," *At. Énerg.*, **38**, No. 2, 108-109 (1975).
5. V. I. Bol'shov, K. E. Volodin, V. G. Nesterov, and Yu. M. Turchin, "Neutron spectra in the thermal-neutron fission of ^{233}U , ^{235}U , and ^{239}Pu and in the spontaneous spectra fission of ^{252}Cf ," *Vopr. At. Nauk. Tekh., Ser. Yad. Konst.*, No. 3 (42), 43 (1981).
6. V. I. Kukhtevich, L. A. Trykov, and O. A. Trykov, *The Single-Crystal Scintillation Spectrometer* [in Russian], Atomizdat, Moscow (1971).
7. J. Terrell, *Phys. Rev.*, **113**, 527 (1959).

STUDY OF THE CHANGES IN THE ELECTRICAL RESISTIVITY AND MICROHARDNESS
OF VANADIUM AND NIOBIUM UNDER SEPARATE AND SUCCESSIVE IRRADIATION
WITH NEUTRONS, α -PARTICLES, AND ELECTRONS

P. K. Khabibullaev, T. B. Ashrapov,
A. K. Kakabadze, I. M. Neklyudov
V. N. Tkach, A. I. Fedorenko,
Kh. R. Yunusov, and V. A. Yamnitskii

UDC 621.039.539

In a fusion reactor the material surrounding the plasma is under the action of deuterium, tritium, and helium ions, neutral atoms, neutrons, and "runaway" electrons ($E = 0.5-1.5$ MeV). The interaction of particle fluxes from the plasma with the materials of the first wall, limiter, shields, and other units inside the discharge chamber leads to radiation damage in them.

Model studies carried out over the past two decades to ascertain how each of the corpuscular radiations emitted by a thermonuclear plasma affects the materials have provided considerable information about the coefficients and mechanisms of radiation erosion as well as the changes in the structure and properties of promising structural materials for fusion reactors. Under the actual conditions of power reactors, the structural materials will be irradiated by all forms of plasma emission almost simultaneously (the intensity of the fluxes of some forms of radiations, in particular "runaway" electrons, will have peak values at the beginning and end of the plasma discharge). As a consequence of synergism the integrated interaction of the corpuscular radiations of the plasma on the structural material of the discharge chamber can differ significantly from the simple sum of the interactions of the individual radiations [1].

In view of this it seems desirable to study the influence of irradiation with one form of corpuscular emission on the radiation damage caused in material irradiated with another form (or other forms) of emission. As the objects for our study we chose vanadium and niobium, whose vulnerability to radiation damage was estimated by measuring the electrical resistivity and microhardness.

Single-crystal specimens of vanadium and niobium were cut by the electrospark method from ingots grown by electron-beam zone refining in a vacuum. The mass fractions of gaseous

TABLE 1. Changes in the Characteristics
of Niobium and Vanadium After Irradiation

Type of irradiation	$\Delta\rho$, %		ΔH , %	
	V	Nb	V	Nb
Neutrons*	121,6	183,3	14,6	35,0
α -particles†	163,6	233,3	38,2	50,0
Neutrons + α -particles	195,4	283,3	51,7	75,0
Neutrons + α -particles + electrons‡	9,0	33,3	4,5	3,75

* $\phi = 1 \cdot 10^{21} \text{ cm}^{-2}$, $E \geq 0.18$ MeV.

† $E = 0.5-32$ MeV, $\phi = 1 \cdot 10^{17} \text{ cm}^{-2}$ for each energy.

‡ $E = 1.5$ MeV, $W = 2.4 \text{ MeV} \cdot \text{cm}^{-2}$, $N = 1000$.

Translated from Atomnaya Énergiya, Vol. 59, No. 5, pp. 345-348, November, 1985. Original article submitted March 11, 1984.

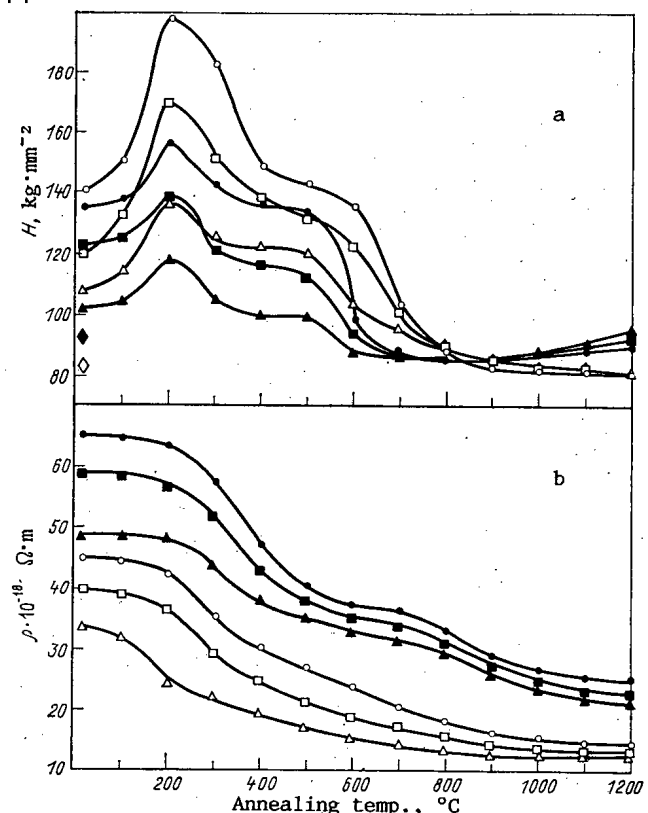


Fig. 1. Annealing-temperature dependence of the microhardness (a) and electrical resistivity (b) of vanadium (black symbols) and niobium (white symbols) single crystals irradiated at 200°C separately and successively with α -particles, neutrons (n^0), and electrons (e^-): \bullet , \circ) $n^0 + \alpha$; \blacksquare , \square) α ; \bullet , Δ) n^0 ; \blacktriangle , \diamond) $n^0 + \alpha + e^-$.

impurities in the single crystals were (in %): oxygen 0.008, hydrogen 0.0008, and carbon 0.015. From the Laue back-reflection patterns we established that the misorientation of the blocks of the mosaic did not exceed $10'$. The vanadium and niobium specimens were disks of orientation (112) and (110), diameter 12 and 18 mm, and thickness 0.5 and 0.3 mm, respectively. The specimens were first treated mechanically and electrochemically (surface roughness $\sim 0.5 \mu\text{m}$) and were then annealed in a vacuum at 1200°C for 1 h.

The irradiation was carried out at 200°C in three ways: separately in the VVR-SM reactor to a thermal-neutron fluence of $5.08 \cdot 10^{21} \text{ cm}^{-2}$ and fast-neutron flux of $1 \cdot 10^{21} \text{ cm}^{-2}$ ($E \geq 0.18 \text{ MeV}$); separately in a flux of accelerated α -particles to a fluence of $1 \cdot 10^{17} \text{ cm}^{-2}$ for each value of energy in the ESU-2 accelerator ($E = 0.5\text{--}1.5 \text{ MeV}$ in intervals of 0.2–0.3 MeV) and then in a U-150-2 cyclotron ($E = 2.0\text{--}40 \text{ MeV}$ in intervals of 1.5–3 MeV); and successively vanadium and niobium were irradiated with α -particles, as in the second method, then with neutrons, as in the first method, and finally with electrons in the ELIT-1.5 accelerator ($E = 1.5 \text{ MeV}$, energy release per pulse $W = 2.4 \text{ MW} \cdot \text{cm}^{-2}$, $\tau_p = 3 \mu\text{sec}$, pulse-duty factor 1 Hz, and number of pulses $N = 1000$).

To anneal the radiation-induced defects and to re-establish the properties of the material after each form of irradiation the specimens were heated in a vacuum to 1200°C with 100°C intervals in 1 h. After each of the forms of treatment (irradiation or annealing) we measured the electrical resistivity by the potentiometric method at room temperature and the microhardness on a PMT-3 instrument. The measuring accuracy was 0.1 and 3%, respectively. The irradiation conditions, the measuring procedure, and the results of the separate irradiations of the materials with neutrons, α -particles, and electrons were presented earlier in [2–4].

The distributions of the displaced and interstitial helium atoms after vanadium and niobium were bombarded with reactor neutrons and with α -particles were calculated on a BESM-6 computer using the IMITATOR program [5] while the temperature of the vanadium and niobium during high-power pulsed electron bombardment was estimated computationally with the aid of the KASKAD program [6].

Separate irradiation of vanadium and niobium with neutrons and α particles leads to an increase in their electrical resistivity ($\Delta\rho$) and microhardness (ΔG) (see Table 1). In the case of successive irradiation, first with α -particles and then with neutrons, the electrical resistivity increases by a factor of 1.2-1.5 and the microhardness increases by a factor of 1.5-3 in comparison with the effects of separate irradiation. Subsequent pulsed irradiation of the same specimens with electrons leads to a decrease in the electrical resistivity and microhardness to levels 9-30% and ~5%, respectively, above the initial levels (prior to irradiation). When specimens that have been irradiated separately and successively are annealed to 1200°C the same effect is observed (see Fig. 1) while in the case of annealing in the range 120-300°C the microhardness is observed to increase further above its value after irradiation.

The irradiation of vanadium and niobium single-crystals with neutrons and α -particles leads to the formation of various types of primary-damage zones, whose number, size, configuration, and relative position are determined by the irradiation conditions (type, energy, and fluence of particles and temperature, structure, and properties of the material). Neutron irradiation led to the formation of radiation damage, which amounted to 3 displacements per atom for vanadium and 2.5 displacements per atom for niobium.

In contrast to neutron bombardment, which produces in the bulk of the material a fairly uniform distribution of the primary-damage zones, bombardment with α -particles produced zones of primary damage and increased concentration of interstitial helium only at the end of the particle range. Consequently, discrete bombardment of vanadium and niobium with batches (up to 10^{17} cm⁻²) of accelerated α -particles with an energy of 0.5-40 MeV at intervals of 2-3 MeV was used to obtain a uniform distribution of radiation defects and helium in the bulk of the material. This led to practically the entire bulk of the irradiated specimens being overlapped by zones of radiation damage and helium implantation. In this case the following levels are attained (per atom): in vanadium - 7.09 displacements and $2.54 \cdot 10^{-2}$ interstitials in the surface layer and 4.5-1 displacements and $(7.63-3) \cdot 10^{-3}$ interstitials in the bulk; in niobium - 15.5 displacements and $3.47 \cdot 10^{-2}$ interstitials in the surface layer and 3-1.5 displacements and $1.39 \cdot 10^{-2}-4 \cdot 10^{-3}$ interstitials in the bulk of the specimen. The formation of different types of defect and impurity atoms in the material under irradiation leads to a considerable change in its basic properties, e.g., electrical resistivity and microhardness (see Fig. 1).

In vanadium and niobium the effects of radiation damage caused by successive bombardment with neutrons and α -particles are superimposed upon each other, leading to a cumulative effect that exceeds each of the individual effects.

The annealing of radiation defects when the irradiated materials were heated and, therefore, the restoration of the corresponding properties in connection with the presence of a radiation-defect spectrum should occur in several stages over a wide range of temperatures. The study and classification of stages in the annealing of defects in irradiated bcc metals [7-9] indicated the onset of radiation-annealing ordering when the irradiated specimens were heated to $(0.13-0.2) T_m$ [10-11]. As is seen from Fig. 1, additional hardening of vanadium and niobium take place in the range 150-250°C under both separate and successive irradiation with α -particles and neutrons. Such ordering of irradiated bcc metal was assumed to have an "impurity" nature [11].

When vanadium and niobium damaged by neutrons and α -particles are irradiated with batches of high-energy electrons the properties of the materials are restored (see Fig. 1). Calculations showed that under pulsed electron bombardment the temperature of the vanadium specimen rises by 50-70°C during each pulse and that of the niobium specimen rises by 100-165°C, reaching 1200-1500°C twenty minutes after the beginning of irradiation, with allowance for the heat losses through radiation from the surface of the specimen and heat transfer to the material of the substrate (electrical porcelain). Naturally, such heating of the material by pulsed electron bombardment leads to annealing of the radiation defects produced as a result of irradiation with α -particles and neutrons and even leads to the escape of helium from the bulk of the material.

The nature of the "damageability" of materials in future fusion reactors, in connection with the spectrum and energy of the bombarding particles as well as the sequence of the interaction events, is not always predictable on the basis of model tests under the conditions of one irradiation. In order to approximate the actual conditions under which the materials would operate it is necessary to carry out tests on the materials by simultaneously, or at least successively, bombarding them with the corpuscular emissions of a plasma.

LITERATURE CITED

1. M. I. Guseva, Yu. V. Martynenko, and N. V. Pleshivtsev, in: Study and Development of Fusion-Reactor Materials [in Russian], Nauka, Moscow (1981), pp. 106-115.
2. T. B. Ashrapov, N. Abdusalyamov, S. V. Artemov, et al., Vopr. At. Nauki Tekh. Ser. Fiz. Radiats. Povrezhdenii Radiats. Materialoved., No. 2(21), 53-58 (1982).
3. P. K. Khabibullaev, T. B. Ashparov, N. Abdusalyamov, et al., Izv. Akad. Nauk Uzb. SSR. Ser. Fiz.-Mat. Nauk, No. 5, 53-58 (1982).
4. L. A. Gromov, V. A. Kalyagin, Z. A. Mendeleeva, et al., Vopr. At. Nauki Tekh. Ser. Fiz. Radiats. Povrezhdenii Radiats. Materialoved., No. 1(24), 62-70, (1983).
5. V. V. Gann, A. M. Vaisfel'd, and V. A. Yamnitskii, Vopr. At. Nauki Tekh. Ser. Fiz. Éksperiment, No. 1(15), 39-43 (1980).
6. V. V. Gann, N. L. Emets, V. A. Kuz'menko, et al., Vopr. At. Nauki Tekh. Ser. Fiz. Radiats. Povrezhdenii Radiats. Materialoved., No. 2(16), 14-18 (1981).
7. Ch. V. Kopetskii, Structure and Properties of Refractory Metals [in Russian], Metallurgiya, Moscow (1974), pp. 117-133.
8. Sh. Sh. Ibragimov, in: Radiation Defects in Metallic Crystals [in Russian], Nauka Alma-Ata (1978), pp. 3-30.
9. N. L. Larikov, in: Radiation Defects in Metals [in Russian], Nauka, Alma-Ata (1981), pp. 87-100.
10. M. B. Waldron, J. Adam, and B. L. Eyre, in: Refractory Metallic Materials for Space Technology [Russian translation], Mir, Moscow (1966), pp. 391-416.
11. Sh. Sh. Ibragimov, O. P. Maksimkin, V. S. Dobrovol'skii, and S. Yu. Chelnokov, in: Radiation Defects in Metals [in Russian], Nauka, Alma-Ata (1981), pp. 189-194.

MODEL OF FISSION-PRODUCT DIFFUSION IN THE CORES OF FUEL MICROASSEMBLIES

V. I. Arkhipov, A. N. Gudkov,
V. A. Kashparov, V. M. Kolobashkin,*
M. A. Koptev, A. A. Kotlyarov,
V. M. Login, and A. I. Rudenko

UDC 621.039.544.55

Questions of gas liberation from fuel materials occupy an important place among the most important problems of high-temperature nuclear power. Hence there arises the need for careful study of the mechanisms of fission-product transfer both in nuclear fuel and in its protective coatings.

Some results of investigating the process of nuclide transfer from a number of fission products in the spherical cores of fuel microelements in the case of multiple capture by traps are given below. A loop experiment on special equipment was performed [1].

The fission products formed in the fuel microelement diffuse under the influence of the concentration gradient arising in connection with the continuous removal of nuclides from the surface of the fuel microelement in conditions of intensive gas flow. The nuclides diffusing in the volume of the microelement may be captured by traps, passing to localized states of different energies, generally speaking. To explain the experimental results, both diffusional [2] and defect-trap models [3, 4] of nuclide transfer have been used; the latter provide better agreement with the experimental data [4].

However, to date, it has been assumed in using the defect-trap model that all the traps are characterized by the same energy level. At the same time, the introduction of the concept of traps with a broad energy-level spectrum allows the experimental dependences to be described in more detail.

*Deceased.

Translated from Atomnaya Energiya, Vol. 59, No. 5, pp. 348-350, November, 1985. Original article submitted October 30, 1984; revision submitted March 25, 1985.

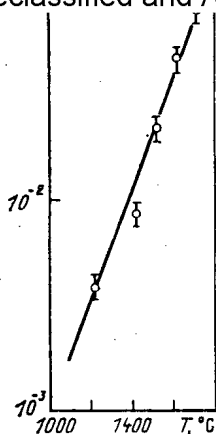


Fig. 1

Fig. 1. Yield of ^{88}Kr nuclides from a 0.26 mm core according to temperature under stationary conditions: The curve is the theoretical dependence according to (4), while the circles are the experimental results.

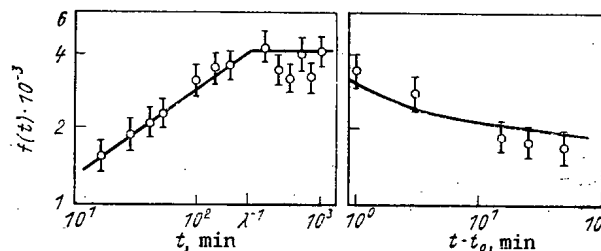


Fig. 2

Fig. 2. Variation over time of the yield of ^{88}Kr nuclides from a 0.26 mm core at 1260°C: Curves) theoretical dependence according to (6), (4) and (7); circles) experimental data.

The energy distribution of localized states is described by the function $n(\mathcal{E})$, where \mathcal{E} is the energy of the localized state measured downward from the minimum energy level of the noncaptured nuclide. A nuclide captured by a trap is in a localized state, but as a result of thermal excitation may leave the trap; the probability of this process is proportional to the Boltzmann exponent $\exp(-\mathcal{E}/kT)$, where T is the temperature. In addition, account must be taken of the probability of nuclide decay determined by its lifetime $(1/\lambda)$.

The basic equations take the form

$$(\partial/\partial t) p(r, t) - D_c (1/r^2) (\partial/\partial r) [r^2 (\partial/\partial r) p_c(r, t)] = G - \lambda p(r, t); \quad (1)$$

$$(\partial/\partial t) \rho(r, t, \mathcal{E}) = (1/\tau_0) [n(\mathcal{E})/N_t] p_c(r, t) - \lambda \rho(r, t, \mathcal{E}) - (1/\tau_0) (N_c/N_t) \exp(-\mathcal{E}/kT) \rho(r, t, \mathcal{E}) \quad (2)$$

$$p(r, t) = p_c(r, t) + \int_0^\infty d\mathcal{E} \rho(r, t, \mathcal{E}), \quad (3)$$

where r is the spherical coordinate, $0 \leq r \leq R$; R , core radius; t , time; $p_c(r, t)$, concentration of mobile nuclides; $\rho(r, t, \mathcal{E})$, concentration of localized nuclides in states with energy from \mathcal{E} to $\mathcal{E} + d\mathcal{E}$; $p(r, t)$ is the overall nuclide concentration G , number of nuclides "generated" in unit volume per unit time; D_c , diffusion coefficient of uncaptured nuclides; $N_t = \int_0^\infty d\mathcal{E} n(\mathcal{E})$ total density of localized states; N_c , density of delocalized states; τ_0 , nuclide lifetime in the noncaptured state.

Equation (1) describes the diffusion with spherical geometry; Equation (2) defines the kinetics of capture and liberation of the nuclides; Equation (3) gives the relation between the concentrations of free and localized nuclides. In deriving Eq. (2), it is assumed that the probability of nuclide capture does not depend on the energy of the localized state and is proportional to the spectral density of capture centers.

The boundary condition corresponds to removal of all the nuclides diffusing to the microelement surface by the heat-carrier flow; $p_c(r = R, t) = 0$. The initial conditions are obtained for irradiation of the microelement by a neutron flux beginning at time $t = 0$: $p(r, 0) = p_c(r, 0) = 0$; $\rho(r, 0, \mathcal{E}) = 0$.

The basic quantity measured in the course of the experiment is the yield function $f(t)$, defined as the ratio of the number of nuclides liberated over the whole core surface per unit time to the number of nuclides generated in the same time over the whole sample volume: $f(t) = -3(D_c/RG)(\partial/\partial r) p_c(r, t)|_{r=R}$.

In the present work, the diffusion of nuclides is considered in the case of an exponential energy distribution of the traps with characteristic energy \mathcal{E}_0 : $n(\mathcal{E}) = (N_t/\mathcal{E}_0) \exp(-\mathcal{E}/\mathcal{E}_0)$.

Solving the steady problem of nuclide diffusion in the core gives the following dependence of the yield function on the basic parameters

$$f_{st} = 3(D_c \tau_0 / R^2)^{1/2} (N_c / N_t \lambda \tau_0^{\alpha/2}), \quad (4)$$

where $\alpha = kT/\mathcal{E}_0$. In the case of the stepwise action of irradiation and generation of nuclides, it is found that

$$f(t) = 3(D_c \tau_0 / R^2)^{1/2} \{ [N_c / N_t \lambda \tau_0] [1 - \exp(-\lambda t)] + \exp(-\lambda t) \}^{\alpha/2} \quad (5)$$

which gives the following result at small times ($t \ll \lambda^{-1}$)

$$f(t) = 3(D_c \tau_0 / R^2)^{1/2} (N_c / N_t)^{\alpha/2} (t / \tau_0)^{\alpha/2} \quad (6)$$

In deriving Eq. (6), it is assumed that $t \gg \tau_0$. Taking into account that τ_0 is very small in comparison with the length of the experiment, this constraint is not too serious. It is appropriate to note here that the inequality $\lambda \tau_0 \ll 1$ is also satisfied. It is evident from Eqs. (5) and (6) that the characteristic time for establishing the steady value f_{st} is $1/\lambda$.

The variation in yield function $f(t)$ in the vase where neutron irradiation ceases at $t = t_0$ after the establishment of a steady state is described by the equations

$$\begin{aligned} f(t) &= \alpha f_{st} \{1 - [\lambda(t - t_0)]^{\alpha/2}\}, \\ \tau_0 &\leq t - t_0 \leq 1/\lambda; \\ f(t) &= (\alpha/2) f_{st} [\lambda(t - t_0)]^{-1+(\alpha/2)} \exp[-\lambda(t - t_0)], \\ t &> 1/\lambda. \end{aligned} \quad (7)$$

The basic results may be compared with experimental data for uranium-dioxide (density 10.2 g/cm^3) cores of radius $R = 0.26 \text{ mm}$. Comparison of analytical Eq. (4) for the steady value of the yield function with the experimental dependence of f_{st} on the temperature (Fig. 1) shows that the diffusional path length of ^{88}Kr in the free state is sufficiently close to the interatomic distance.

Theoretical and experimental curves of the variation in yield function at the beginning and termination of the neutron flux are shown in Fig. 2. Their comparison gives a value of the characteristic energy of the trap distribution $\mathcal{E}_0 = 0.17 \text{ eV}$.

Thus, within the framework of the defect-trap model with energy-distributed traps, the experimental dependences may be well described and some important structural parameters of the core material are obtained from a comparison of the theoretical results and experimental curves.

LITERATURE CITED

1. A. N. Gudkov, V. M. Kolobashkin, M. A. Koptev, et al., "Isothermal loop tests of HTGR fuel microelements," *Vopr. At. Nauk. Tekh., Ser. At.-Vodorod. Énerg.*, No. 1(4), 149-152 (1978).
2. B. Lastman, *Radiation Phenomena in Uranium Dioxide* [in Russian], Atomizdat, Moscow (1964), p. 66.
3. R. Carroll, R. Perez, and O. Sisman, *J. Am. Ceram. Soc.*, 48, No. 2, 54 (1965).
4. A. N. Gudkov, V. M. Kolobashkin, M. A. Koptev, et al., "Experimental investigation of the yield mechanisms of gaseous fission products of HTGR fuel microelements," *Vopr. At. Nauk. Tekh., Ser. At.-Vodorod. Énerg. Tekhnol.*, No. 2(7), 52-55 (1980).

CONTRIBUTION OF DISLOCATION CREEP TO THE RADIATIONAL CREEP
OF MATERIALS

V. A. Borodin and A. I. Ryazanov

UDC 539.376

Radiational creep is an acceleration of the deformation of stressed materials in conditions of irradiation and is observed experimentally at temperatures $\leq 500-700^\circ\text{C}$. In the case of irradiation of materials in fast reactors, the rate of radiational creep referred to the external load and the radiation dose is usually $10^{-6}-10^{-5}$ (MPa·disp./atom) $^{-1}$, which is considerably higher than the rate of thermal creep for this temperature. Therefore radiational creep is, like radiational swelling and embrittlement, one of the basic physical phenomena determining the efficiency of constructional materials in fast reactors and materials of the first wall in projected thermonuclear reactors.

The plastic deformation of materials is a result of dislocational motion. Therefore, adequate theoretical description of this phenomenon requires correct consideration of the development of the dislocational structure of irradiated materials as a function of the irradiation conditions. Experiments show that, on the curve of the rate of radiational creep as a function of the radiation dose, three stages may be conventionally distinguished: transient, steady, and accelerated creep. It is established that, immediately after the onset of irradiation, the creep rate of the stressed material increases sharply, and then gradually decreases over a certain period to a practically constant value. The length of this transient stage of radiational creep is a few hundred minutes for irradiation in charged-particle accelerators and hundreds of hours for irradiation in fast reactors, which corresponds to a radiation dose of 0.01-1 disp./atom. Then the creep rate remains constant up to a dose of $\geq 3-40$ disp./atom, and may subsequently increase over time in certain conditions. In turn, microstructural investigations indicate that the structure of the initial materials is characterized by a dislocation density of between 10^7-10^8 cm $^{-2}$ (for well-annealed samples) and 10^{11} cm $^{-2}$ (for cold-deformed materials). Immediately after the onset of irradiation, Frank interstitial dislocation loops are initiated in the material and grow. The growth of these loops and the elimination of some of the linear dislocations leads to the establishment of an approximately constant dislocation density $(1-3) \cdot 10^{10}$ cm $^{-2}$ at a radiation dose of ≤ 20 disp./atom. [1]. Regarding the acceleration of creep at high radiation doses, it may be assumed at present that this stage is associated with the development of pore systems in the material. Comparison of microstructural data with experimental dose dependences of radiational creep leads to the conclusion that theoretical description of the transient stage of radiational creep entails considering the motion of linear dislocations and the growth of dislocational loops, while the description of the steady stage entails considering the development of a network of linear dislocations, and, finally, at the stage of accelerated creep the influence of pores on the dislocation mobility must be taken into account.

The dependence of the type of dislocational structure developing on the load applied is important for an understanding of the mechanisms of dislocation motion in irradiation conditions. In contrast to the case of thermal creep, which is caused to a considerable extent by the conservative motion of dislocations (slip, limited therofluctuational barrier crossing), irradiation produces supersaturation of point defects, which allows the dislocations to move nonconservatively. As a result, the radiational component of the creep will be determined either by creep of the dislocations or slipping limited by creep through the barriers. As shown by experiments, at a stress $\sigma \leq 100-300$ MPa, the rate of creep depends linearly on the stress and the microstructure is characterized by a system of dislocations and dislocational loops, whereas for large stresses, when the dependence of the creep rate on the stress is significantly nonlinear, a cellular structure is more characteristic [2]. These results indicate that, with a comparatively small external stress, the basic mode of dislocational motion, at least in the transient and steady stages, is creep. At large stresses, dislocational slip processes must be taken into account as well as creep, since at these stresses creep of dis-

Translated from *Atomnaya Énergiya*, Vol. 59, No. 5, pp. 350-355, November, 1985. Original article submitted October 30, 1984.

locations through barriers is significantly easier, and the character of the dislocational structure observed in this case has much in common with the structure characteristic for thermal creep, in which slipping of dislocations plays a significant role.

The question of the relation between the contributions of creep and creep-limited slipping of dislocations to the rate of radiational creep at high stresses requires separate investigation. Here consideration is limited to radiational creep due to processes of dislocational creep. Suppose that there are K orientations of linear dislocations in a material; the k -th orientation ($1 \leq k \leq K$) is specified by the Burgers vector b^k of the corresponding dislocation and the unit vector n^k lying in the extra plane of the dislocations perpendicular to the dislocation line. Then the tensor corresponding to the radiational-creep rate $\dot{\epsilon}_{ij}^{(D)}$ ($i, j = 1, 2, 3$) takes the form

$$\dot{\epsilon}_{ij}^{(D)} = \frac{1}{b} \sum_{k=1}^K b_i^k b_j^k V_c^k \rho_D^k + \frac{1}{b} \sum_{k=1}^K b_i^k n_j^k V_g^k \rho_D^k, \quad (1)$$

where b is the value of the Burgers vector; V_c^k and V_g^k are the rates of creep and slipping of the dislocations of type k ; ρ_D^k is the density of type- k dislocations. Thus, the contributions of creep and slipping of dislocations to the radiational creep may be considered independently.

Note that, at the stage of steady creep, when the dislocational structure is a system of practically linear dislocations, the rate of creep coincides with $\dot{\epsilon}_{ij}^{(D)}$. However, in the transient stage, the contribution of dislocational-loop growth must be taken into account as well as linear-dislocation motion. As well as the above-mentioned Frank interstitial loops, small (≤ 1 nm) vacancy loops may be formed in the material as a result of the relaxation of collision cascades. However, the evolution of these loops cannot be considered, since first of all the character of the dose dependence in the transient stage is not greatly dependent on the form of radiation, while at the same time cascade vacancy loops are not formed at any irradiation, and second, even in the case of vacancy-loop formation, their contribution to the deformation observed in the transient stage is $\leq 1\%$ [3]. Suppose that there are M orientations of the dislocational loops of interstitial type in the material and the distribution of loops of type m ($1 \leq m \leq M$) over the radius is specified by the function $f_m(R, t)$, which is normalized to the density of loops of this orientation per unit volume N_m . The contribution of dislocational-loop growth to radiational creep is

$$\dot{\epsilon}_{ij}^{(L)} = \frac{2\pi}{b} \sum_{m=1}^M b_i^m b_j^m \int_0^{R_{\max}} f_m(R, t) R V_L^m dR, \quad (2)$$

where R_{\max} is the greatest radius of the dislocational loops, close to the mean distance between dislocations; $V_L^m = (dR/dt)_m$ is the growth rate of dislocational loops of orientation m . The total rate of radiational creep at the transient stage may be expressed as $\dot{\epsilon}_{ij} = \dot{\epsilon}_{ij}^{(D)} + \dot{\epsilon}_{ij}^{(L)}$.

Consider the transient stage of creep; assume, for simplicity, that the material is in a state of uniaxial loading with a stream σ and that the predominant majority of dislocational loops are generated immediately after the onset of irradiation. The rate of dislocational creep V_c and growth of the dislocational loops V_L is determined by the fluxes of vacancies and interstitial atoms to these structures

$$\begin{aligned} V_c^k &= \frac{1}{b} (J_{DI}^k - J_{DV}^k); \\ V_L^m &= \frac{1}{b} (J_{LI}^m - J_{LV}^m), \end{aligned} \quad (3)$$

where $J_{D\alpha}^k$ is the flux of point defects of type α ($\alpha = I$ for interstitial atoms and $\alpha = V$ for vacancies) to unit length of a linear dislocation of type k ; $J_{L\alpha}^m$ is the flux of point defects of type α to a dislocational loop of radius R with orientation m . These fluxes may be expressed in terms of the point-defect concentrations far from the sinks C_I and C_V

$$\begin{aligned} J_{D\alpha}^k &= Z_\alpha^k D_\alpha (C_\alpha - C_{\alpha 0}^k); \\ J_{L\alpha}^m &= \eta_\alpha^m D_\alpha (C_\alpha - C_{\alpha 0}^m), \end{aligned} \quad (4)$$

Declassified and Approved For Release 2013/02/20 : CIA-RDP10-02196R000300070005-0
 where D_α is the volume-diffusion coefficient of point defects of type α ; $C_{\alpha 0}$ is the equilibrium concentration of point defects close to the sink with orientation k ; Z_α^k and η_α^m are the asymmetry coefficients of absorption (preferences) of point defects of type α by dislocations with orientation k and loops with orientation m , respectively, depending on the geometry and microstructure of the core of the dislocations and the dislocational loops, and also on the features of their interaction with point defects. The point-defect concentration is determined from the balance equation

$$\frac{\partial C_\alpha}{\partial t} = G - \sum_{k=1}^K \rho_D^k J_{D\alpha}^k - 2 \sum_{m=1}^M \pi \int_0^{R_{\max}} R J_{L\alpha}^m(R, t) dR - B C_I C_V, \quad (5)$$

where G is the rate of Frenkel-pair formation; $B \approx D_I/a^2$ is the recombination coefficient of vacancies and interstitial atoms; a is the interatomic distance. Since the equilibrium distribution of point defects is established sufficiently rapidly in comparison with the change in sink power, it may be assumed that $\partial C_\alpha / \partial t = 0$ in the quasi-steady state.

The coefficients Z_α and η_α determining the dependence of the power of the corresponding point-defect sinks on their form and orientation are important for the description of the rate of radiational creep. At present, it has been established that the difference in preferences of the dislocations and dislocational loops is due to the difference in their geometric forms and core microstructures. Thus, in the case of linear dislocations, a point defect incident at the core of the dislocation will diffuse in an accelerating manner along the core and either be absorbed at the dislocational step or else, if there is no nearby step, travels some mean distance λ_α and leaves the core. If the step is positioned at the edge of the extra plane, the dislocations are sufficiently dense ($\lambda_\alpha C_j \gg 1$, where C_j is the step concentration per unit length of dislocation), each point defect of type α after diffusion in the core is absorbed by some step, regardless of the point at which it enters the core. In this case, the dislocation acts as a continuous sink for point defects and

$$Z_\alpha^k \approx 2\pi / \ln(L/R_\alpha^k), \quad (6)$$

where R_α^k is the radius of elastic interaction of the point defects with dislocations, depending on the orientation of the dislocations because of the polarization of the point defects by the external load; L is the characteristic dimension of the region of influence of the dislocations ($L \sim \rho_D^{-1/2}$, where ρ_D is the total density of linear dislocations). If the step concentration is small ($\lambda_\alpha C_j \ll 1$), the dislocation consists of a discrete set of sinks at the steps with a characteristic region of influence along the dislocations of $\sim 2\lambda_\alpha$. The total length of the sections absorbing point defects of type α per unit length of the dislocation is $\sim \lambda_\alpha C_j$, and the preference Z_α^k may be written in the form [4]

$$Z_\alpha^k = \beta_\alpha^k C_j \lambda_\alpha, \quad (7)$$

where the coefficient β_α^k depends not only on R_α^k but also on C_j ($\beta_\alpha^k \approx 5$). Note that, in the theory of radiational creep, asymmetry of the coefficients β_α plays a fundamental role.

Dislocational loops of size $R \leq 30$ nm include a considerable number of steps on account of their natural curvature and may always be regarded as continuous sinks for point defects. The expression for η_α takes the form in Eq. (6), where the characteristic dimension of the influence region of the dislocational loop $L \sim R$. It is evident that interstitial dislocational loops are stronger sinks for point defects than continuous dislocations ($\eta_\alpha > Z_\alpha$). It may be shown that the relation $\lambda_\alpha > Z_\alpha$ is also valid for "discrete" dislocations if $\lambda_V > \lambda_I$ [5]. As a result, dislocational loops of all orientations will grow on account of their greater absorption of interstitial atoms in comparison with linear dislocations until they become the basic sinks for point defects or part of a dislocational network. In the case when the dislocations are continuous sinks for point defects, the mean radius of dislocational loops is determined by the relation [5]

$$\bar{R} \approx R_c [(1 + 9t/t_c)^{1/3} - 1], \quad (8)$$

where (with the usual experimental parameters) $R_c \approx 1$ -10 nm and $t_c \approx 0.01G^{-1}$. In the case of discrete linear dislocations, the law of increase in \bar{R} is determined from the relation

$$\frac{1}{9} \frac{\bar{R}^3}{R_c^3} \left(1 + \frac{3}{2} \frac{R_c}{\bar{R}}\right) = \frac{t}{t_c}. \quad (9)$$

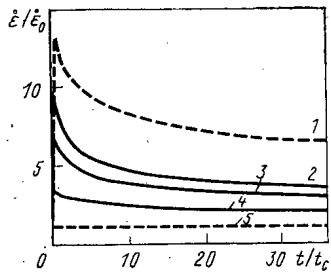


Fig. 1

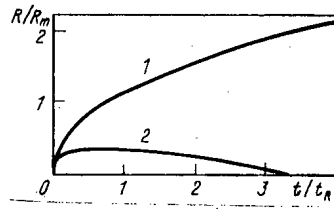


Fig. 2

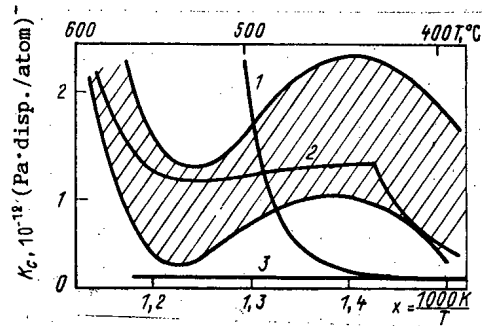


Fig. 3

Fig. 1. Dependence of the rate of radiational creep on the time in the transient stage, for the cases when the dislocations are continuous (dashed curve) and discrete (continuous curve) sinks for point defects: 1) anisotropic orientational distribution of loops; 5) isotropic; 2) $\lambda_I/\lambda_V = 0$; 3) 0.2; 4) 0.5; $\dot{\epsilon}_0 = 10^{-2} G\sigma/\mu$.

Fig. 2. Dependence of the radii of dislocational loops with Burgers vector along (1) and perpendicular (2) to the applied load on the irradiation time; $R_m = 5 \cdot 10^{-3} \rho_D \mu / (N\sigma)$.

Fig. 3. Temperature dependence of the creep modulus $K_c = \dot{\epsilon}/G\sigma$: 1, 2) the dislocations are continuous and discrete sinks for point defects, respectively; 3) the radiational component of the creep rate in the AI model; the shaded region shows the spread of experimental results of the irradiation of steel 316 by fast neutrons in a reactor [9]; $\rho_D = 4 \cdot 10^{10} \text{ cm}^{-2}$; $C_j = \exp(-0.65 \text{ eV}/\tau)$; $(\beta_I - \beta_V)/\beta_I \approx 0.05$; the energy of vacancy formation and migration is 1.7 and 1.2 eV, respectively.

Note that the growth law for interstitial dislocational loops $R \sim t^{1/3}$ was observed in experiments with Nb irradiation in an electron microscope [6].

The development of an ensemble of dislocational loops leads to deformation of the material only in the case when dislocations and dislocational loops with an extra plane perpendicular to the load axis will absorb more interstitial atoms and fewer vacancies than dislocations and loops of other orientations. In other words, determining the rate of radiational creep of a material entails taking account of the stress-induced dependence of Z_α and η_α on the orientation of dislocations and loops and also on the distribution of dislocation densities and loops with respect to the orientation.

In the present work, a model of the orientational dependences of the preferences of discrete linear dislocations in which the influence of the external load on the step concentration at the dislocations is taken into account is proposed. This concentration is maintained constant as a result of dynamic processes occurring in the dislocation cores: steps are continuously generated, shifted along the edge of the extra plane on account of absorption of point defects, and annihilated. It is clear that determining the total step concentration at the dislocations is a kinetic problem in which the influence of point-defect supersaturation of the material must be taken into account. However, regardless of the absolute value of the step concentration, the contribution of the applied load to this concentration may be determined. In fact, new steps are generated by pairs as a result of building up the edge of the extra plane of the dislocations by a complex of Λ atoms or "corrosion" of this edge by a complex of Λ vacancies ($\Lambda \approx 2-3$). Then, the additional work $\delta A = -\Lambda \sigma_{nn}^k \omega$ must be done for the formation of a step nucleus building up the dislocational extra plane under the action of the external load, and work $\delta A = \Lambda \sigma_{nn}^k \omega$ must be performed for a nucleus corroding the extra plane, where σ_{nn}^k is the stress in the direction of the normal to the dislocational extra plane with orientation k ; ω is the atomic volume. Correspondingly, the number of nuclei of particular forms will be proportional to $\exp(-\delta A/T)$, where T is the temperature (in energy units). It may be shown that the development of step nuclei whose further growth leads to acceleration of the deformation is energetically favored. However, if this development is to occur, the growth of an excess number of nuclei must be kinetically possible, i.e., the formation of an excess number of energetically favorable nuclei must not be suppressed by an increase incoming flux of point defects obstructing their growth. If both conditions are observed (the sufficient condition for which is $\lambda_I < \lambda_V$ [4]), the step concentration at dislocations with a Burgers vector directed along the load axis varies so that these dislocations will absorb more interstitial atoms and fewer vacancies than linear dislocations with the same orientation.

As well as influencing the orientational dependence of the preferences, the external stress may cause anisotropic generation of dislocational loops under irradiation. Experimental observations show [7] that such anisotropy may be approximately described by the relation $N_m \sim \exp(n'\sigma_{nn}^m \omega/T)$, where σ_{nn}^m is the deviator component of the load in the direction of the normal to the plane of the loop; $n \approx 3$. It is evident that the largest component of the total number of loops consists of loops with a Burgers vector close to the direction of action of the external load.

In calculating the rate of radiational creep, as well as the proposed mechanism of accelerated step nucleation at discrete dislocations, account must also be taken of the anisotropy produced by the external load in the interaction of point defects with dislocations of various orientations [8] (Fig. 1). Curve 5 corresponds to the case when the dislocations are continuous sources for point defects and the orientational distribution of the dislocational loops is isotropic. Taking account of anisotropy of loop nucleation in the continuous-dislocation model leads to a dependence of the creep rate on the radiation dose (curve 1). Taking account of anisotropy of loop nucleation in the case of discrete dislocations only influences the absolute value of the creep rate, and does not affect the general character of its variation. The character of the variation in creep rate with increase in radiation dose observed in experimental conditions may be qualitatively well described on the basis of the model of dislocations as discrete sinks for point defects (under the condition $\lambda_I < \lambda_V$); see Fig. 1. It is also evident that the continuous-dislocation model gives an increase in creep rate in the transient stage only in the presence of anisotropy of the loops distribution with respect to the direction; the maximum is attained not at once but only after a time $t \approx t_c$. Since $t_c \approx 10$ sec (with irradiation in an accelerator), this difference in character of the curves permits experimental verification of this result. Anisotropy of nucleation of dislocational loops is only significant in the transient stage and will not influence steady creep. The characteristic length of the transient stage $\tau \approx (10-100)t_c$, i.e., $\tau \approx (0.1-1)G^{-1}$. Estimation for conditions of reactor irradiation — $G = 10^{-6}$ (disp./atom)·sec⁻¹ — gives $\tau \approx 10^5 - 10^6$ sec, while for irradiation in charged-particle accelerators — $G = 10^{-5}$ (disp./atom)·sec⁻¹ — $\tau \approx 10^4 - 10^5$ sec, which agrees with the available experimental data.

The given theories allow an interesting effect which may appear at stresses greater than $\sigma^* \approx 0.1 \mu \rho_0^{3/2}/N \approx 5 \cdot 10^{-3} \mu$ to be predicted; here N is the density of dislocational loops per unit volume; ρ_0 is the initial density of linear dislocations; μ is the shear modulus of the material [5]. In this case, "pumping-over" of point defects between dislocational loops resulting from the orientational dependence of η_α may be the basic mechanism of development of a loop system, beginning at some time. In this situation, growth of unfavorably oriented loops stops, and subsequently they dissolve (Fig. 2). As a result, an anisotropic orientational distribution of the orientational loops is formed in the material, consisting mainly of dislocational loops with a Burgers vector that is close to the direction of the loading axis. From estimates, the characteristic time of loop dissolution is $t_R \approx 10^{-9} [\rho_0/(GN)] (\mu/\sigma)^3$. It is evident that for annealed material ($\rho_0 \approx 10^8$ cm⁻²), in conditions of irradiation in an accelerator and an applied high potential — $G = 10^{-3}$ (disp./atom)·sec⁻¹, $\sigma/\mu \approx 5 \cdot 10^{-3}$ — $t_R = 10^4 - 10^5$ sec, i.e., this effect may also be verified experimentally.

The steady stage of radiational creep is most convenient for qualitative comparison with experiment, since in this case the creep rate does not depend on the radiation dose. The dislocational structure of the material in the steady stage consists of a set of linear dislocations with different orientations. Taking account of the discrete structure of the dislocations leads to a value of the creep rate approximately 10-100 times higher than those found on the basis simply of the mechanism of anisotropic interaction of the point defects with dislocations (AI), and this is in considerably better agreement with experiment. If account is taken simultaneously of the influence of the mechanism of accelerated step nucleation, the predicted results are considerably closer to experimental data. Consider, first of all, the dependence of $\dot{\epsilon}$ on the stress. Since the asymmetry of point-defect absorption is caused by external stress σ , expansion of $\dot{\epsilon}$ to terms of first order in σ at small stresses leads to the linear dependence $\dot{\epsilon} \sim \sigma/\sigma_0$ observed experimentally, where σ_0 is some characteristic stress. In the model where anisotropy is due to elastic interaction of point defects with dislocations, it is found that $\sigma_0 \approx \mu$ and hence in this model the creep rate depends linearly on the stress up to values that are close to the shear modulus of the material, which conflicts with experimental observations. Taking accelerated step nucleation into account leads to the appearance of one more characteristic parameter $\sigma_0 \approx T/(\Lambda\omega)$, which gives $\sigma_0 \approx 100-300$ MPa when $T \approx 300-500^\circ\text{C}$, $\omega \approx 3 \cdot 10^{-23}$ cm³, and $\Lambda = 2-3$; this is in reasonable agreement with the existing experimental results for the beginning of the region of nonlinear stress depen-

One advantage of the given model is the possibility of explaining the temperature dependence of the creep rate of irradiated material (Fig. 3). To determine the creep rate in a sufficiently broad temperature range, account must be taken of the contribution of the rate of thermal creep (Nabarro creep) at high temperature and the influence of recombination on the rate of dislocational creep at low temperature ($< 300-400^{\circ}\text{C}$). Recombination must be taken into account here not only in writing the balance equation for the point defects, Eq. (5), but also in determining the flux of point defects to the dislocations in Eq. (4). Of the very small number of careful investigations of the characteristic sigmoid temperature dependence of the creep rate in the region of transition from thermal to radiational creep (Fig. 3), the results are presented in a form convenient for quantitative comparison only in [9], where it was established that the porosity of the given material is slight.

It is evident from Fig. 3 that the radiational-creep modulus of the irradiated material predicted by the AI model (curve 3) lies below the experimental band and, when the thermal component of the creep rate is taken into account in combination with the radiational component, the curve obtained differs greatly from the experimental curve both in general form and in position of the characteristic temperatures corresponding to transition from one section of the curve to another. Since the values of the parameters determining $\dot{\epsilon}$ in the AI model are known sufficiently well, variation in the parameters within reasonable limits cannot significantly improve the agreement between the theoretical and experimental data.

In the case of discrete dislocations with $\lambda_V > \lambda_I$, the form of the curve of $\dot{\epsilon}$ coincides with the experimental curve. At low temperatures, when recombination plays a significant role, the rate of radiational creep increases with increase in temperature. In the temperature range where recombination is insignificant, the model here proposed predicts decrease in the rate of radiational creep with increase in temperature. Finally, at even larger temperatures, the increasing thermal creep begins to play the main role. With a reasonable choice of parameters, good agreement may be achieved between the theoretical and experimental curves, both in order of absolute magnitude and in the position of the extremal points.

As a result, the following conclusions may be stated.

In constructing theoretical models of a radiational creep, for stresses that are not too high ($\geq 100-300$ MPa), it is sufficient to consider only processes of linear-dislocation creep and the growth of Frank dislocational loops, as is confirmed by the results of electron-microscope investigation of the development of the dislocational structure of loaded materials in conditions of irradiation.

In the present work, a new mechanism of radiational creep has been proposed, on the basis that step nucleation at dislocations is promoted by external stress. The use of this model, taking account of the mechanism of stress-induced anisotropy of the elastic interaction between point defects and dislocations, not only permits a correct qualitative explanation of the dependence of the rate of radiational creep on the basic irradiation parameters (dose, stress, temperature) but also allows approximate quantitative agreement with experimental results to be obtained.

At sufficiently high stress, the theory predicts conditions of the formation of an ensemble of dislocational loops with a specific direction of the Burgers vector.

LITERATURE CITED

1. H. Brager et al., in: Radiation Effects in Breeder Reactor Structural Materials (1978), p. 727.
2. E. N. Laguntsev, V. A. Safonov, S. N. Tyumentsev, et al., "Dislocational structure developing in the course of radiational creep," Fiz. Met. Metalloved., 57, No. 4, 802-807 (1984).
3. G. Lewthwaite, J. Nucl. Mater., 61, No. 3, 313 (1976).
4. V. A. Borodin and A. I. Rizanov, Temperature Dependence of the Creep Rate of Irradiated Materials [in Russian], Preprint IAE-3771/11, Institute of Atomic Energy (1983).
5. A. Ryazanov and V. Borodin, Rad. Eff., 59, No. 1, 13 (1981).
6. K. Nakai et al., Philos. Mag. A, 48, No. 2, 215 (1984).
7. H. Brager et al., J. Nucl. Mater., 66, No. 3, 301 (1977).
8. R. Bullough and J. Willis, Philos. Mag., 31, No. 4, 855 (1975).
9. J. Lehmann et al., in: Irradiation Behavior of Metallic Materials for Fast Reactor Core Components (1979), p. 409.

A COMPARATIVE STUDY OF THE CORROSION RESISTANCE OF AN AUSTENITIC STEEL IN LITHIUM AND THE EUTECTIC LEAD-LITHIUM ALLOY

G. M. Gryaznov, V. A. Evtikhin,
L. P. Zavyal'skii, A. Ya. Kosukhin,
I. E. Lyublinskii, N. V. Samsonov,
and A. A. Gusakov

UDC 621.039.6:621.039.53:669.018.8

In a number of designs of thermonuclear reactors (TNR) besides liquid lithium, the use of lead-lithium alloy of the eutectic composition ($Pb_{83}Li_{17}$) is envisaged for tritium breeding, heat transfer, and protecting the primary wall [1, 2]. The interaction of this alloy with water and air is less vigorous as compared to lithium, and the (n, 2n) type reactions involving lead atoms can ensure a tritium-breeding factor exceeding unity (but less than that for lithium) in the TNR blanket at a relatively low concentration of lithium in the alloy.

The previous studies [3] on the corrosion resistance of stainless steels under nonisothermal conditions showed that the mass transfer rate in the lead-lithium alloy is higher than that in lithium; however, in other respects, the nature of corrosive action of these liquid metal systems on the steels is similar.

In view of the limited experimental data available, we carried out tests on the 18-10 steel in convective currents (streams) of lithium and the Pb-17Li alloy in order to compare their corrosive action on the austenitic chromium-nickel steels that are promising materials for the primary wall and the blanket of TNR. Cold-worked (rolled) steel specimens measuring $20 \times 8 \times 1$ mm (their original composition is given in Table 1) were placed in the hot and the cold zones of the loop (Fig. 1) having a temperature of 600 and 500°C, respectively. The loop was made from the 06Kh18N10T steel. The maximum test duration in lithium was 1100 h and in the lead-lithium alloy it amounted to 1000 h; in both cases, the flow rate of the liquid metal was maintained at 2-3 cm/sec and the nitrogen content did not exceed $2 \cdot 10^{-2}\%$. After completing the tests, the specimens were withdrawn from the loop and were cleaned. While the cleaning operation of the specimens and the loop from lithium was easy, it was quite difficult to remove the lead-lithium alloy residue. In view of this, after testing the specimens in the lead-lithium alloy, they were cleaned by additional immersion in lithium at 400°C for a period of 30 min. Following this treatment, these specimens as well as the ones tested in lithium were washed in water and ethyl alcohol. Thereafter, we determined the change in the specimen weight, and carried out metallographic studies and microhardness measurements at a load of 0.49 N. The quantitative evaluation of the local chemical composition of the surface and the distribution of the elements across the cross section of the specimens was carried out using x-ray microspectral analysis under an accelerating voltage of 20 kV and at a probe diameter of $\sim 1 \mu m$. The secondary and absorbed electron images of the surfaces under study were obtained. The distribution of lithium in the steel was evaluated using track autoradiography. The studies were carried out on the low-angle ($2-4^\circ$) sections of the specimens that were not subjected to additional treatment after with-

TABLE 1. Chemical Composition of the 06Kh18N10T Steel

Medium	Weight content of the elements, %				
	C	Mn	Cr	Ni	Ti
Lithium	0,039	1,6	16,5	9,3	0,35
Lead-lithium	0,043	1,6	16,7	9,8	0,37

Translated from Atomnaya Énergiya, Vol. 59, No. 5, pp. 355-358, November, 1985. Original article submitted January 15, 1985.

TABLE 2. Chemical Composition of the Surface of the Steel Specimens Tested under Different Conditions

Medium	Temp. °C	Time, h	Weight content of the elements, %				
			Cr	Ni	Ti	Mn	Si
Lithium	600	1100	7,9	1,9	—	0,14	< 0,05
		560	4,9	4,0	0,3	0,09	< 0,05
	500	1100	69,3	4,2	—	1,1	< 0,05
		560	57,2	3,5	0,9	0,9	< 0,05
Lead-lithium	600	1000	3,4	2,5	1,5	0,05	1,9
	500		29,2	1,7	0,6	0,2	< 0,05

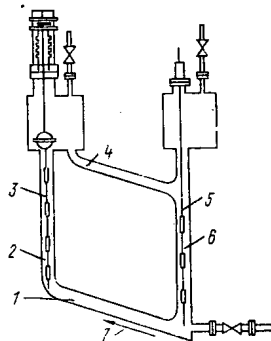


Fig. 1

Fig. 1. Convectional loop: 1) heating zone; 2) hot zone; 3, 5) cassette with specimens; 4) cooling zone; 6) cold zone; 7) flow direction of the liquid metal.

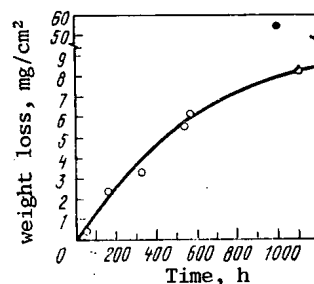


Fig. 2

Fig. 2. Kinetics of the change in the weight of the 06Kh18N10T steel specimens in lithium (○) and in lead-lithium alloy (●).

drawal from the loop. We recorded the products of the reaction ${}^6\text{Li}(n, \alpha){}^3\text{H}$, involving thermal neutrons. The specimens maintained in contact with α solid-state detector were irradiated in an IRT-2000 reactor. The tracks formed in the detector were etched with a 35% aqueous solution of KOH.

Figure 2 shows the kinetics of variation of the specimen weight. Within a period of 10^3 h, the weight loss of the steel specimen in the lead-lithium alloy was found to be 6.5 times greater than that of the specimen tested in lithium and $\sim 10\%$ less than that obtained in the case of the chromium-nickel steels of similar composition in pure lead under similar conditions [4].

The mass transfer rate is, as a rule, proportional to the thermodynamic activity of the most soluble component of a solid alloy in the liquid metal [5]. In the present case, the weight loss increases because of the greater degree of solubility of the components of the steel in lead as compared to that in lithium. At 600°C , the solubility of iron in pure lithium amounts to $\sim 10^{-8}\%$ (atomic fraction $10^{-9}\%$) [6], and in lead it varies from 10^{-3} up to $10^{-2}\%$ (atomic fraction $4 \cdot 10^{-2}$ – $4 \cdot 10^{-1}\%$) [7, 8]. At the same temperature, the solubility of nickel in lithium and lead amount to 0.22% (atomic fraction 0.03%) [6] and 0.5% (atomic fraction 1.8%) [7], respectively. Such a significant relative increase in the solubility of iron and nickel observed when changing the medium from lithium to lead results in only a six-fold increase in the weight loss of the steel. This indicates that the corrosion mechanisms of lithium and lead on the experimental steel must be different.

On the surface of the specimens that were tested at 600°C in lithium and lead-lithium alloy, we observed $\sim 35\text{-}\mu\text{m}$ -thick layers having a different structure and high porosity. In contrast to the specimens drawn from the cold zone, these specimens showed high etchability throughout their depth. The results of chemical analysis of the surface of the steel speci-

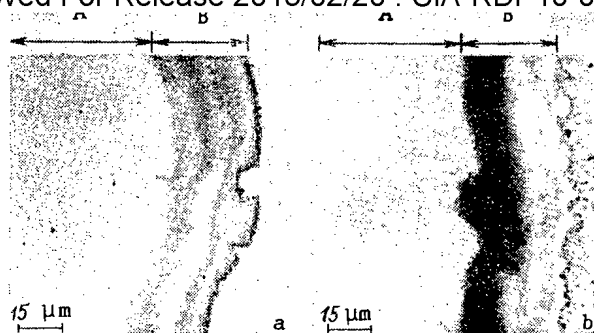


Fig. 3. Track autoradiographs of lithium distribution in the transverse sections of the 06Kh18N10T steel specimens held at 600°C in flowing lithium for a period of 1100 h (a) and in flowing lead-lithium alloy for a period 1000 h (b): A) noncorroded metal; B) corroded zone.

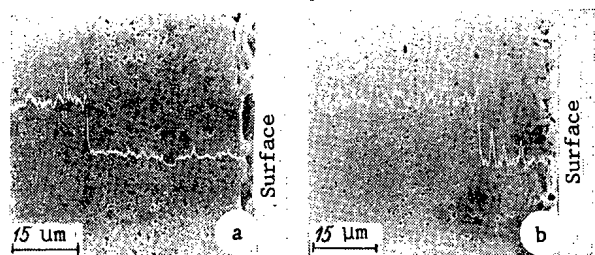


Fig. 4. Surface of the transverse sections of the 06Kh18N10T steel specimens subjected to mild electrolytic etching in a 5% aqueous solution of H_2SO_4 . Secondary electron image with superimposed concentration profiles of nickel distribution: a) immersion in lithium, 1100 h, 600°C; b) immersion in lead-lithium alloy, 1000 h, 600°C.

mens subjected to the action of liquid metal environments (Table 2) indicate that the nature of transfer of the components of the steel is identical in both the cases. In the hot zone there is depletion of nickel and chromium from the surface and in the cold zone there is chromium enrichment of the surface. The observed differences are of secondary nature. Carbon analysis showed that in the specimens held at 600°C in lithium and in the lead-lithium alloy its concentration increased up to 0.061 and 0.054%, respectively; and at 500°C there was a reduction in the carbon concentration up to 0.033 and 0.034%, respectively. It is seen from the track autoradiographs (Fig. 3) that lithium penetrates into the steel up to a depth corresponding to the thickness of the corroded zone. From the lead base alloy, a greater quantity of lithium penetrates into the steel than from pure lithium, and is concentrated in the subsurface layer. Lithium penetration is absent in the steel specimens taken from the cold zone.

The distribution of nickel across the cross section of the specimens (Fig. 4) indicates that the nature of variation of its concentration is identical in both cases and confirms that the weight losses of the steels in lithium and in the lead-lithium alloy are due to stripping of the most dissolvable component (nickel) from them. At the same time, we observed significant differences. It was found that as a result of washing the specimens in lithium, the thickness of the corrosion zone of the specimens (that was previously varied metallographically) reduced to approximately half (see Fig. 4). In order to understand the reasons for this phenomenon, we studied the surface structure of specimens. The shape of the deposited corrosion products in the cold zone of the lithium and the lead-lithium loops does not show significant differences. The corrosion products deposited from the lead-lithium alloy are found to be coarser than those deposited from lithium (Fig. 5). In the hot zone of the lithium loop, the surface of the steel specimens shows a dense cellular structure (Fig. 6) with a cell size of 2-3 μm . The formation of a surface with similar structure was previously observed during a study on the interaction of the 304 and 316 steels

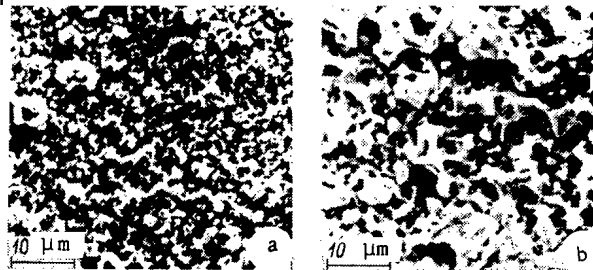


Fig. 5. Surface of the 06Kh18N10T steel specimens held in the cold zone (500°C) of the convectional loop in lithium (a) for a period of 1100 h and in lead-lithium alloy (b) for a period of 1000 h. Secondary electron image.

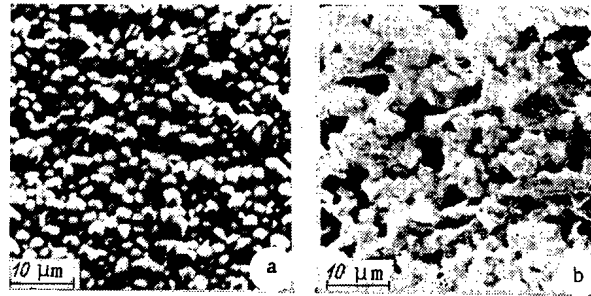


Fig. 6. Surface of the 06Kh18N10T steel specimens held in the hot zone (600°C) of the convectional loop in lithium (a) for a period of 1100 h and in the lead-lithium alloy (b) for a period of 1000 h. Secondary electron image.

with lithium [9]. Under the action of the lead-lithium, the surface structure becomes loose and shapeless. Microhardness measurements on the cross section showed that the deformation resistance of the corrosion zone of the specimens held in lithium is almost the same as that of the metal not in contact with lithium. At the same time, the corrosion layer of the specimens subjected to the environment of the lead-lithium alloy has a microhardness of 0.9 GPa whereas, the microhardness of the central part of the specimen is 1.8 GPa. Thus, under the action of the lead base alloy, a loose and weak ferrite layer forms on the surface of the experimental steel, and this layer is destroyed to a considerable depth during the process of cleaning the specimens in lithium. This agrees with the results of the earlier investigations [3].

Based on the obtained results, the high corrosive activity of the lead-lithium alloy as compared to pure lithium can be explained in the following way. The increased solubility of iron in lead as compared to that in lithium alone can not ensure the observed rate of mass transfer of the steel by the lead base alloy. However, this small increase is found to be sufficient for creating a loose structure and discontinuities in the ferrite layer formed on the surface of the steel leading to its mechanical destruction. This layer being a relatively effective diffusion barrier for preferentially dissolving nickel (in lithium), loses its protective properties (in the given case, approximately up to a depth of 12 μm) under the action of lead resulting in the accelerated diffusional extraction (withdrawal) process of nickel from the body of the steel specimen into the liquid metal. During prolonged operation of the loop, this finally leads to inadmissibly high weight losses of the chromium-nickel steels in the stream of the eutectic lead-lithium alloy.

LITERATURE CITED

1. D. Smith, "Blanket materials for DT fusion reactors," J. Nucl. Mater., 103-104, No. 1, 19-30 (1981).
2. H. Avci and G. Kulcinski, "The effect of liquid-metal protection schemes in inertial confinement fusion reactors," J. Nucl. Technol., 44, No. 2, 333-345 (1979).

3. O. Chopra and D. Smith, "Corrosion of ferrous alloys in eutectic lead-lithium environment," J. Nucl. Mater., 122-123, No. 3, 1219-1224 (1984).
4. J. Ali-Khan, "Corrosion of steels and refractory metals in liquid lead," in: Proc. Int. Seminar on Material Behavior and Physical Chemistry in Liquid Metal Systems, Karlsruhe (1981), Plenum Press, New York (1982), pp. 243-252.
5. V. A. Ivanov and O. V. Starkov, "Solubility of stainless-steels in lithium current," At. Tekh. Rubezh., No. 10, 9-13 (1979).
6. A. I. Kuzin, I. E. Lyublinskii, and N. M. Beskorovainyi, "Experimental and theoretical determination of the solubility of transition metals in liquid lithium," in: Materials for Nuclear Technology [in Russian], Énergoatomizdat, Moscow (1983), pp. 33-41.
7. B. Fleischer and J. Elliott, "The solubility of iron-nickel alloys in liquid lead: 700°C to 1000°C," in: Proc. NRL 9th Sym. on Physical Chemistry of Metals and Alloys, Part 2F, London (1959), pp. 2-12.
8. J. Ali-Khan, "Solubility of iron in liquid lead," in: Proc. Int. Seminar on Material Behavior and Physical Chemistry in Liquid Metal Systems, Karlsruhe (1981), Plenum Press, New York (1982), pp. 237-242.
9. H. Konvicka and P. Reithmayr, "Characterization of 304-SS and 316-SS exposed to liquid lithium for 10,000 h," J. Nucl. Mater., 103-104, No. 3, 645-650 (1981).

MATERIOLOGICAL ASPECTS RELATED TO THE APPLICATION OF LITHIUM IN THE THERMONUCLEAR REACTOR BLANKETS

G. M. Gryaznov, L. G. Golubchikov,
V. A. Evtikhin, L. P. Zavyal'skii,
A. Ya. Kosukhin, and I. E. Lyublinskii

UDC 621.039.6:621.039.53

In most of the existing designs of thermonuclear reactors (TNR), metallic lithium is incorporated as a material for breeding (reproducing) tritium [1]; this alkali metal can be used as a coolant [1, 2]; and the use of lithium is envisaged in the eutectic melts of the Pb-Li and Pb-Bi-Li alloys [1, 2] and in the Na-Li melt [3].

At the present time, a large body of data has been accumulated on various aspects of the interaction of low-melting metals (lithium, sodium, potassium, cesium, lead, bismuth, etc.) and their alloys with metallic structural materials of different classes, and relatively less data are available on their interaction with ceramic materials. A significant practical experience has been gained on the large-scale use of sodium as a coolant in the fast power reactors. However, a simple extension of this experience to lithium is not possible because its properties considerably differ from those of the other alkali metals. This applies to the corrosion activity as well as the technology of working with lithium. The use of lithium in the TNR blankets is associated with the presence of numerous totally new factors whose effect on the interaction of lithium with the structural materials and the efficiency of the liquid-metal systems has virtually not been a subject of discussion and experimental study.

In view of this, it is considered necessary to carry out a brief analysis of the corrosion aspects of the interaction of lithium with the structural materials, to evaluate the possible effect of the factors arising during the service of TNR, and to examine the ways of improving the reliability of the liquid-metal systems of TNR.

COMPATIBILITY OF STRUCTURAL MATERIALS WITH LIQUID LITHIUM

Among the alkali metals, lithium possesses a better combination of thermophysical properties, but at the same time, it is the most active metal with respect to corrosion. For example, at 600°C the solubility of the main components of steels, viz., iron, chromium, and nickel in pure lithium is greater than that in sodium by 50 times on average [4, 5]. Consequently, the mass transfer rate of the chromium and chromium-nickel stainless steels

Translated from Atomnaya Énergiya, Vol. 59, No. 5, pp. 358-363, November, 1985. Original article submitted January 15, 1985.

by nonisothermal currents (flow) is much higher in lithium than in sodium. When testing chromium-nickel austenitic steels in convectional lithium circuits (flow rate of liquid metal 1-3 cm/sec), it was found that the steady-state mass transfer rate varies from 10 up to 30 mg/(m²·h) at a temperature of 600°C [6]. These data characterize, to a large extent, the situation where lithium is used in the TNR blanket for tritium breeding only and its displacement rate is determined by the predetermined productivity of the tritium extraction process. When the lithium coolant flows at a rate of few meters per second, at a hot-zone temperature of 600°C the mass transfer intensity increases by 3-5 times as compared to the intensity due to thermal convection [6]. Such rates of weight loss of steels are not permissible for ensuring satisfactory service of TNR for a few years. The mass transfer rate increases [7] with increasing nickel content in the steel. However, the data obtained on the steels containing 8-16% nickel contradict [6, 8] these conclusions. It is assumed [9] that the stability of chromium-nickel steels is determined by their phase constitution and that it depends on the content of the main elements (chromium and nickel) as well as the supplementary alloying elements (molybdenum, tungsten, titanium, niobium, etc.). So far, a completely well-founded and generally acknowledged approach has not been worked out for selecting the austenitic steels that are stable against mass transfer by lithium. The mass transfer rate of the chromium stainless steels in lithium is significantly lower than that of the chromium-nickel steels [7] and, consequently, their use is preferred under the conditions of contact with lithium.

The corrosion rate of the steels in lithium is affected by the nonmetallic impurities, nitrogen in the first place, and also, oxygen, carbon, and hydrogen [10, 11]. The negative effect of nitrogen impurity on the corrosion of steels has been unambiguously established for the temperatures exceeding ~600°C; for lower temperatures closely corresponding to the actual conditions of the lithium blankets of TNR made from stainless steel, the available data is contradictory. The data obtained on the effect of nitrogen impurity on the solubility of iron, chromium, and nickel in lithium [10] indicate that at a temperature below 600°C the solubility of these metals is a very slowly varying function of the purity of lithium with respect to nitrogen right up to a nitrogen concentration of 0.5%. The available data on the mass transfer of the 316 steel at 400°C in nitrogen-bearing lithium indicate an increased solubility rate of the steel which contradicts the data on the equilibrium solubility of metals in lithium. On the other hand, Tortorelli and Chopra [6] noted the absence of any effect of the nitrogen contaminant (up to a concentration of 0.05%) on the mass transfer of the same steel in the convectional loop at a temperature of 400-600°C. The effect of the impurities carbon, oxygen, and hydrogen on the corrosive activity of lithium has not been studied in detail; however, it is generally acknowledged that their effect is less significant than that of nitrogen [12].

An analysis of the available experimental data on the mass transfer of steels by lithium and the effect of the purity of the liquid metal on it indicate considerable variations in the quantitative characteristics of this process right up to incompatible (mutually exclusive) experimental observations. This circumstance makes it virtually impossible to predict the development of the mass transfer process of steels over long periods of operation of the lithium systems at a temperature of 400-600°C.

In view of the fact that the effect of nonmetallic impurities on the interaction of lithium with the stainless steel is not completely clear, it is necessary to determine the permissible level of their concentration that ensures the desired service life of the materials (in this case, it is necessary to take into account the possible effect of these impurities on the effectiveness of tritium extraction from lithium). The problem is formulated in this manner because of the difficulties encountered in carrying out such a high degree of decontamination (purification) of lithium as to ensure for certain that it meets all the specifications (in particular, when large quantities of lithium require decontamination). This is related to the higher (as compared to the other alkali metals) solubility of nonmetallic impurities in lithium and their high chemical affinity towards this metal [13].

Besides dissolution and mass transfer, penetration of lithium into the structural materials forms a significant corrosion process. In this regard, lithium is also the most active element among the alkali metals. After holding the austenitic 316 chromium-nickel steel at a temperature of 600°C for a period of a few hundred hours under static conditions, lithium traces have been observed in the steel specimen at a depth exceeding 0.6 mm [14]. Under the conditions stimulating selective dissolution of the components of the steel, Bes-

Declassified and Approved For Release 2013/02/20 : CIA-RDP10-02196R000300070005-0
korovainyi et al. [15] observed intense penetration of lithium along the grain boundaries. In this case, they observed occurrence of the recrystallization processes, redistribution of nonmetallic impurities, and an increased etchability (corrosion) of the steel which are not observed during its thermal aging under the same conditions. The nonmetallic impurities present in the solid as well as the liquid phases aid lithium penetration. For example, the presence of nitrogen leads to lithium penetration in the chromium-nickel steels because of the formation of ternary nitrides Li_3CrN_2 and Li_3FeN_2 in the solid phase [16], and the presence of oxygen in vanadium and niobium leads to lithium penetration because of the formation of nonstoichiometric ternary oxides or lithium oxide [17].

Lithium penetration by itself has a negative effect on the mechanical properties of the structural materials as a result of the weakened intergranular bonds (interaction) and the destabilized structure of the metal. Under the conditions of neutron irradiation in TNR, this effect is naturally intensified because of the accelerated accumulation of helium and tritium in the solid phase which form according to the ${}^6\text{Li} + n \rightarrow {}^4\text{He} + {}^3\text{H}$ type reaction from the penetrating lithium atoms [18].

A study of the effect of lithium on the strength and fatigue properties of the stainless steels showed that the mechanical properties of the materials deteriorate under the action of this liquid metal to a greater extent as compared to sodium. An analysis of the available experimental data led to the conclusion [19] that at the present time, it is not possible to make a well-founded long-term prediction regarding the variation of mechanical properties of the steels of different classes that are in contact with lithium.

While the problems of selecting metallic materials for working in liquid lithium are being gradually solved and there are definite achievements in this field, there have not been systematic experimental investigations on the resistance of ceramic materials to lithium environment. The limited results available are generally negative [20]. The ceramics based on oxides and nitrides of metals undergo either complete destruction in liquid lithium and its vapors or volumetric changes and become electrical conductors. The stability of ceramics depends to a large extent on the purity of lithium with respect to nitrogen and oxygen [21]. In a number of cases it was found that contamination of the liquid metal as well as its excessive purity are undesirable. The selection of ceramics that are resistant to the action of liquid lithium or its vapors is a subject of special investigation.

Based on the available experimental results, the following conclusions can be drawn:

only tentative (rough) values of the maximum temperatures at which the structural materials can be used in contact with lithium are known; according to different evaluations, the maximum temperature for chromium-nickel austenitic steels is 500-600°C, for chromium stainless steels 500-650°C, for nickel base alloys 300-500°C, for titanium alloys ~700°C, for niobium alloys 650-1000°C, for vanadium alloys 650-900°C, and for molybdenum alloys 800-1000°C;

there are no well-founded specifications on the purity of metallic lithium intended for the use in the TNR blanket;

the available experimental data are insufficient for a well-founded prediction of the mass transfer process of the materials in lithium and the variation of the mechanical properties, and for selecting lithium-resistant ceramics.

On the whole, the existing information is insufficient for a well-founded selection of the materials and for predicting their behavior in large-sized lithium systems.

EFFECT OF NEUTRON IRRADIATION ON THE COMPATIBILITY OF LITHIUM WITH STRUCTURAL MATERIALS

In contrast to the fast reactors in which the structural materials are subjected to irradiation with neutrons of an energy >0.1 MeV, in TNR the neutron fluence attains much higher values (up to $n \cdot 10^{23} \text{ cm}^{-2}$) under much more rigid energy spectrum. Such conditions can considerably intensify the interaction processes of the materials with lithium. In view of the fact that there has been no experimental verification of the effect of neutron irradiation on the compatibility of the materials with lithium, we can evaluate only the probable mechanisms of the effect of this factor.

Disintegration of the material of the first wall and the structural elements of the blanket by neutrons is most evident on the surfaces in contact with lithium. According to the existing evaluations [10, 22], at a neutron flux density of $10^{16} \text{ cm}^{-2} \cdot \text{sec}^{-1}$, the disintegration rate of 316 steel can amount to a few tens of microns per year. In view of the fact that the corroded layer forming on steels (as a result of preferential dissolution of their components in lithium) is subjected to disintegration and the diffusional resistance of this layer is low, there is an inevitable increase in the rate of mass transfer by the liquid metal. This leads not only to a reduction in the lithium-resistance (stability) of the steels, but also to an increase in the volume of the corrosion products formed which contaminate the surfaces of tritium extraction from lithium and worsen the radiational conditions.

It is well known that the neutron irradiated austenitic steels are prone to vacancy-related swelling. The volumetric expansion may reach 10% or more. Considering the high penetrating ability of lithium, one can expect that it will rapidly penetrate into the steels along the resulting pores. In the steels, lithium penetration is accelerated also due to the excess-phase precipitation [23] which is intensified under irradiation [24].

Loss of corrosion resistance may also be found in the chromium steels exhibiting a less degree of swelling. It occurs because of the increased defect density during irradiation which, in turn, leads to an increased dissolution rate of the components of these steels and facilitates lithium penetration into the steels.

When evaluating the effect of neutron irradiation on the corrosion of structural materials in lithium, one must also consider the possibility of chemical compositional changes in these materials as a result of transmutation under irradiation. For instance, after two years service under a thermal load of 5 MW/m^2 on the first wall, the atomic fraction of helium and hydrogen formed in the 316 stainless steel amounts to approximately 0.7% [10]. Helium formation increases when high-nickel steels and alloys are used. Irradiating a niobium base alloy with neutrons under a load of 1.25 MW/m^2 for 30 years service of TNR leads to an increase in the atomic fraction of zirconium in the alloy from 1.0 up to 6.5% owing to nuclear transformations. Under similar conditions, the compositions of a 316 steel changes in the following way [25]: atomic fraction of iron — from 62.6 up to 58.0%, nickel — from 14.0 up to 13.3%, manganese — from 2.0 up to 6.4%, and titanium — from 0.01 up to 0.2%. All these changes can significantly affect the interaction of the structural materials with lithium.

It may be assumed that besides the aforementioned possible mechanisms of the effect of irradiation on the corrosion processes, it affects the chemical interaction in the system "liquid lithium-dissolved metal-nonmetallic impurity." A shift (disturbance) of the equilibrium in this system to either side under the action of radiation leads to an increase or decrease of corrosion of the metal in lithium.

All the aforementioned effects related to neutron irradiation must be studied experimentally in order to determine their actual effect on the compatibility of the structural materials of TNR in lithium.

EFFECT OF A STRONG MAGNETIC FIELD ON THE INTERACTION OF THE STRUCTURAL MATERIALS WITH LITHIUM

The presence of a magnetic field is characteristic of the tokamak-reactors only. In such TNR the magnetic field changes rapidly with time and its intensity can reach 5-7 T [26]; such a field is capable of causing significant changes in the rate and even in the nature of the interaction processes of lithium with the structural materials.

According to the existing hypotheses [1], the alternating magnetic field, across which the (electric) current-carrying liquid is moved, facilitates equalization (smoothing out) of the profile of lithium flow rate. This must lead to a reduction in the thickness of the lamellar boundary layer of the liquid stream (flow) which, in turn, changes the nature of the dissolution process of the solid metal in liquid lithium. When this layer is quite thick (characteristic for moderate flow rates), the diffusion of the dissolved metal in liquid lithium is the controlling stage; on the other hand, when the thickness of the lamellar layer is reduced to $\leq 5 \mu\text{m}$ (usually observed at high flow rates), the process of transition of the atoms of the dissolving metal through the solid-liquid interface becomes the controlling stage. Experience shows that such a change leads to a significant increase in

Declassified and Approved For Release 2013/02/20 : CIA-RDP10-02196R000300070005-0

the dissolution and mass transfer rates of the structural materials in liquid metals. Thus, the effect of the magnetic field on lithium current is equivalent to increasing its flow rate in the system. The aforementioned effect is a characteristic of the structural materials of any class; other possible mechanisms of the effect of magnetic field apply mainly to the steels of the austenitic class. A significant feature of most of the austenitic steels used in reactor building is that they are metastable at the service temperatures below $0.5 T_{\text{melting}}$. This situation determines the possibility of occurrence of structural and phase transformations in the steels used in TNR. They may occur due to the aforementioned radiation-induced intensified diffusion [24] and due to the action of a magnetic field. It is known [27] that in a magnetic field, the boundaries of the two-phase regions $\alpha/\alpha + \gamma$ and $\gamma/\alpha + \gamma$ are shifted towards higher temperature because of the reduced free energy of the magnetic α -phase. The high diffusion coefficients of the components of the steel in the α -phase (as compared to those in austenite) make the two-phase $\alpha + \gamma$ materials less resistant to lithium as was confirmed by the experiments [9].

As a result of the preferential corrosion of the austenitic steels in lithium, their surface layer undergoes $\gamma \rightarrow \alpha$ transformation and a corresponding transition from the paramagnetic state to the ferromagnetic state. Because of porosity and intense penetration of the liquid metal, the corroded layer becomes loose (friable) and weak as has been observed in the case of the 316 steel held in the lead-lithium eutectic at 470-500°C [28]. Under the action of a magnetic field, the mechanically weak ferromagnetic layer can peel off and expose the uncorroded metal. This process abruptly increases the rate of weight loss of the steel and constantly holds it at a high level.

Besides intensifying the corrosion processes, the magnetic field changes the nature of deposition of the corrosion products. Their ferromagnetic constituent (mainly iron) can concentrate not only in the cold zones, but also in other parts of the system. This suggestion is based on the observation indicating that in the lithium circuits the dissolved iron and manganese are concentrated in the working zones of the magnetohydrodynamic pumps and the magnetic flowmeters [6]. Just as in the case of the other phenomena related to the magnetic field, the actual contribution of this phenomenon towards the development of corrosion processes of the structural materials in lithium and its effect on the efficiency of the liquid metal systems of TNR must be evaluated experimentally.

Numerous aspects of materials behavior require investigation in connection with tritium breeding in the lithium blanket, its effective retention in the system, and withdrawal from it. An analysis of the effect of tritium existing in lithium at a concentration level of 10^{-4} - $10^{-3}\%$ on the structural materials shows [29] that this factor does not significantly change the mechanical properties of steels and refractory metals. Most of the problems of materials science that emerge due to the presence of tritium are related to the method of tritium extraction from lithium and, consequently, the discussion and analysis of these aspects form a subject of special investigation.

It follows from the aforementioned facts that under the operation conditions of TNR, the effect of lithium on the structural materials (that is significant by itself) can be substantially intensified under the action of neutron irradiation and a strong magnetic field. The results of the materials and structural studies undertaken for designing TNR must be confirmed by direct experiments that would take into account the complete set of factors affecting the compatibility of the structural materials with lithium.

In spite of the problems remaining unsolved at the present time, on the whole, the investigators are optimistic regarding the possibility of accomplishing TNR designs using liquid lithium and stainless steels as the structural materials in the blanket. Various protection methods are proposed for improving the resistance of the materials to the action of lithium. The most acceptable method among these is to develop the steels with optimum alloying ensuring maximum reduction in the activity of the components of the steels that are easily dissolvable and are prone to transfer by the liquid metal (besides ensuring the required combination of the physical and mechanical properties) [30]. However, the studies conducted in this direction [7, 9, 31] have not yet yielded sufficiently well-founded recommendations.

Creation of protective coatings and diffusion barriers [2] on the surface of the structural materials is a promising direction. For instance, it was shown that addition of 5% aluminum to lithium decreases the mass transfer rate of the 316 steel in lithium stream

(flow) by approximately 5 times owing to the formation of a layer of intermetallic compounds on its surface [32]. We note that alitizing (aluminizing) of steels is also an effective means of decreasing their hydrogen permeability at temperatures up to 700°C [33]. Thus, aluminum addition to lithium could simultaneously increase the corrosion resistance of the steels and decrease the rate of tritium penetration through them. Just as the other methods of protecting the structural materials from corrosion in lithium environment, alitizing through the liquid metal requires additional experimental basis in view of the indications [11] that it does not have a positive effect.

LITERATURE CITED

1. J. DeVan, "Compatibility of structural materials with fusion reactor coolant and breeder fluids," *J. Nucl. Mater.*, 85-86, No. 1, 249-256 (1979).
2. O. Chopra and P. Tortorelli, "Compatibility of materials for use in liquid-metal blankets of fusion reactors," *ibid.*, 122-123, No. 3, 1201-1212 (1984).
3. R. V. Verner, B. Maier, P. B. Mor, et al., "Initial examination of the power reactor based on the 'Astron' system," in: *Selected Reports of the Conference on Thermonuclear Reactors* [in Russian], Issue 4, Atomizdat, Moscow (1974), pp. 3-18.
4. F. A. Kozlov, Yu. N. Zagorul'ko, N. G. Bogdanovich, et al., *Solubility of Individual Substances in Sodium* [in Russian], Preprint FÉI-510, Obninsk (1974).
5. A. N. Kuzin, I. E. Lyublinskii, and N. M. Beskorovainyi, "Experimental and theoretical determination of the solubility of transition metals in liquid lithium," in: *Materials for Nuclear Technology* [in Russian], Énergoatomizdat, Moscow (1983), pp. 33-41.
6. P. Tortorelli and O. Chopra, "Corrosion and compatibility considerations of liquid metals for fusion reactor applications," *J. Nucl. Mater.*, 103-104, No. 2, 621-632 (1981).
7. P. Tortorelli and J. DeVan, "Effect of nickel concentration on the mass transfer of Fe-Ni-Cr alloys in lithium," *ibid.*, 103-104, No. 2, 633-638 (1981).
8. G. Whitlow, W. Wilson, W. Ray, and M. Down, "Materials behavior in lithium systems for fusion reactor applications," *ibid.*, 85-86, No. 1, 283-387 (1979).
9. I. E. Lyublinskii, A. N. Kuzin, and N. M. Beskorovainyi, "Regularities in the effect of alloying of chromium and chromium-nickel steels on their stability in liquid-metal coolants," in: *Materials for Nuclear Technology* [in Russian], Énergoatomizdat, Moscow (1983), pp. 41-52.
10. N. M. Beskorovainyi and A. G. Ioltukhovskii, *Structural Materials and Liquid-Metal Coolants* [in Russian], Énergoatomizdat, Moscow (1983).
11. V. Coen, H. Kolbe, L. Orecchia, and T. Sasaki, "Compatibility of high Ni-Fe-Cr alloys in lithium containing traces of LiH," in: *Proc. Int. Seminar on Material Behavior and Physical Chemistry in Liquid-Metal Systems*, Karlsruhe (1981), Plenum Press, New York (1982), pp. 121-130.
12. N. M. Beskorovainyi, A. A. Rusakov, and I. E. Lyublinskii, "Structural materials (interaction with liquid metals)," in: *Itogi Nauki i Tekhniki. Ser. Metallovedenie i Termicheskaya Obrabotka* (Physical Metallurgy and Heat Treatment), Vol. 11, VINITI, Moscow (1977), pp. 112-151.
13. V. I. Subbotin, M. N. Ivanovskii, and M. N. Arnol'dov, *Physicochemical Principles of Using Liquid-Metal Coolants* [in Russian], Atomizdat, Moscow (1970).
14. M. Barker and S. Frankham, "The effects of carbon and nitrogen on the corrosion resistance of type 316 stainless steel to liquid lithium," *J. Nucl. Mater.*, 107, No. 1, 218-221 (1982).
15. N. M. Beskorovainyi, A. G. Ioltukhovskii, E. I. Filippkina, et al., "A study on the interaction of a chromium-nickel steel with sodium, lithium, and sodium containing 1% lithium at 650°C," in: *Materials for Nuclear Technology* [in Russian], Énergoatomizdat, Moscow (1983), pp. 23-32.
16. P. Bull, H. Tas, R. Toels, et al., "Chemical aspects of fusion technology - 1982," *Nucl. Fusion*, 23, No. 7, 955-973 (1983).
17. A. G. Arakelov, L. N. Galkin, V. V. Vavilova, and A. F. Gekov, "Corrosion of vanadium alloys in lithium," *Zashch. Met.*, 17, No. 2, 233-236 (1981).
18. J. Megusar, O. Harling, and N. Grant, "Lithium doping of candidate fusion reactor alloys to simulate simultaneous helium and damage production," *J. Nucl. Mater.*, 115, No. 1, 192-196 (1983).
19. O. Chopra, "Effects of sodium and lithium environments on the mechanical properties of ferrous alloys," *Ibid.*, 115, No. 1, 223-238 (1983).

20. J. Schreinlechner and F. Holub, "Compatibility of certain ceramics with liquid lithium," in: Proc. Int. Seminar on Material Behavior and Physical Chemistry in Liquid-Metal Systems, Karlsruhe (1981), Plenum Press, New York (1982), pp. 105-111.
21. M. Barker, J. Alexander, and J. Bentham, "The reactions of liquid lithium with the dioxides of titanium, zirconium, hafnium, and thorium," J. Less-Common Met., 42, No. 1, 241-247 (1975).
22. A. Johnson and W. Vogelsang, "An assessment of corrosion product transport problems in a CTR," Trans. Am. Nucl. Soc., 17, 150-151 (1973).
23. E. Ruedl and T. Sasaki, "Effects of lithium on grain-boundary precipitation in a Cr-Mn austenitic steel," J. Nucl. Mater., 116, No. 1, 112-122 (1983).
24. L. N. Bystrov, L. I. Ivanov, Yu. M. Platov, and V. M. Ustinovshchikov, "Radiation-induced structural and phase transformations in the materials of the first wall of the thermonuclear reactors," in: Structural Materials for the Thermonuclear Fusion Reactors [in Russian], Nauka, Moscow (1983), pp. 5-18.
25. W. Vogelsang, G. Kulcinski, R. Lott, and T. Sung, "Transmutations, radioactivity, and afterheat in a deuterium-tritium tokamak fusion reactor," J. Nucl. Technol., 22, No. 2, 379-391 (1974).
26. M. Hegler and M. Christiansen, Introduction to Controlled Thermonuclear Fusion [Russian translation], Mir, Moscow (1980).
27. D. Martin and R. Roétti, Microstructural Stability of Metallic Systems [in Russian], Atomizdat, Moscow (1978),
28. O. Chopra and D. Smith, "Corrosion of ferrous alloys in eutectic lead-lithium environment," J. Nucl. Mater., 122-123, No. 3, 1219-1224 (1984).
29. K. Natesan, "Influence of nonmetallic elements on the compatibility of structural materials with liquid alkali metals," *ibid.*, 115, No. 1, 251-262 (1983).
30. B. A. Nevzorov, V. V. Zotov, V. A. Ivanov, et al., Corrosion of Structural Materials in Liquid Alkali Metals [in Russian], Atomizdat, Moscow (1977).
31. P. Tortorelli and J. DeVan, "Mass transfer behavior of a modified austenitic stainless steel in lithium," J. Nucl. Mater., 122-123, No. 3, 1258-1263 (1984).
32. G. Burrow M. Down, and Bagnall, "Corrosion inhibition experiments in liquid lithium," *ibid.*, 103-104, No. 3, 657-662 (1981).
33. D. M. Skorov, B. A. Kalin, E. P. Fomina, et al., "Studies on a fragment of a converted blanket," in: Proc. II All-Union Conference on Engineering Problems of Thermonuclear Reactors [in Russian], Vol. 4, NIIÉFA, Leningrad (1982), pp. 346-351.

THERMODYNAMICS OF THE INTERACTION OF UO_2 WITH CARBON IN THE PRESENCE
OF THE ADDITIVES $\text{Al}_2\text{O}_3 \cdot \text{SiO}_2$, SiC , AND UC_2

Yu. F. Khromov, D. E. Svistunov,
and S. A. Zhmurov

UDC 621.039.542.34

In a study on the thermodynamics of the interaction of uranium oxide with carbon [1], we measured the equilibrium pressure of CO for the $\text{UO}_2 + \text{C}$ system in the presence of excess carbon and analyzed the variations of the oxygen potential in the homogeneity region of UO_{2+x} .

In continuation of these studies, we investigated the thermodynamics of the interaction of UO_2 with C in the presence of the additives, viz., aluminosilicate $\text{Al}_2\text{O}_3 \cdot \text{SiO}_2$, silicon carbide, and uranium dicarbide. The studies were carried out according to the Knudsen method described elsewhere [1-3]. In the experiments, we measured the pressure of carbon monoxide as a function of the temperature and the composition of the systems under study. After prior high-vacuum degassing (degasification), we studied the systems (compositions) based on uranium oxide in contact with pyrocarbon in the temperature range 1300-1900°K (Table 1). The systems $\text{UO}_2 + \text{UC}_2$ and $\text{UO}_2 + \text{SiC}$ were produced by mixing the powders of the respective compounds in a neutral organic matter. The systems consisting of uranium dioxide with the additions of aluminum and silicon oxide, and the oxides Al_2O_3 , SiO_2 , and

Translated from Atomnaya Énergiya, Vol. 59, No. 5, pp. 363-366, November, 1985. Original article submitted July 13, 1984.

TABLE 1. Characteristics of the Components and the Experimental Systems in Contact with Carbon

Composition	Weight content of elements, %					Mole ratio $\text{Al}_2\text{O}_3/\text{SiO}_2$; UO_2/UC_2 ; UO_2/SiC	Lattice parameter, nm	
	U	Al	Si	C_{tot}	O_2^*		before expt.	after expt.
UO_2	87,2	—	—	—	12,8	—	0,54640	0,54710
$\text{UO}_2 + 6,5 \text{ wt. \% } (\text{Al}_2\text{O}_3 \cdot \text{SiO}_2)$	82	2,4	0,5	—	5,1	2,5/1	0,54610	0,54702
$\text{UO}_2 + 5 \text{ wt. \% } (\text{Al}_2\text{O}_3 \cdot \text{SiO}_2)$	80,4	0,9	1,6	—	—	1/3,5	0,54640	0,54700
SiO_2 after calcin.	—	—	46,6	—	53,4	—	—	—
Al_2O_3 after calcin.	—	52,9	—	—	47,1	—	—	—
$3\text{Al}_2\text{O}_3 \cdot 2\text{SiO}_2$ (mullite)	—	38	13,10	—	48,9	3/2	—	—
$\text{UO}_2 + \text{UC}_2$	—	—	—	—	—	1/1	—	—
UO_2	87,2	—	—	—	12,8	—	0,54640	0,54702
UC_2	87,7	—	—	8,8	—	—	0,3527	—
$\text{UO}_2 + \text{SiC}$	—	—	—	—	—	1/1	—	—
UO_2	87,2	—	—	—	12,8	—	0,54640	0,54701
SiC	—	—	70	30	—	—	—	—

Note: Weight content of other impurities amounts to <0.1% in each system. The O/U ratio in the original uranium dioxide is equal to 2.04.

*Calculation based on the difference.

TABLE 2. Values of the Constants A and B in the Equation $\log P_{\text{CO}}(\text{Pa}) = A - B(10^4/T)$ Depicting the Temperature Dependence of the Pressure of CO in the $\text{M}_x\text{O}_y + \text{C}$ Systems

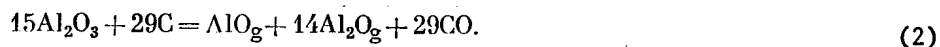
Calculated phase composition	Temp. range, °K	A	B
UO_2 , original (Fig. 1, curve 4; Fig. 4, curve 2)	—	14,732	1,998
Al, C, UO_3 , $3\text{Al}_2\text{O}_3 \cdot 2\text{SiO}_2$, Al_2O_3 (Fig. 1, curve 1)	1200—1450	13,665	2,20
Al_2O_3 (after calcin.), Al, C (Fig. 1, curve 3)	1200—1450	15,515	2,16
Al_2O_3 (after calcin.), C (Fig. 1, curve 5)	900—1100	14,285	1,30
$3\text{Al}_2\text{O}_3 \cdot 2\text{SiO}_2$, SiO_2 , SiC, C (Fig. 2, curve 3)	1300—1500	16,9925	2,40
UO_2 , $3\text{Al}_2\text{O}_3 \cdot 2\text{SiO}_2$, SiO_2 , SiC, C (Fig. 3, curve 1)	900—1200	9,805	0,80
SiO_2 (after calcin.), SiC, C (Fig. 3, curve 2)	850—1100	10,185	0,81
UO_2 , SiC, SiO_2 , C (Fig. 3, curve 3)	850—1100	13,795	1,10
UO_2 , SiO_2 , Si, C (Fig. 3, curve 4)	900—1300	9,715	1,07
UO_2 , UC_2 , C (Fig. 4, curve 1)	1200—1400	14,935	2,00

mullite ($3\text{Al}_2\text{O}_3 \cdot 2\text{SiO}_2$) were obtained by precipitation using aqueous ammonium hydroxide solution with subsequent calcination (roasting) of the hydroxides at 1050–1100°K. Table 2 and Figs. 1–4 show the experimental results in the form of analytical dependences $\log P = f(T)$ which are in satisfactory agreement with the value of the oxygen potential of the compounds under study, viz., UO_{2+x} , SiO_{2-x} , and $3\text{Al}_2\text{O}_3 \cdot 2\text{SiO}_2$.

A direct evaluation of the pressure P_{CO} according to the equation

$$\lg P_{\text{CO}} = \lg K_p + 1/2 \lg P_{\text{O}_2}, \quad (1)$$

where K_p is the oxidation constant of carbon up to CO, is possible only in the case of simple compounds (Fig. 1, curves 2 and 3) which dissociate into the constituent elements and form carbon monoxide CO. An analogous reaction with carbon is observed in the case of uranium dioxide containing aluminosilicate additive that has excess Al_2O_3 with respect to the composition of mullite $3\text{Al}_2\text{O}_3 \cdot 2\text{SiO}_2$ (Fig. 1, curve 1). The temperature of prior degassing of the experimental systems (curves 1, 3, and 4) under a residual pressure of $6.6 \cdot 10^{-5}$ Pa was maintained at 1500–1800°K until the attainment of the equilibrium pressure of CO. In the absence of Al_{sd} in the final products of the reactions of the oxides with carbon after degassing at a residual pressure of $6.6 \cdot 10^{-5}$ Pa in the temperature range 800–900°K, the values of the equilibrium pressure P_{CO} are found to be significantly higher (Fig. 1, curve 5). This agrees with the result of mass spectroscopy [4] (point 7) and the calculated values (curve 6) for the reaction



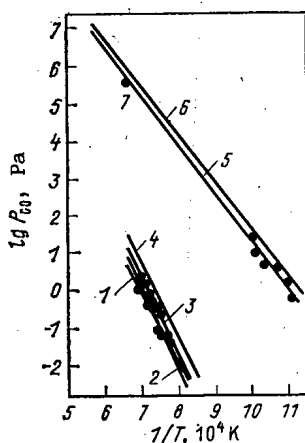


Fig. 1

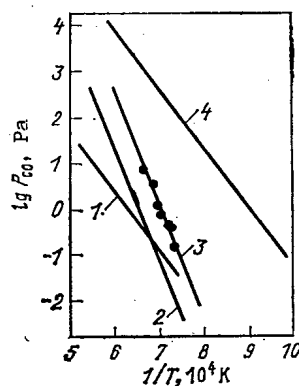


Fig. 2

Fig. 1. Pressure P_{CO} as a function of temperature for the systems with aluminosilicate addition under excess Al_2O_3 : 1) $UO_{2+x} + 3Al_2O_3 \cdot 2SiO_2$ (excess Al_2O_3) + C (experiment); 2) $4Al_2O_3 + 6C = Al_{sd} + Al_2O_g + 5AlO_g + 6CO$ (calculated); 3) $Al_2O_{3-x} + C$ (experiment); 4) $UO_{2ini} + C$ [3] (experiment); 5) $Al_2O_3 + C$ (experiment); 6) $15Al_2O_3 + 29C = 2AlO_g + 14Al_2O_g + 29CO$ (calculated); 7) calculated P_{CO} according to the published data [4] for $Al_2O_3 + C$ (calculated).

Fig. 2. Pressure P_{CO} as a function of temperature for the mullite system ($3Al_2O_3 \cdot 2SiO_2$) with carbon: 1) $3Al_2O_3 \cdot 2SiO_2 + C = 3Al_2O_3 + 2Si_{sd} + 3CO + SiO_g$ (calculated); 2) $3Al_2O_3 \cdot 2SiO_2 + 4C = 3Al_2O_3 + 2Si_{sd} + 4CO$ (calculated); 3) $3Al_2O_{3-x} \cdot 2SiO_{2-x} + C$ (experiment); 4) $3Al_2O_3 \cdot 2SiO_2 + 4C = 3Al_2O_3 + SiO_g + 3CO + SiC$ (calculated).

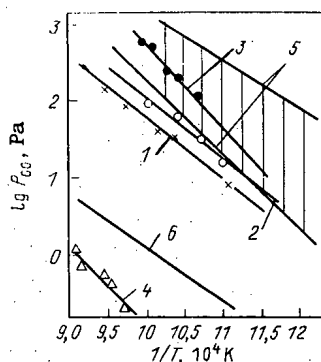


Fig. 3

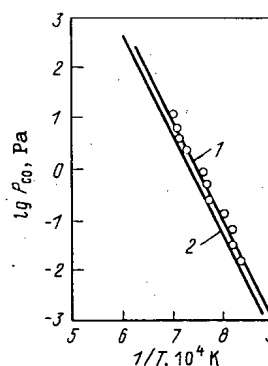


Fig. 4

Fig. 3. Pressure P_{CO} as a function of temperature for the UO_2 systems with aluminosilicate addition under excess SiO_2 : 1) $UO_{2+x} + 3Al_2O_3 \cdot 2SiO_2$ (excess SiO_2) + C (experiment); 2) SiO_2 (calcined) + C (experiment); 3) $UO_{2+x} + SiC + C$ (experiment); 4) $UO_{2+x} + SiO_{2-x} + Si + C$ (experiment); 5) $SiO_2 + 4C = SiO_g + 3CO + SiC$ (calculated); 6) $2SiO_{2-x} + 3C = Si_{sd} + SiO_g + 3CO$ (calculated).

Fig. 4. Pressure P_{CO} as a function of temperature for the $UO_2 + UC_2$ system: 1) $(UO_2 + 50 \text{ mole } \% UC_2) + C$ (experiment); 2) $UO_{2ini} + C$ [1] (experiment).

Such a behavior of aluminum oxide indicates the existence of a narrow range (region) of homogeneity and the change in the nature of the interaction with temperature indicates the absence of congruent evaporation in the region of the Al_2O_3 compositions.

The experimental and the calculated data on the thermodynamics of interaction of $3\text{Al}_2\text{O}_3 \cdot 2\text{SiO}_2$ with carbon show that after degassing in the temperature range 1500-1800°K, there is a high probability of mullite decomposition into the constituent oxides SiO_2 and Al_2O_3 , and after subsequent dissociation of SiO_2 , oxygen interacts with carbon to form CO (Fig. 2, curves 2 and 3). If the degassing temperature of this system is decreased up to 800-900°K, the equilibrium pressure P_{CO} must increase up to the values corresponding to the curve 4.

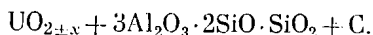
An analysis of the interaction (with carbon) of the uranium dioxide systems containing aluminosilicate additive in which the $\text{SiO}_2/\text{Al}_2\text{O}_3$ ratio is higher than that in mullite indicates the occurrence of the reaction with the formation of CO, silicon monoxide SiO^* , and silicon carbide



This result follows from the fact that the calculated data (Fig. 3, curve 5) coincide with the experimental values obtained for the systems subjected to prior degassing at 900°K and under a residual pressure of $6.6 \cdot 10^{-5}$ Pa (curves 1, 2). When uranium dioxide is alloyed with silicon carbide (curve 3), the pressure of CO is insignificantly higher than that existing over the systems



The aforementioned situation indicates that in the three systems being examined, equilibrium is established according to the reaction (3); here, in the system $\text{UO}_{2+x} + \text{SiC} + \text{C}$, uranium oxide acts as the oxygen source for the formation of CO, and the interaction in this system must be considered as a reverse process with respect to that observed in the system



The observed small difference in the values of $P_{\text{CO}} = f(T)$ over $\text{UO}_{2+x} + \text{SiC} + \text{C}$ as compared to the values found for the other two systems is apparently related to the structural state of the oxide SiO_2 isolated as a result of the reverse (back) reaction and to the dissimilar O/U ratios in the final uranium dioxide and that entering the system $\text{UO}_{2+x} + 3\text{Al}_2\text{O}_3 \cdot 2\text{SiO}_2 + \text{SiO}_2 + \text{C}$.

The calculations showed that the formation of finely dispersed silicon dioxide having the structure of glass can lead to a considerable increase of P_{CO} in the system $\text{SiO}_2 + \text{SiC} + \text{CO} + \text{SiO}_g + \text{C}_{\text{sd}}$ (see Fig. 3, curve 5). A similar nature of the variation of the equilibrium pressure of nitrogen due to the differences in the dispersion of carbon was observed [7] in a study of the direct and reverse reactions



During the interaction of the $\text{UO}_2\text{-SiO}_2$ system with carbon after initial combined degassing at 1800°K and under a residual pressure $\approx 6.6 \cdot 10^{-5}$ Pa, the absence of congruent volatilization in the region of SiO_2 compositions [6] leads to the formation of elemental silicon Si_{cond} and to a reduction in the values of P_{CO} (see Fig. 3, curves 4, 6) similar to the nature of interaction in the $\text{Al}_2\text{O}_3 + \text{C}$ system (Fig. 1, curves 5-6 and 2-3).

The coincidence of the experimental data of the system $\text{UO}_2 + \text{C}$ and $\text{UO}_2 + \text{UC}_2 + \text{C}$ (Fig. 4) shows that the addition of UC_2 to uranium oxide does not have any effect on the equilibrium pressure of CO in the presence of free carbon and at an identical O/U ratio in the final compositions of uranium dioxide. The uranium dicarbide additive remains inert with respect to UO_2 until the system is drawn out of the equilibrium state.

The experiments conducted on the systems "uranium dioxide-aluminosilicate additive-carbon" at a ratio $\text{SiO}_2/\text{Al}_2\text{O}_3 \geq 2/3$ show that during the degassing process of the systems at a residual pressure of $\approx 6.6 \cdot 10^{-5}$ Pa and a temperature of 1300-1800°K, the O/U ratio varies from 2.04 (for the original dioxide) up to 2.00; in this case, the smaller value of this ratio is determined either by the oxygen potential of SiO_2 or Al_2O_3 (when one of these

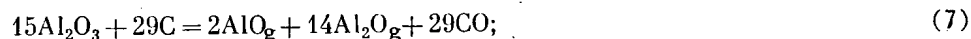
* $\Delta F^\circ \frac{\text{SiO}_g}{\text{SiO}_2} \log P^\circ \frac{\text{SiO}_g}{\text{SiO}_2}$ was evaluated on the basis of the published data [5, 6].

compounds is present in excess with respect to the composition of mullite) or by the oxygen potential of $3\text{Al}_2\text{O}_3 \cdot 2\text{SiO}_2$. When degassing of the experimental systems is carried out in the range 800–900°K, the equilibrium composition of the dioxide is determined by the oxygen potential corresponding to the upper limit (boundary) of the homogeneity range of aluminum or silicon oxides.

Based on the data on the interaction of uranium dioxide containing aluminosilicate additive with carbon under equilibrium conditions of the reaction (3), it can be concluded that it is advisable to maintain the $\text{SiO}_2/\text{Al}_2\text{O}_3$ ratio in aluminosilicate at a value different from that of mullite (2:3). In this case, the oxygen potential of Al_2O_3 and SiO_2 , and the pressure of CO corresponding to them are found to be higher than those observed in the case of $3\text{Al}_2\text{O}_3 \cdot 2\text{SiO}_2$. The final uranium oxide in the system consisting of UO_2 with aluminosilicate additive and carbon will also have higher O/U ratio. If the aluminosilicate additive contains excess Al_2O_3 with respect to the composition of mullite, the eutectic temperature of $\text{Al}_2\text{O}_3 \cdot \text{SiO}_2$ increases from 1870 up to 2100°K.

The obtained experimental and calculated thermodynamic data permit one to describe the interaction process of uranium dioxide containing additives with carbon.

Under equilibrium conditions and in the presence of excess silicon dioxide or aluminum oxide in the aluminosilicate additive with respect to mullite composition, the interaction of the oxide system with carbon is described by the following reactions



The pressure of CO corresponding to the reaction (8) must be equal to that determined from the reactions Eqs. (6) or (7).

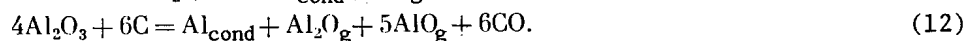
During the interaction process of UO_{2+x} with carbon, the composition of the dioxide is displaced towards the lower limit of the homogeneity range of UO_{2+x} [3] with a change in the O/U ratio. In view of more positive oxygen potential in the systems $\text{SiO}_2 + \text{C}$ and $\text{Al}_2\text{O}_3 + \text{C}$, the O/U ratio of the dioxide will be greater than the 2.00 that is typical for the lower limit of the stoichiometric composition of uranium dioxide [1].

When SiC is introduced into uranium dioxide, silicon carbide partially binds oxygen from UO_{2+x} as a result of the reactions



This binding process of oxygen is accompanied by a reduction in the O/U ratio of the original dioxide up to the equilibrium value that is determined by the pressure P_{CO} from the reaction (8).

Under nonequilibrium conditions, the interaction of uranium oxide containing aluminosilicate additive with carbon can lead to a state described by the reactions



During the occurrence of the reactions (11) and (12), isolation of silicon and aluminum can take place in the temperature range 1300–1800°K either in vacuum or in an inert gas current at a residual pressure of CO below 0.133 or 1330 Pa, respectively.

LITERATURE CITED

1. Yu. F. Khromov and R. A. Lyutikov, *At. Énerg.*, **49**, No. 1, 28 (1980).
2. Yu. F. Khromov et al., *ibid.*, **54**, No. 5, 360 (1983).
3. Yu. F. Khromov et al., *Zavod. Lab.*, **44**, 296 (1978).
4. D. Gruen, P. Finn, and D. Page, *Nucl. Techn.*, **29**, No. 3, 309 (1976).
5. V. P. Elutin and Yu. A. Pavlov, *Ferroalloys [in Russian]*, Metallurgizdat, Moscow (1957).
6. I. S. Kulikov, *Thermal Dissociation of Oxides [in Russian]*, Metallurgiya, Moscow (1969).
7. T. Nomura, M. Kotsura, and T. Sano, *J. Nucl. Mater.*, **43**, 234 (1972).

DETERMINATION OF THE TEMPERATURE DEPENDENCE OF THE DEMIXING OF AN EMULSION

S. M. Karpacheva, T. N. Shepeleva,
and S. N. Mel'nikova

UDC 66.061.5

The process of liquid extraction is divided into two stages: contacting of the phases with the formation of an emulsion, followed by the separation of the emulsion into its component phases.

In column extractors and mixer-settlers the separation of phases occurs under the effect of gravity. In multistage column extractors contacting occurs continuously during the counterflow motion of the two phases, one of which (continuous) fills the entire volume of the apparatus while the other (dispersed) moves in it in the form of drops which accumulate at the interface where they coalesce. Regardless of the number of theoretical stages of contact in the column separation occurs only once. In mixer-settlers the contacting is effected in a differential way in each stage with forward flow of both phases. The emulsion that is formed is then separated into two phases in the settling chambers of the apparatus, whose number corresponds to the number of stages.

The process of separation (demixing) of the phases takes place in several stages: coalescence of drops with each other, motion of the drops to the interface, and emergence of these drops across the interface into the continuous phase. The rate of demixing is affected by such physicochemical properties of the system as the surface tension, viscosity of the continuous and dispersed phases, difference of densities, drop sizes (i.e., the quality of the mixing), temperature, and the ratio of the phases in emulsions of the "oil in water" (O/W, direct) type and the "water in oil" (W/O, reverse) type.

The influence of the temperature on the demixing rate (v_d) has not been adequately elucidated although it is known that the temperature is elevated in order to improve the separation, especially stable emulsions in viscous systems (e.g., petroleum-water) [1].

The aim of this work is to determine the qualitative influence of the temperature on v_d of some extraction systems. Nine of the extraction systems used most often in industry were chosen for the investigations. The extracting agent TBP, which has been used extensively in practice (especially in the nuclear industry), was used in all the systems.

The systems studied can be divided into two groups according to the amount of extracting agent they contain: with undiluted TBP (100%) and with TBP diluted with synthine to a 20-25% volume fraction. In each of these groups the aqueous phase was represented by a concentrated solution (8 mole HNO_3 /liter), a weakly acidic solution (0.5 mole HNO_3 /liter), and various salt solutions [NH_4NO_3 , $\text{Al}(\text{NO}_3)_3$, Na_2CO_3].

For the investigations we used commercial TBP, which was not subjected to further purification and was identical with ordinary technical extracting agent containing impurities that have a complicated influence on the nature of the process of phase separation. As the aqueous phase we used solutions that were prepared on the basis of distilled water. The systems were first brought into equilibrium, after which the physicochemical characteristics of both phases and v_d were determined (see Table 1 and Fig. 1).

The work was conducted on an apparatus consisting of a laboratory impeller mixture and a measuring cylinder of diameter 65 mm and volume 400 ml with a millimeter scale for determining the height of the layer of the emulsion. The temperature of each experiment was kept constant by warming the initial solutions and the emulsion being studied.

The rotational speed of the mixer paddles was chosen to be constant (700 rpm). This made it possible, on the one hand, to maintain a constant energy input for emulsification and, on the other hand, to obtain a layer of emulsion throughout the volume of the phases.

Translated from *Atomnaya Energiya*, Vol. 59, No. 5, pp. 366-368, November, 1985. Original article submitted August 20, 1984.

TABLE 1. Temperature Variations of the Physicochemical Properties of the Two-Phase Systems Studied

No.	System	Phase density difference, ton/m ³	Phase viscosity, 10 ⁻³ N·sec/m ²		Interfacial surface viscosity, g/sec ²
			organic	aqueous	
I	100% TBP + 8 mole HNO ₃ /liter	0,14/0,146	5,50/2,87	1,33/0,86	10,64/11,32
II	100% TBP + 3.75 mole NH ₄ NO ₃ /liter	0,14/0,149	4,75/2,33	1,05/0,66	8,23/10,05
III	20% TBP in synthine + 0.5 mole HNO ₃ /liter	0,22/0,23	1,74/1,08	1,09/0,60	9,98/12,64
IV	25% TBP in synthine + 10% Na ₂ CO ₃ solution	0,29/0,3	1,76/1,11	1,72/0,98	9,59/11,44
V	25% TBP in synthine + 3.75 mole NH ₄ NO ₃ /liter	0,343/0,351	1,66/1,02	1,04/0,66	13,31/16,5
VI	25% TBP in synthine + 8 mole HNO ₃ /liter	0,49/0,485	1,58/0,95	1,61/0,97	14,44/1,56
VII	25% TBP in synthine + 0.83 mole Al(NO ₃) ₃ /liter + 0.5 mole HNO ₃ /liter	0,356/0,373	1,91/1,63	2,27/0,834	11,13/13,45
VIII	100% TBP + 0.83 mole Al(NO ₃) ₃ /liter + 0.5 mole HNO ₃ /liter	0,174/0,182	5,99/2,62	2,26/1,31	7,43/8,69
IX	100 TBP + 0.5 mole HNO ₃ /liter	0,022/0,0385	5,98/2,57	1,06/0,67	6,996/8,12

Note: The numerator gives the value at 20°C and the denominator gives the value at 50°C.

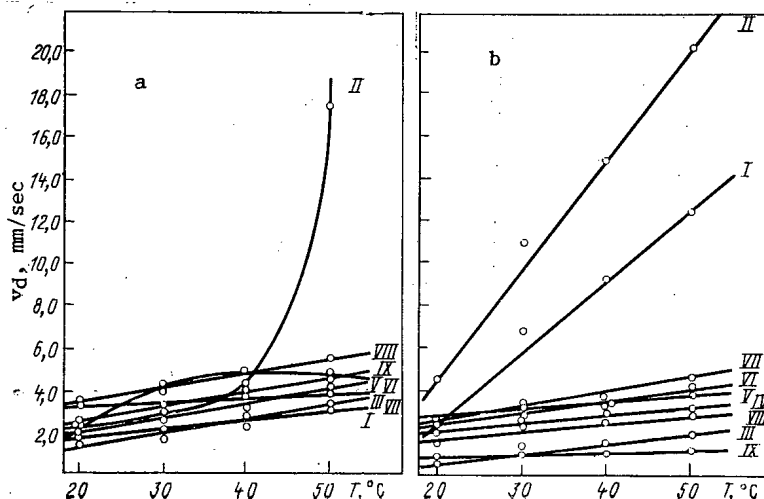


Fig. 1. Variation of the demixing rate and physicochemical properties for emulsions of the O/W type (a) and W/O type (b): for notation of I-IX see Table 1; O denotes experimental data and the solid lines represent averaged values.

The duration of the mixing of the phases for all the systems studied was 3 min, which corresponds to the usual average time for which solutions remain in the mixing chambers of operating mixing-settling extractors. The given type of emulsion was obtained by changing the position of the mixer paddles over the height of the layer. The mixer paddles were placed in the aqueous phase in order to get an O/W type of emulsion and in the organic phase to get a W/O type of emulsion.

The demixing rate of the emulsions studied and the physicochemical components were studied in the temperature range 20-50°C.

After the contacting process the mixer was switched off and v_d was determined by measuring the increment of the clarified layer on a millimeter scale. The demixing time was recorded with a timer and the temperature was recorded by a laboratory thermometer placed in the emulsion.

The volume ratio of the organic and aqueous reagents was chosen to be 1:1 for all systems apart from IV and 10:1 for IV (which is applicable to soda washing of the extracting agent in industry).

From the data presented in Table 1 and Fig. 1 it follows unambiguously that the demixing rates of the systems studied increase with increasing temperature and this dependence is nearly linear; accordingly, we can assume that this dependence has the form $v_d = kT + b$, where k is a coefficient that is determined by the physicochemical properties of the system

For the systems studied the total increase in v_d with increasing temperature is 150-200% for emulsions of the direct type and 40-60% for emulsions of the reverse type; an exception is that of system I for both types of emulsions and the reverse emulsion of system II, in which v_d increases by a factor of 5-7. This law also holds for direct and reverse emulsions; the absolute value of v_d for reverse emulsions in systems I and II is substantially higher than for the direct emulsion and this is at variance with the generally accepted view that the demixing rate of the direct emulsion is, as a rule, higher than that for the reverse emulsion.

The temperature affects the variation of the physicochemical properties as follows:

— The density of the organic and aqueous phases decreases slightly as the temperature increases and the change in the density difference is so small that its influence on v_d can be neglected.

— With increasing temperature the interfacial surface tension increases by 5-20% and this leads to the growth of the drop diameter [2], as a result of which v_d increases.

— Since the viscosity μ of the organic and aqueous phases decreases with rising temperature and since a drop of the dispersed phase (in order to coalesce with another such drop or with the interface) should overcome the resistance of the continuous phase, we can assume that the viscosity of the continuous phase should play an important role in the demixing process: a decrease in this viscosity leads to an increase in v_d with decreasing μ . The viscosity of the dispersed phase affects the nature of the motion of the drop itself.

As mentioned above, in systems with undiluted TBP the demixing rate v_d increases with increasing temperature to a much greater extent than in systems with diluted (25%) TBP, although the temperature variations of the physicochemical characteristics of these systems differ little. A change in the salt compositions of the aqueous phase also does not alter the nature of the laws found.

Thus, the work that we have done demonstrates how important it is for the indicated temperature regime to be observed during extraction; this makes it possible, if necessary, to increase the phase-demixing rate for extractors, in particular for mixer-settlers, i.e., to increase the output of the apparatus over fairly substantial limits.

LITERATURE CITED

1. G. N. Pozdnyshv, Stabilization and Destruction of Petroleum Emulsions [in Russian], Nedra, Moscow (1982).
2. Emulsions [in Russian], Khimiya, Leningrad (1972).

RADIATION DECOMPOSITION OF SURFACE-ACTIVE SUBSTANCES IN AQUEOUS SOLUTIONS

M. V. Vladimirova, V. P. Kermanov,
I. A. Kulikov, and M. N. Maslova

UDC 541.15

The waste water from atomic power plants contains a large amount of surface-active substances (SAS), whose presence hinders the use of traditional physicochemical methods (clarification, ion exchange) to decontaminate them. To date, such water has been concentrated by evaporation and the concentrates have been stored in special containers.

Activated-carbon sorption is one of the most widely applied methods of removing SAS from waste water. Until recently, however, the use of activated carbon to purify waste water on an industrial scale has proved to be economically unfeasible as a consequence of the small capacity of carbon (for SAS) and the complexity of the regeneration of "used-up" carbon. The method of radiation destruction of SAS requires aqueous solutions of SAS to be irradiated to large doses (10^6 - 10^7 Gy) to decompose them to the maximum permissible concentrations (MPC); this makes the method economically impractical since the cost of γ -radiation energy is high. In the Institute of Electrochemistry, Academy of Sciences of the USSR, workers have shown that the simultaneous sorption of organic substances and their radiation decomposition by ^{60}Co γ -ray quanta lead to the complete decontamination of waste water from pig-breeding complexes [1].

In this paper we present the results of experiments on the radiation-induced purification of aqueous solutions of anionic [e.g., sulfonol (SF)] and nonionic (OP-10) SAS, passed through a column of activated carbon as well as data on the radiation-chemical decomposition of SAS in aqueous solutions at pH 4-5. The concentration of SAS in aqueous solutions was monitored spectrophotometrically [2, 3].

The results of radiation decomposition of SF in solutions without air bubbling are given in Fig. 1. It is seen that as the γ -radiation dose increases the SF concentration [SF] decreases and the higher the initial [SF], the faster this decrease. For a given initial [SF] the decomposition rate of the SF decreases with increasing radiation dose. From the initial segments of the dose curves 10^3 - 10^4 Gy we determined the radiation-chemical yields of SF decomposition, G_{SF} . For solutions without air bubbling when the values of [SF] are 0.03 and 50.0 g/liter, $G_{\text{SF}} = 1.1$ and 4.0 molecules/100 eV, respectively. Similar experiments were carried out for aqueous solutions of OP-10 and they established that an increase in [OP-10] from 0.1 to 1.0 g/liter without air bubbling causes G_{OP} to increase from 0.1 to 0.8 molecule/100 eV. In the studied range of γ -ray doses from 10^2 - 10^6 Gy the maximum permissible concentration (≤ 0.5 mg/liter) for either SAS was not attained [4].

Experiments on radiation-sorption decontamination were carried out in activated-carbon columns with volumes of 25, 500, 1300, and 14,500 cm^3 . The sorptivity of the activated carbons AG-3, AG-5, and SAU was 13.0, 13.0, and 76.0 mg/cm^3 , respectively, for SF. Since the sorptivity of SAU carbon is more than five times that of AG carbon, subsequent work was conducted with carbons of this grade.

Studies were made of the sorption decontamination of aqueous solutions with different initial concentrations of SAS. We determined how the rate at which aqueous solutions are filtered through a column containing 1300 cm^3 activated carbon affects the SAS concentration in the filtrate; the filtration rate v_f was expressed in column volumes (c.v.) per hour. The SAS concentration in the filtrate depends significantly on the filtration rate and on the initial [SF] (Fig. 2). The values of the maximum permissible concentration (MPC) of SF in the filtrate for initial concentrations of 0.1, 0.5, and 1.0 g/liter are attained at filtration rates ≤ 2.0 , 0.1, and 0.05 c.v./h, respectively, in 10-24 h. Experiments on SF filtrations through an activated-carbon column, irradiated with γ -rays at a dose rate of ~ 0.3 Gy/sec, indicated that in this case the MPC of SF were attained at slightly higher values

Translated from *Atomnaya Energiya*, Vol. 59, No. 5, pp. 368-370, November, 1985. Original article submitted November 5, 1984.

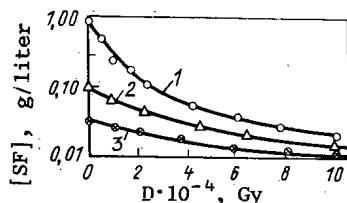


Fig. 1

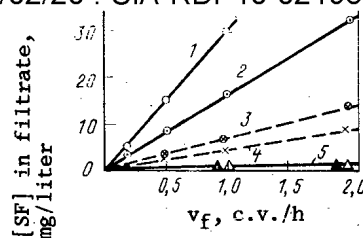


Fig. 2

Fig. 1. Influence of the γ -radiation dose (D) on the radiation-chemical decomposition of SF in aqueous solutions without air bubbling; 1, 2, 3) $[SF] = 1.0, 0.1, 0.03$ g/liter, respectively. (Here and henceforth in the figures the dose rate is 0.3 Gy/sec).

Fig. 2. Influence of the filtration rate, the initial $[SF]$, and γ -ray irradiation on the SAS content in the filtrate: 1, 3) $[SF]_{init} = 1$ g/liter; 2, 4) $[SF]_{init} = 0.5$ g/liter; 5) $[SF]_{init} = 0.1$ g/liter; \circ, \odot , and Δ) data obtained without γ -ray irradiation; \otimes, \times , and \blacktriangle) data obtained with γ -ray irradiation.

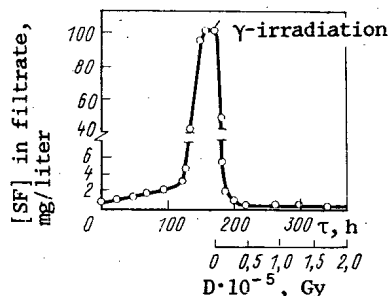


Fig. 3. Radiation-sorption decontamination of aqueous solution of SF at a filtration rate of 0.5 c.v./h (τ is the irradiation time).

TABLE 1. Restoration of the Filtering Capacity of SAU Activated Carbon for a Mixture of SF and OP-10

Irradiation time, h	Radiation dose $D \cdot 10^{-4}$, Gy	SAS conc. in filtrate, mg/liter	
		SF	OP-10
0		96,0	88,0
3	0,3	12,0	14,0
7,5	0,8	2,5	3,5
13,5	1,5	1,2	2,0
30	3,2	0,5	1,0
47	5,1	0,6	1,0
71	7,7	0,25	1,0

of the filtration rate, viz., $v_f = 0.2$ and 0.1 c.v./h for $[SF] = 0.5$ and 1.0 g/liter, respectively. On the basis of these experiments we can conclude that the simultaneous irradiation and filtration (in activated carbon) of aqueous solutions of SAS (SF) gives better decontamination than does just sorption alone. Moreover, the duration of filtration through the column in the absence of irradiation is limited by the sorptivity of the activated carbon while in the case of sorption with simultaneous irradiation the decontamination factors for the removal of SAS (SF) from the carbon do not become worse. The results of these experiments are presented in Fig. 3. Without irradiation a solution with an initial $[SF] = 0.1$ g/liter was passed through activated carbon at a rate of 0.5 c.v./h. After 120 the SF content in the filtrate reached the initial value, i.e., the carbon completely lost its sorptivity. Irradiation of the sulfonol-saturated carbon led to the total restoration of the sorptivity in $6-24$ h (γ -ray irradiation dose $5 \cdot 10^3 - 2 \cdot 10^4$ Gy) and the MPC was attained in $20-30$ h.

The decontamination factors for the activated carbon were maintained for ~ 60 days (γ -ray irradiation dose $\sim 1.5 \cdot 10^6$ Gy). Comparison of the descending branch of the curve in Fig. 3 with that of curve 2 in Fig. 1 indicated that the radiation-sorption decomposition of SAS (SF) is much more efficient than the radiation-chemical decomposition of SAS in solution.

Since waste waters contain a mixture of different surface-active substances, we studied the influence of γ -radiation on the sorptivity of SAU activated carbon with respect to a mixture of SF and OP-10 (~ 200 mg/liter). The experiments were performed in columns containing 25-1300 cm³ of carbon. The activated carbon was saturated with SAS prior to irradiation. From the results of the experiment (see Table 1) it is seen that during filtration of a mixture of SF and OP-10 the filtering capacity was restored at a filtration rate of 0.2-0.5 c.v./h seven hours after the onset of irradiation at a dose rate of 0.3 Gy/sec. Subsequently the decontamination factors for the carbon were maintained throughout the entire time of the experiment (~ 100 h).

Thus, the results obtained in the experiment demonstrated the efficiency of radiation-sorption decontamination in removing SAS from aqueous solutions.

LITERATURE CITED

1. V. N. Shubin, Khim. Vys. Énerg., 17, No. 5, 394 (1983).
2. R. V. Dzhagatspanyan, M. T. Gol'din, M. T. Filippov, et al., Introduction to Radiation-Chemical Technology [in Russian], Atomizdat, Moscow (1979), p. 259.
3. Standardized Methods of Water Analysis [in Russian], Khimiya, Moscow (1971), p. 348.
4. Regulations for the Protection of Surface Water from Contamination with Effluents [in Russian], Moscow (1975).

HYBRID RADIATION BACKGROUND MONITORING IN OPERATIONAL CONTROL AND FORECASTING OF ENVIRONMENTAL CONTAMINATION BY NUCLEAR POWER STATION DISCHARGES

I. S. Ereemeev, V. A. Eremenko,
V. S. Zhernov, Yu. A. Makarov,
V. V. Matveev, N. V. Ryzhov,
V. V. Ryazanov, and V. M. Skatkin

UDC 539.1.075.2.621.039.58

Rapid developments in nuclear power have stimulated research on monitoring and forecasting environmental radiation pollution (ERP), and in particular the amounts, compositions, and distributions of radionuclides in the environment. In the early days of nuclear power, the high reliability in power station equipment made it sufficient to use existing systems for monitoring discharges in order to check obedience to permissible norms and to analyze environmental samples. Improvements are required now to such systems in order to record ERP in the regions of some multiunit power stations, and also because of increased interest in the contribution of the man-made component to the radiation background, the increase in the number of users of ERP information, and the need to provide ready-made systems for detecting emergency situations. These measures involve certain costs, so one is justified in performing a preliminary search for optimal solutions [1, 2].

The system has distributed parameters, so there are certain difficulties in direct ERP measurement at many points in order to provide the required reliability (environmental monitoring). Radiation-monitoring stations require power supplies and equipment support, as well as links to the central control, and access for servicing and repair. Even if the structure is optimized, one requires about 80 detectors at least for the most unfavorable class of stability at a distance of 4000 m from the discharge point, and the number increases rapidly at larger distances [3], when allowance is made for the ERP detector radius of action, the atmospheric stability class, the distance to the discharge source, the signaling threshold, the exposure duration, and the length of the line joining the detectors (at the perimeter) to the center.

Translated from Atomnaya Énergiya, Vol. 59, No. 5, pp. 370-372, November, 1985. Original article submitted March 29, 1985.

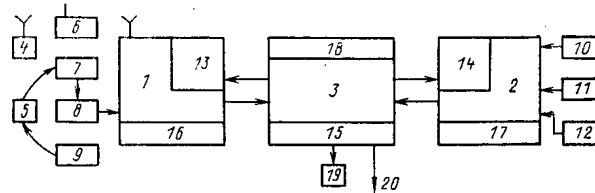


Fig. 1. Conceptual model for hybrid environmental radiation pollution monitoring: 1-3) central reception and processing computers (systems for measurement, simulation, and hybrid monitoring correspondingly); 4 and 5) mobile local monitoring facilities; 6, 8, and 9) data-acquisition stations; 7) receiver for remote reception of mobile monitoring data; 10 and 11) units monitoring discharges and effluents; 12) meteorological parameter monitoring; 13) calculated ERP values for observing man-made part; 14) model bank for ERP propagation; 15) output data; 16-18) software; 19) ERP data users; 20) data transmission to regional monitoring system; Y) radiocommunication; →) wire line.

An important factor is that one must measure man-made ERP at the largest possible distances from sources under conditions of natural radiation backgrounds exceeding the ERP by factors of 10-100.

An alternative to measurement monitoring is model monitoring, i.e., calculating the ERP concentration patterns on the basis of data on the size of the discharge, the initial distribution, and the hydrometeorological factors, which are inserted into an ERP propagation model. Deriving reliable data in that case also involves certain difficulties because of the incomplete data on the atmospheric state, behavior in the atmosphere of particles containing radionuclides, and the possibility of an unmonitored discharge. An idealized or simplified model leads to discrepancies between the calculations and the actual ERP distribution increasing with distance and time if the actual particle propagation conditions deviate from the ideal ones in the model. The complexities in model monitoring are due also to the increase in the amount of input data required as one increases the scale on which the ERP propagation is considered. Also, model monitoring has heavily delayed feedback or none at all, which is bound to affect the ERP evaluation performance [4]. There are ongoing changes in hydrometeorological factors influencing ERP, which makes it difficult to adjust the model, which has to be an ongoing task accompanying the monitoring.

Recently, it has been suggested that the two should be combined (measurement and models) to make optimum use of the experimental data [5, 6]. However, what one needs is not a simple union of these methods but realistic minimization or compensation of the disadvantages in each method separately, while making maximal use of the advantages.

Hybrid monitoring (Fig. 1) provides continuous adaptation of a model for ERP propagation to the detailed changing conditions on the basis of local measurements.

Then when there is an emergency, the model operates in a fashion most closely corresponding to the actual meteorological conditions, and the ERP data given by the model enable one to distinguish changes due to the man-made component from random fluctuations in the natural background.

The measurement system in general includes mobile and stationary data-acquisition facilities linked by wire or radio to the central point.

A mobile laboratory may not only make measurements but also receive data from stationary installations not having their own communications with the center and transmit the data under field conditions via the special reception point at another station in communication with the center. The measurement system receives information not only from the locality but also from the model, which enables one to use measurements at the perimeter to identify the man-made component [7]. The system also accumulates and stores data on the radiation environment, which are edited on the basis of the radioactive, chemical, and other transformations, and it serves to control the data acquisition and the mobile facilities in accordance with the processing results; it also interpolates the ERP distributions between the monitored points and detects trends and anomalies in the ERP.

The mobile facilities operate with data-acquisition stations not having permanent links to the center and have facilities for environmental sampling, performing radiometric and spectrometric analyses on samples under field conditions, processing the data by microcomputer, and transmitting the results by radio or data-reception points to the center. The data-acquisition stations are located on the basis of the local ecological features and are equipped with continuous-running γ -ray exposure dose rate monitors, in which the man-made component can be distinguished from the natural background (for example, on spectral characteristics [7]); the stations also sample aerosols on filters, collect precipitation, and have devices for preprocessing the data and transmitting it to the center.

The computerized simulation system for radionuclide distributions (model monitoring) contains units for generating the input data on the size, initial distribution, and spectral composition of the discharge, as well as a system handling hydrometeorological information on a current basis and statistically processed over a given time interval, which is required in the simulation with the set of models for ERP propagation, which incorporate the environmental inhomogeneity, the boundary conditions, the propagation scales, radioactive decay, and chemical and other reactions.

The compilation and analysis system compares the output data from the model with the measurements for fixed points, adapts the model to the actual circumstances by correcting or replacing the model from the available set, and contains a software suite for running sequentially through the ERP models, choosing a model providing data closest to the measurements, and then adjusting the model coefficients to improve the model fit to the actual ERP propagation conditions. One should envisage a software suite also for selecting the multi-level model most closely reflecting the ERP at medium and large distances; one needs a computerized data bank on the radiation environment in the region, which can generate periodic and one-off reports; and this should also support interaction with other data-processing and managerial systems requiring ERP information or with systems providing additional information on the radiation environment and the associated factors in the region.

This conceptual model combines the methods and means of simulating ERP propagation, the methods and means of monitoring the actual ERP distribution, methods of distinguishing man-made signals from the natural radiation background to provide a given reliability in the processing results, and in particular means of periodic model adaptation from the measurements. One way of optimizing the adaptation is described in [8]. The calculations for points at which the system checks against the measurements are used with the measured values as corrected for short-lived nuclide decay, washout, precipitation, transport time, and actual meteorological conditions; the comparison is made in order to check the model accuracy. If the discrepancies in a locality exceed a limit, the system directs model editing, which may involve adjusting individual coefficients or altering the model structure as a whole. The editing is performed in two stages: in the first, one uses the old calculations on the concentration pattern, when the model is adjusted to certain input data, while in the second stage, the calculations are based on the new data and checked against the latter. The process can be iterative, with the model adjusted after the second stage in each cycle by trial and error or by Monte Carlo methods.

The purpose of hybrid monitoring is ultimately to analyze trends in order to detect elevated discharges and thus to output data to the regional monitoring system.

LITERATURE CITED

1. V. S. Zhernov, I. S. Krashenninnikov, V. V. Matveev, et al., "Data support to the dosimetric operator at Soviet nuclear power stations," in: Nuclear Power Experience, Vol. 4, IAEA, Vienna (1983), p. 351.
2. É. P. Bolkov, A. I. Glushchenko, V. N. Durnev, et al., "The design of automated radiation-monitoring systems for the environment at nuclear power stations," *At. Energ.*, 57, Issue 1, 32 (1984).
3. M. Kümmel, "Developing an optimal network for environmental monitoring at nuclear power stations," in: Providing Radiation Safety in Operating Nuclear Power Stations [in Russian], Issue 5, Énergoatomizdat, Moscow (1983), pp. 78-89.
4. B. N. Bronin and L. I. Erdman, "The scope for correcting input data, theoretical models, and calculated concentration patterns for man-made pollutants from measurement data," *Trudy IPG*, Issue 41, 35-42 (1982).

5. E. N. Teverovskii, E. S. Dmitriev, and G. S. Kirdin, Computerized Systems for Forecasting and Monitoring Atmospheric Pollution in Accidental Discharges from Nuclear Power Plants [in Russian], Energoatomizdat, Moscow (1983), p. 136.
6. T. Stuart, T. Hendricks, G. Wallace, and J. Cleland, "An airborne system for mapping and tracking extended gamma ray sources," in: Measurement, Detection and Control of Environmental Pollutants; Proc. Symp. Vienna, 15-19 March, 1976, IAEA, Vienna (1976), pp. 319-326.
7. S. Moriuti, "A method of measuring and estimating environmental environmental gamma radiation doses at the level of 5 mber a year," Radioisotopes, 28, No. 8, 519-527 (1979).
8. R. Shannon, System Simulation: Art and Science [Russian translation], Mir, Moscow (1978), p. 420.

CHARACTERISTICS OF THE PROPAGATION IN THE GROUND LAYER OF THE ATMOSPHERE OF THE RADIONUCLIDES EMITTED DURING THE REGENERATION OF FUEL ELEMENTS

I. N. Ruzhentsova, R. V. Semova,
E. N. Teverovskii, and I. A. Ternovskii

UDC 004.86

When depleted fuel elements are regenerated, long-lived radioactive substances in gaseous and aerosol form are discharged into the atmosphere. The scattering of radioactive gases (for example, ^{85}Kr) in the ground layer of the atmosphere is governed by the known laws of turbulent diffusion for a weightless impurity. The range of sizes of radioactive-aerosol particles entering the atmosphere is fairly broad: together with fine particles, there may also be coarse particles discharged into the atmosphere, and this leads to the appearance of substantial rates of gravitational deposition onto the surface of the earth. It is therefore of interest to investigate the characteristics of the scattering of discharged radioactive aerosols in the ground layer of the atmosphere, i.e., the distribution of the dilution factors and deposition rates at various distances from the source.

When the discharge is continuous, the dilution factor k_p is the volume of air necessary for the scattering of an impurity discharged by a source per unit of time divided by the corresponding value of ground concentration: $k_p = Q/C$, where Q is the rate of discharge and C is the ground concentration. The dilution factors were found from the data of simultaneous measurements of the discharge rate and the concentrations of radionuclides in the ground layer of the atmosphere, which were determined by selecting specimens of atmospheric air in an emission jet at a distance of 0.8-12 km from the source. The rate of discharge into the atmosphere was measured by selecting specimens of aerosols from a gas-and-air mixture leaving a ventilation pipe 150 m high. The radionuclide composition of the aerosols was determined by means of a gamma-spectrometric apparatus. In the collection of the atmospheric-air specimens, the meteorological parameters (wind velocity at heights of 2 and 10 m, temperature difference between the heights of 4 and 1 m) were measured continuously in the jet. The results of the meteorological observations were averaged over the period of measurement of the ground concentration (0.5-3 h), and this was followed by calculation of the average over that interval of the value of the parameter B , which served as a criterion of the stability of the ground layer of the atmosphere [1]: $B = gH'\Delta T/(Tu_2^2)$, where g is the acceleration of gravity; T is the average temperature in the ground layer of the atmosphere; ΔT is the difference between the temperatures at heights of 4 and 1 m; u_2 is the wind velocity at a height of $H' = 2$ m.

In evaluating k_p , it must be borne in mind that the radioactive-substance content in the ground layer of the atmosphere in the direction of the prevailing winds may be caused not only by the discharge but also by the action of the windblown migration of aerosols from previously contaminated areas of ground surface. The contributions made by these factors depend not only on the rate of discharge and the density of surface contamination but also on the combined influence of the meteorological conditions (thermal stratification of the ground layer of the atmosphere, wind velocity) and the condition of the underlying sur-

Translated from Atomnaya Energiya, Vol. 59, No. 5, pp. 373-375, November, 1985. Original article submitted August 3, 1984.

TABLE 1. Dilution Factor of Radioactive Aerosols

State of thermal stratification	Distance from source, km	Dilution factor, m ³ /sec	
		aerosol	weightless impurity [3]
Very unstable, or unstable	0,8—1,8	(5,6—15) 10 ⁵	(3,6—9,5) 10 ⁵
Neutral	2,6—5,2	(4,2—22) 10 ⁶	(3,3—12) 10 ⁶
Stable, or very stable	6—12	(3,6—15) 10 ⁶	(3,9—14) 10 ⁶

TABLE 2. Rate of Deposition of Radioactive Aerosols

Distance from source, km	¹⁹⁶ Ru	¹³⁷ Cs	¹⁴⁴ Ce
0,3	0,6—8,5	0,8—6,4	0,8—8,3
0,6	0,6—2,3	0,4—11	0,5—4,3
0,9	0,2—1,8	0,6—3,9	0,4—1,9
1,6	0,1—0,9	0,4—2,0	0,3—2,3
2,1	0,2—1,8	0,4—0,9	0,7—3,5
3,5	0,1—0,7	0,8—3,5	0,4—2,4
5,0	0,3—0,6	0,3—2,1	0,8—1,2
10	0,2—0,8	1,8—3,0	1,8—2,2
20	0,5—0,7	0,7—1,0	1,0—2,3

Note. At distances of 0.3–0.6 km from the source, the 10-day average wind velocity at a height of 10 m is $u_{10} = 2.0$ – 6.7 m/sec, the amount deposited is $h = 3.0$ – 30 mm; at distances of 0.9–20 km from the source $u_{10} = 3.5$ – 5.5 m/sec, $h = 8.0$ – 47 mm.

face (presence of grass cover, soil moisture). The component of the ground concentration that is due to the discharge into the atmosphere (C_Q) can be estimated as follows [2]:

$$C_{Q1} = \frac{\delta_Q}{\delta_C} (C_e - C_b)_1 \frac{\delta_\sigma - \delta_C}{\delta_\sigma - \delta_Q};$$

$$\delta_Q = \frac{Q_1}{Q_2}, \quad \delta_\sigma = \frac{\sigma_1}{\sigma_2}, \quad \delta_C = \frac{(C_e - C_b)_1}{(C_e - C_b)_2};$$

$$C_{Q2} = \frac{C_{Q1} Q_2}{Q_1},$$
(1)

where C_e is the experimental value of the ground concentration; C_b is the concentration caused by the overall background; σ is the density of the contamination on the earth's surface; the subscripts 1 and 2 refer to different radionuclides whose scattering in the ground layer of the atmosphere is governed by the same laws (such radionuclides are primarily isotopes).

By using the formulas (1), we can determine the dilution factors for aerosols at different conditions of thermal stratification of the ground layer of the atmosphere for an averaging time of 30 min (Table 1). To pass from other measurement periods to the 30-min period, we used the empirical relation [3]

$$\frac{C_1(\tau_1)}{C_2(\tau_2)} = \left(\frac{\tau_2}{\tau_1} \right)^{0.2},$$
(2)

where C_1 and C_2 are the values of the ground concentration for the averaging periods τ_1 and τ_2 , respectively.

TABLE 3. Ratio of the Minimum Dilution Factor of Aerosols to the Minimum Dilution Factor of a Weightless Impurity

State of thermal stratification	$x_{v\min}$, km	$k_{pv\min}/k_{p\min}$
Moderate instability	1—1,2	0,6—1,0
Neutral state	2,5—3,6	0,4—1,0
Weak or moderate inversion	2,7—6,0	0,1—0,6
Strong or moderate inversion	4,4—10	0,1—0,6

Note. The first values are given for a deposition rate of 10 cm/sec, the second values for 1.3 cm/sec.

At distances of 0.8–12 km from the source, the dilution factors of the radioactive aerosols and the weightless impurity differ within the limits of error of the determination ($\leq 40\%$). Thus, at distances > 0.8 km the contamination of the ground layer of the atmosphere is caused primarily by the radioactive particles, which do not have any practically appreciable rate of gravitational deposition and are scattered in the atmosphere under the action of turbulent diffusion. This conclusion is also confirmed by the data of measurements of the deposition rate of radioactive aerosols at distances of 0.9–20 km from the discharge source.

The rate of deposition onto the ground surface, v , was determined from the results of simultaneous measurements of the ground concentration and the density of precipitation of aerosols onto the surface of planchettes made of FP fabric set up at control points at distances of 0.3–20 km from the source (Table 2):

$$v = \sigma' / [(C_e - C_b) \Delta t], \quad (3)$$

where σ' is the density of contamination of the planchette surface; $\Delta t = 10$ days is the period of observation.

As can be seen from Table 2, within the range of 0.9–20 km from the source the rate of deposition is practically independent of the position of the measurement point and the type of radionuclide. In this range there is no clear dependence of v on the meteorological characteristics. The average value of the rate is 1 ± 0.2 cm/sec. At distances < 0.6 km from the source the rate of deposition may be considerably greater than 1 cm/sec, and this is due to the presence of larger aerosol particles in the solid or liquid phase (the latter include, for example, condensate droplets). The deposition of these aerosols is influenced not only by the turbulent displacement but also, to a considerable extent, by gravity forces (the error in determining the rate was $\leq 45\%$).

The results of the measurements of the dispersed state of the aerosol particles in the ground layer of the atmosphere obtained by means of a multicascade impactor showed that at distances > 1 km from the source of the discharge the contribution made by particles with diameter ≥ 8 –10 μ m is about 20%.

For the estimate of the minimum dilution factor of the deposited impurity, $k_{pv\min}$, we can use the relation $k_{pv\min} = k_{p\min} / \varphi(v)$, where $k_{p\min}$ is the minimum rate of dilution of the weightless impurity; $\varphi(v)$ is a dimensionless function of the parameter v ; $v = v / (Bu)$ (B is the vertical-scattering parameter, which depends on the state of thermal stratification of the ground layer of the atmosphere; u is the average wind velocity in the layer from 0 to the height of the discharge source). The function $\varphi(v)$ in the general case is determined in accordance with the numerical solution of the equation of turbulent diffusion for the deposited impurity [1, 4]. For the same deposition rate, the values of $k_{pv\min}$ are different, depending on the intensity of the turbulence. For the zone of minimum dilution (maximum concentration) we have $\varphi \geq 1$, and for greater distances $\varphi < 1$. For a deposited impurity the zone of minimum dilution, $x_{v\min}$, is situated closer to the source of height H than for a weightless one [1]:

$$\begin{aligned}x_{v_{min}} &= H/[B(2+v)] \quad v \leq 1; \\x_{v_{min}} &= Huf(v)/v \quad v > 1,\end{aligned}\tag{4}$$

where $f(v)$ is a dimensionless function of the parameter v , which, like $\varphi(v)$, is determined by starting from the solution of the equation of turbulent diffusion. According to Stokes's law, which defines the rate of deposition of spherical particles as a function of their radius, rates of 1.3 and 10 cm/sec are characteristic of particles with diameters of 20 and 50 μm , respectively, for a density of 1 g/cm³. As can be seen from Table 3, as the meteorological conditions change from moderate instability to a neutral state, the minimum values of the dilution factors for a weightless impurity and for aerosols with a deposition rate of 10 cm/sec differ by a factor of about 2-2.5.

The presence of inversion conditions in the atmosphere leads to a decrease of $k_{pv_{min}}$ in comparison with a weightless impurity by a factor of up to 10. For a deposition rate of 1.3 cm/sec the minimum values of the dilution factors of aerosols and of a weightless impurity differ by a factor of no more than 2 under stable conditions, while for other states of thermal stratification they are practically equal.

In conclusion, the authors wish to express their gratitude to M. V. Ashanin and V. N. Solov'ev for their assistance in carrying out the experimental work.

LITERATURE CITED

1. N. P. Byzova, Methodological Textbook on the Calculation of the Scattering of Impurities in the Boundary Layer of the Atmosphere [in Russian], Gidrometeoizdat, Moscow (1973).
2. R. V. Semova, I. A. Ternovskii, and A. F. Tret'yakova, IAEA-SM-191/35. IAEA, Vienna (1975).
3. N. E. Artemova, I. N. Ruzhentsova, R. V. Semova, et al., "Variation of the ground concentration of radionuclides discharged from pipes as a function of averaging time," *At. Énerg.*, 51, No. 2, 112-116 (1981).
4. M. E. Berlyand, Modern Problems in Atmospheric Diffusion and Atmospheric Pollution [in Russian], Gidrometeoizdat, Leningrad (1975).

POSSIBILITY OF DETERMINING NUCLEAR-FUEL CHARACTERISTICS BY MASS
SPECTROMETRY WITHOUT CHEMICAL SEPARATION OF THE ELEMENTS

V. V. Kalygin, V. Ya. Gabeskirya,
and V. I. Borisenkov

UDC 621.09.54:539.128.4.144:539.166.3

In order to correctly organize the fuel cycle of a nuclear power plant, it is necessary to know such characteristics of the spent nuclear fuel as the burnup and the content of transuranium elements in it. The mass-spectrometric method of isotopic dilution is used to determine them accurately [1]. As a rule, in performing such measurements, a three-ribbon ion source, which requires a sample of very high purity, is used. Since the relative content of the series of analytes in it is low while the content of external impurities is high, the elements of the sample must be chemically separated [2].

The process of chemical separation of the analytes is laborious and can distort the results of the analysis. Thus it has been established that when neodymium ($\sim 2 \mu\text{g}$) is chemically separated from the fuel sample with the help of a 1×8 ($\sim 0.3 \text{ g}$) Dowex ion-exchange resin, it is contaminated by $\sim 4 \cdot 10^{-2} \mu\text{g}$ of natural neodymium.

The ion source with surface ionization in a partially closed cavity [3], developed for the mass spectrometer, not only substantially raises the sensitivity of the device when working with transuranium and rare-earth elements, but it also enables the analysis of mixtures of these elements with a high salt content as well as the determination of the characteristics of the spent fuel without chemical separation of the elements [4].

Thus we studied a sample of spent fuel, cut out of the center of a fuel cell of the RBMK-1000 reactor and dissolved (without removing the jacket of the fuel cell) in nitric acid. To perform the isotopic analysis of U and Pu as well as of the fission products of Cs, Ce, and Nd, used as monitors of fuel burnup, we extracted from the given solution an aliquot containing $\sim 5 \mu\text{g}$ of fuel, which we placed into the evaporator of the ion source, where we evaporated it to the point of dryness.

In performing the mass-spectrometric analysis, while increasing the temperature of the evaporator we successively recorded the following groups of mass spectra: Cs, Ce, and Nd and their oxides, Pu, and U. The mass spectrum of Nd and Ce contains peaks with the same mass numbers. During analysis the Nd ion current substantially exceeds the Ce ion current, and the reverse ratio is observed for their oxides. Taking this into account, we calculated by the method of iteration the isotopic ratios of Ce and Nd. We calculated the first approximation for the ratios $^{142}\text{Ce}/^{140}\text{Ce}$ and $^{144}\text{Nd}/^{143}\text{Nd}$ from the mass spectra of the oxides and of the atoms, respectively; while for $^{142}\text{Nd}/^{143}\text{Nd}$ and $^{144}\text{Ce}/^{140}\text{Ce}$ we calculated the first approximation using the above-obtained ratios and values in the mass spectra of the intensity of the currents of the ions $^{140}\text{Ce}^+$ and $^{144}\text{NdO}^+$. We did not take into account the content of the nuclides ^{148}Nd and ^{150}Nd , because Sm, which has the same isobars, was present in the sample.

We recorded the Pu spectra after the ratio of the intensities of the currents of the ions $^{243}\text{Am}^+$ and $^{241}\text{Pu}^+$ (Am is more volatile) dropped below 0.01 as the temperature of the evaporator was raised. In this case, within the limits of error of the measurements, the presence of Am in the sample did not affect the results obtained.

In recording the mass spectra of Cs and U we did not observe the superposition of peaks of other elements. Even in this case, however, we monitored the absence of isobars of impurities according to the peaks on neighboring mass lines and according to the constancy of the isotopic ratios calculated.

To determine the content of U and Pu and of fission products in the spent fuel, we added a complex marker, containing a known concentration of the nuclides U, Pu, Cs, Ce, and

Translated from Atomnaya Énergiya, Vol. 59, No. 5, pp. 378-379, November, 1985. Original article submitted April 2, 1984.

TABLE 1. Content of Some Nuclides in the Sample of Spent Fuel

Element	Mass fraction relative to uranium in the spent fuel, $\times 10^{-2}$	Mass number	Mole fraction, %
U	100	234	0,0096 (1) *
		235	0,545 (7)
		236	0,204 (5)
		238	99,240 (7)
Pu	0,437 (8) *	239	54,2 (3)
		240	33,7 (2)
		241	8,3 (1)
		242	3,80 (5)
Cs	0,210 (4)	133	48,0 (6)
		134	0,519 (3)
		135	11,38 (4)
		137	40,11 (54)
Ce	0,184 (4)	140	53,3 (2)
		142	46,4 (2)
		144	0,30 (7)
Nd	0,263 (5)	142	0,6 (2)
		143	23,7 (4)
		144	37,6 (3)
		145	20,1 (2)
		146	18,04 (13)

TABLE 2. Burnup of the Fuel Sample, %

Burnup monitor	Analysis	
	1	2
^{133}Cs	—	1,58
^{137}Cs	—	1,57
^{140}Ce	1,68	1,56
^{142}Ce	1,59	1,48
$^{143}\text{Nd} + ^{144}\text{Nd}$	1,51	1,53
$^{145}\text{Nd} + ^{146}\text{Nd}$	1,50	1,58
Average burnup	1,55 (4)	

*Here and below the statistical error, corresponding to a confidence probability of 0.95 and referring to the last significant numbers of the corresponding quantity, is presented in parentheses.

TABLE 3. Characteristics of Burnup of a Sample of Spent Mixed Fuel from the BOR-60 Reactor

Analysis	Mass fraction of nuclides relative to uranium		Fuel burnup, %
	Pu	$^{145}\text{Nd} + ^{146}\text{Nd}, \times 10^{-2}$	
1	0,220 (4)	0,838 (8)	9,5 (1)
2	0,227 (3)	0,835 (7)	9,35 (7)
3	0,234 (5)	0,840 (9)	9,46 (14)

Nd, to the aliquot of the starting solution, containing $\sim 3 \cdot 10^{-4}$ g of fuel. For analysis on the mass spectrometer we extracted a sample containing ~ 0.1 μg U.

Table 1 shows the results of the measurements of the isotopic composition and mass of some elements accumulating in the fuel (relative to uranium). We used these data to calculate (using the method of heavy atoms [1]) the burnup of the nuclear fuel and the contribution of fission of heavy nuclides ^{235}U , ^{238}U , ^{239}Pu , ^{241}Pu to it. Using the values of these contributions, we calculated a more accurate value of burnup based on the accumulation of fission products [1] (Table 2).

Using the same method we determined the characteristics of the spent mixed fuel of the BOR-60 reactor. To determine the isotopic composition of U, Pu, and Nd, we loaded ~ 2 μg of fuel into the evaporator, and to determine the required isotopic ratios we loaded ~ 0.1 μg of the fuel mixture with the marker. Because of the peculiarities of the neutron spectrum of the fast reactor (BOR-60), we determined the burnup only from the total accumulation of ^{145}Nd and ^{146}Nd . To calculate the effective yield of ^{145}Nd and ^{146}Nd (with fission of the nuclei in the fuel), we calculated the relative fraction of the fissions of each of the heavy nuclides on a computer. In doing so we used the experimental and computed values of the ratios of the nuclide-neutron reaction rates [5, 6]. The error in the determination presented in Table 3 is the random error, characterizing this method of measurement; its

total value is determined taking into account the error in the yield of the fission products of ^{145}Nd and ^{146}Nd ($\sim 5\%$).

It has thus been shown that the use of an ion source with surface ionization in a partially closed cavity enables determining the basic characteristics of the spent nuclear fuel without purification and chemical separation of the fuel elements from the sample.

As a result, the labor involved in the method drops substantially, the speed of the measurements increases, and errors introduced by contamination of the samples during separation and purification, are eliminated. The amount of high-activity sample required for determining the fuel characteristics is at least two orders of magnitude smaller than required for the three-ribbon ion source. The full complex of measurements can be carried out with a $\sim 10\text{-}\mu\text{g}$ fuel sample.

LITERATURE CITED

1. Yu. B. Novikov, V. Ya. Gabeskiriya, V. V. Gryzina, et al., "Determination of fuel burnup in a water-cooled-water-moderated nuclear power reactor," *At. Énerg.*, **43**, No. 4, 240-242 (1977).
2. V. Ya. Gabeskiriya, A. A. Zaitsev, V. V. Mikulenok, et al., "Determination of the content of uranium isotopes and isotopes of transuranium elements in spent fuel from VVER-365," *At. Énerg.*, **44**, No. 5, 446-448 (1978).
3. V. V. Kalygin, V. Ya. Gabeskiriya, V. I. Raiko, et al., "Ion source for microquantitative isotopic analysis of transuranium elements," *Prib. Tekh. Éksp.*, No. 4, 171-173 (1980).
4. V. V. Kalygin and V. Ya. Gabeskiriya, "High-efficiency source of ions for analysis of transuranium elements," in: *Abstracts of Reports at the 2nd All-Union Conference on the Chemistry of Transplutonium Elements*, Dimitrovgrad (1983), p. 103.
5. V. M. Gryazev, V. Ya. Gabeskiriya, G. I. Gadzhiev, et al., "Experimental studies of burnup and components of the conversion factor in BOR-60 reactor," Preprint NIIAR-25 (359), Dimitrovgrad (1978).
6. V. S. Prokopenko, A. V. Inchagov, Yu. B. Novikov, et al., "Measurement of the value of α for ^{235}U , ^{238}U , and ^{239}Pu in the active zone of the BOR-60 reactor," *At. Énerg.*, **45**, No. 3, 230-231 (1978).

SYSTEM OF COMPUTATION OF THE REACTIVITY BALANCE FOR THE BOR-60 REACTOR

V. N. Efimov, S. N. Eshchenko,
V. A. Kachalin, A. S. Nikol'skii,
and V. N. Pridachin

UDC 621.039.514

One of the most effective techniques of diagnosing the state of a fast reactor involves computation of the reactivity balance (CRB). It is widely used abroad and gave satisfactory results in the course of experiments with a breadboard model of the CRB system on the BOR-60 reactor [1]. An abnormal reactivity ρ_a can be determined by solving the reactivity-balance equation

$$\rho_a = \rho_k - \rho_e - \rho_b \quad (1)$$

where ρ_k is the total reactivity at the reactor as determined from the equations of the point kinetics; ρ_e , reactivity which is due to a change of reactor parameters and to a control-rod displacement; ρ_b , reactivity which is caused by a change of the nuclide composition and by fuel swelling.

For detecting failures related to the melt-down of a fuel assembly (FA) [2], monitoring of abnormalities preceding the melt-down (blocking of FA and sodium boiling) must be provided for. A change of reactivity in BOR-60 due to these abnormalities is $(1-5) \cdot 10^{-5} \Delta k/k$. On the other hand, uncorrelated fluctuations of reactor parameters and of sensor signals lead to reactivity changes as high as $0.6 \cdot 10^{-5} \Delta k/k$ [3] in the frequency range of 0.01-5 Hz. This value specifies a limiting sensitivity which should be aimed at when developing a CRB system.

Translated from *Atomnaya Énergiya*, Vol. 59, No. 5, pp. 379-381, November, 1985. Original article submitted December 7, 1984; revision submitted March 4, 1985.

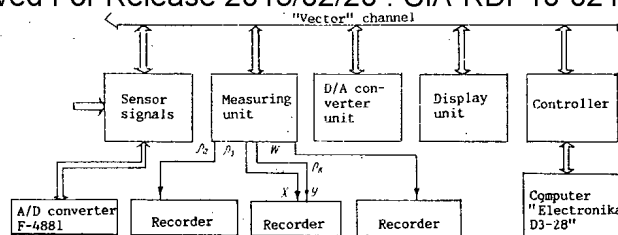


Fig. 1. Block diagram of the CRB system.

The principal requirements to a CRB system are high sensitivity to abnormalities which depends, in an instrumental sense, on the sensitivity as well as on the performance stability of sensor-signal transducers in the frequency range 0-10 Hz, and a functional flexibility which allows a refinement of the program and of computational parameters for a particular reactor. The systems based on digital computation of the reactivity balance meet these requirements to a large measure. The use of a computer common to the whole power station for CRB in real-time operation mode is, however, limited due to a relatively long sensor-interrogation cycle time (seconds).

Taking into account this limitation, a digital CRB system has been developed using a standard Soviet made special-purpose control computer "Elektronika D3-28" as the base. This desk-top minicomputer combines high-precision computation by decimal arithmetic (12-digit mantissa, 2-digit order) and a sufficiently high speed of binary operation (addition time for two-byte format numbers is 0.12 msec) with ease of programming. Input-output equipment of the system has been made in conformity with the "Vector" standard. Its structure makes it possible to build up the system by adding blocks, e.g. for the organization of a communication channel with a computer common to the whole station. In addition to the abnormal reactivity determined from Eq. (1), it calculates also the reactivity ρ_k [4], the reactivity margin ρ_m in safety and control rods, reduced to reactor nominal parameters ($\rho_m = \rho_k - \rho_e$), and the reactor energy production W . These characteristics are of an independent importance for the reactor operation as they make it possible to provide for the calibration of safety and control rods and for the prediction of the reactor operating period between fuel rechargings.

The signals of standard sensors of the flow rate, temperature, neutron power, and the outputs of the four synchro pickups of safety and control rod position after the corresponding conversions enter the analogous inputs of a measuring unit. The signals are amplified, filtered, and fed to the input of an A/D-converter in succession (see Fig. 1). Output information of the A/D converter enters the on-line storage of the measuring unit and is fed to a check-code former. Data array is set into the computer, along with the check code, on completion of the measurement cycle. A possibility of connecting check signals to the inputs of signal amplifiers is provided for the calibration of transduction channels as well as for the elimination of a measurement-error component caused by level drift and by an amplifier-gain change. The connection of check signals to the inputs of the amplifiers can be accomplished on computer command or with the use of toggle switches on the front panel of the unit. A check of the reactivity-measurement channel is accomplished by applying to the input of the amplifier of the ionization-chamber current a signal which simulates a stepped variation of reactivity by 0.1β (β is an effective delayed-neutron fraction). The operator also specifies, by means of toggle switches the reactivity-balance computation step, the gain of the amplifier of the ionization-chamber current (automatically or by hand) and the parameter which must be read out from the A/D converter output and represented on the binary display of the measuring unit.

The programmable amplifier of the ionization-chamber current has been made on the basis of the direct current amplifier 701ML18 of the microminiature module type. The amplifiers of the output signals of thermoelectric temperature transducers and of magnetic flowmeters have been assembled from operational amplifiers K816UD1G. At the output of each amplifier, there is a rejection filter tuned to 50 Hz.

Computed values of ρ_a , ρ_m , W , and ρ_k can be delivered to a display unit or to recorders through a block of D/A converters. The display unit comprises two decimal digital displays made of light-emitting cells AL304B (number format: mantissa sign, 3-digit mantissa, order sign, 2-digit order). Each display has a switch enabling the operator to specify the computational parameter whose value is to be read out of the computer and represented on the display.

play. The highest possible number of parameters for each display is 20. On the front panel of the display unit, there are also two switches for choosing scale values of recorders in terms of reactivity for readout of values ρ_a and ρ_k .

The D/A converter unit comprises four D/A converters built on the basis of integrated circuit K572PA1A. The data entering the unit from the "Vector" framework channel are checked by comparing the check code formed within the unit when receiving the data with the computer check code. When the check codes are not identical the data are not received by D/A converter registers, and an interrupt signal enters the computer.

The controller provides the communication between the "Vector" framework channel and the Elektronika D3-28 computer, performs the parity check of control words, and generates signals from the functional units of the system. Below is a summary of the basic technical characteristics of the system:

Input current of the amplifier of the
ionization-chamber current, A..... 10^{-10} - 10^{-3}
Signal range of:
thermoelectric temperature transducers, mV.....0-24
magnetic flowmeters, mV.....0-8
safety and control rod-position transducer, V.....0-5
Reactivity-balance computation steps, sec0.2; 0.4; 0.8
Quantity of recorder scale values specified
by the operator before measurements.....9

The CRB system has been on trial operation on the BOR-60 reactor for two years. The tests have shown that the real sensitivity to abnormal reactivity changes in the rated reactor operating conditions is $(1-2) \cdot 10^{-5} \Delta k/k$. The main contribution to the error is the ambiguity of reactivity effects and their variation with time which requires a correction of the coefficients introduced into the system at intervals. In 10 days of reactor operation, the following factors cause nonanomalous reactivity-balance changes, $\Delta k/k$:

Power.....0.4
Temperature at the inlet.....0.6
Coolant-flow rate.....0.3
Reactor dynamics.....0.2
Safety and control rod position.....0.3
Electronic equipment.....0.2

Reactivity changes have been recorded to be as high as $5 \cdot 10^{-5} \Delta k/k$, both quick (seconds) and slow (tens of minutes, hours). An analysis proved the abnormal character of variations, but failed to identify the abnormalities for lack of correlation with the data of the standard monitoring systems due to their relatively low sensitivity. The low variations recorded suggest that there were no such abnormalities as sodium boiling or FA "floating-up" in the reactor. There were nonanomalous reactivity variations, sometimes as high as $(10-15) \cdot 10^{-5} \Delta k/k$, due to big reactor-parameter changes (when the rated power was attained or the reactor was shut down). Against this background, only sufficiently big abnormalities can be detected. To obtain more sensitive and reliable diagnostics of abnormalities, a continuous comprehensive monitoring of the BOR-60 reactor state has been planned, using the noise diagnostics and measurements of thermal and hydraulic characteristics [5] as well as the fuel-element containment monitoring system now in use on the reactor in addition to CRB methods.

LITERATURE CITED

1. V. A. Afanas'ev, V. M. Gryazev, V. N. Efimov, et al., "Diagnostics of the BOR-60 reactor state by the reactivity-balance computation method," At. Énerg., 48, No. 2, 100-101 (1980).
2. "General safety provisions for the atomic power stations in the design and operation of the structures (GSP-82)," At. Énerg., 54, No. 2, 160-161 (1983).
3. B. V. Keadze, V. N. Efimov, and L. A. Adamovskii, "Static error of the reactivity-balance computation," At. Énerg., 43, No. 1, 36-37 (1977).
4. V. A. Kachalin and V. N. Pridachin, "Measurement of the reactivity of nuclear reactors," At. Énerg., 54, No. 5, 365-367 (1983).
5. V. N. Efimov, A. A. Minakov, L. N. Kudryashov, et al., "Assessment of the possibility of diagnosing the local overheating in sodium fast reactors," Preprint NIIAR-43 (608), Dimitrograd (1983).

INFLUENCE OF NEUTRONS ON THE ROTATION OF THE POLARIZATION PLANE OF QUARTZ

I. Kh. Abdukadyrova

UDC 553.621:535.568

In this work we continue the investigations started in [1] on the influence of fast neutrons on the rotation of the polarization plane and the phase state of single crystals of artificially grown quartz; the aim of this work at higher neutron fluences Φ ranging from $6 \cdot 10^{19}$ to $6 \cdot 10^{20} \text{ cm}^{-2}$ is to elucidate the mechanism of reactor-radiation-stimulated change in the crystal structure and to make the measuring limits of the recommended neutron detector more precise and to extend them.

Over the entire range considered, $\Phi = 1 \cdot 10^{18} - 6 \cdot 10^{20} \text{ cm}^{-2}$, the dependence $\Delta\alpha_{sp}/\alpha_{sp}^0 = f(\Phi)$ (Fig. 1) has a complicated form and can be represented by a sigmoid curve with an induction period. The ratio $\Delta\alpha_{sp}/\alpha_{sp}^0 = (\alpha_{sp}^0 - \alpha_{sp}^{irr})/\alpha_{sp}^0$ is the relative change in the rotation of the polarization plane, where α_{sp}^0 and α_{sp}^{irr} are the specific values of the rotation of the polarization plane (per unit thickness) of unirradiated and irradiated crystals, respectively (for $\lambda = 589 \text{ nm}$). Indeed, according to the experimental data, the kinetics of the process by which the crystal loses its ability to rotate the polarization plane at first develops at a very slow rate, then increases sharply, and reaches saturation at $\Phi = (1.3-2) \cdot 10^{20} \text{ cm}^{-2}$; this is consistent with an individual result of [2] and confirms the transition of the substance to the amorphous (metamict [2]) state because $\alpha_{sp} = 0$ and further irradiation of the specimen to $\Phi = 6 \cdot 10^{20} \text{ cm}^{-2}$ does not affect the measured value of the optical signal. A parallel study of the kinetics of the process of rearrangement of the crystal structure of quartz, which was made by measuring x-ray scattering [3] as well as α_{sp} , proved to be very informative because it enabled us to establish the existence of a mirror reflection of both radiation kinetic dependences $\alpha_{sp} = f(\Phi)$ and $I_{1h} = f(\Phi)$ and to reveal the picture of the nucleation and growth of the noncrystalline modification of quartz.

In view of this and the lack of reliable experimental data about the quantitative change in the crystalline modification of quartz during irradiation in a nuclear reactor, we established the following preliminary values on the basis of the α_{sp} values found and assumption about the existence of a two-phase state in neutron-irradiated quartz. For fast-neutron fluences of $(0, 1, 2, 4, 5, 7, 8, 9, 11, \text{ and } 20) \cdot 10^{19} \text{ cm}^{-2}$ the concentration of the crystal-phase in the reactor-irradiated quartz was (in %): 100, 99, 98, 83, 72, 43, 30, 5, 4, 0, respectively. As is seen, the concentration of the crystal phase is a nonmonotonic function of the neutron fluence (this is indicated by the variation of I_{1h} and n_p).

To ascertain the nature of the process of radiation-stimulated transformation of the crystal structure of quartz we carried out a mathematical approximation of the determined behavior of the function $\Delta\alpha_{sp}/\alpha_{sp}^0 = f(\Phi)$. Analysis showed that the entire process of variation of the neutron fluence from $1 \cdot 10^{18}$ to $2 \cdot 10^{20} \text{ cm}^{-2}$ can be divided into three stages, whose kinetic curves are approximated by the power law $N_1 = K_1 \Phi^{t_1}$, where K_1 and t_1 are the

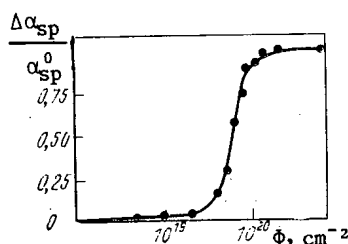


Fig. 1. Influence of fast-neutron fluence on the relative change in the rotation of the polarization plane of crystalline quartz.

Translated from *Atomnaya Energiya*, Vol. 59, No. 5, pp. 381-382, November, 1985. Original article submitted January 28, 1985.

TABLE 1. Results of Neutron-Fluence Measurements by Solid-State (Φ_1) and Threshold (Φ_2) Detectors

Reactor operating regime (No. of cycles)	Power of apparatus, MW	$\Phi_1, 10^{18} \text{ cm}^{-2}$	$\Phi_2, 10^{18} \text{ cm}^{-2}$	Φ_2/Φ_1
2	6	4,9	4,1	0,84
2	10	16	14	0,88
1	10	4,5	4,1	0,91
1	9	9	7	0,80

rate constant of the process and the exponent of the power law for each of the stages, respectively, and N_i is a reduced optical parameter that characterizes the fraction of non-crystalline phase formed. The particular values of the constants can be determined from the experimental relations. The calculations performed led to the following values of the exponent t_i for each stage of irradiation: $t_1 = 0.73$ ($\Phi = 5 \cdot 10^{18} - 2 \cdot 10^{19} \text{ cm}^{-2}$), $t_2 = 2.30$ ($\Phi = 2 \cdot 10^{19} - 9 \cdot 10^{19} \text{ cm}^{-2}$), and $t_3 = 0.07$ ($\Phi = 9 \cdot 10^{19} - 2 \cdot 10^{20} \text{ cm}^{-2}$). As is seen, fairly optimistic relations were obtained between the signal recorded by the detector and the integrated flux of fast neutrons over the entire range of fluence up to $2 \cdot 10^{20} \text{ cm}^{-2}$; this simplifies calibration and enhances the reliability of the given detector.

Thus, simple estimates have shown that $N_1 = K_1 \Phi^{0.7}$, $N_2 = K_2 \Phi^{2.3}$, and $N_3 = K_3 \Phi^{0.1}$ for $i = 1-3$. On the basis of the experimental results obtained and the concrete form of the functions N_i we can hypothesize the existence of an incipient two-stage mechanism of amorphization of the structure. Moreover, the presence of a nearly square-law dependence of $N(\Phi)$ on I_{1h} and ρ in the second stage $\Phi = (4-9) \cdot 10^{19} \text{ cm}^{-2}$ for the radiation effect supports this conclusion and characterizes the feasibility of the formation of a growing nucleus of the amorphous phase near $\Phi = 4 \cdot 10^{19} \text{ cm}^{-2}$.

Besides this we carried out an experiment on the use of a detector to obtain information about the fast-neutron fluence during prolonged continuous operation of the VVR-SM water-moderated-water-cooled reactor at the Institute of Nuclear Physics, Academy of Sciences of the Uzbek SSR for $E \geq 3 \text{ MeV}$ (see Table 1). For comparison, Table 1 gives the values of the fluence that were calculated from the activation integrals that had in turn been obtained on the basis of threshold detectors (^{54}Fe), irradiated simultaneously with plates of α -quartz, for the same neutron energy. The values of Φ_1 and Φ_2 obtained for the corresponding actual conditions of the experiment were very similar. This, together with a number of advantages possessed by the solid-state system, can attest to the advisability of using the solid-state system for prolonged materials-science investigations.

LITERATURE CITED

1. I. Kh. Abdukadyrova and A. A. Fotchenkov, *At. Energ.*, **52**, No. 3, 180 (1982).
2. W. Primak, *Phys. Rev.*, **110**, 1240 (1958).
3. I. Kh. Abdukadyrova, N. N. Mukhtarova, and L. K. Panfilova, in: *Influence of Structural Imperfections on the Properties of Crystals* [in Russian], Branch of the Academy of Sciences of the USSR, Tashkent (1979), pp. 64-69.

PLUTONIUM CONTENT OF SOILS IN THE SOVIET UNION

F. I. Pavlotskaya, Z. M. Fedorova,
V. V. Emel'yanov, B. F. Myasoedov,
and I. G. Vodovozova

UDC 546.799.4:631.41

With the further development of nuclear power and of environmental protection, increasing attention is being given to the assessment of the radiation situation caused by the presence of plutonium, whose long-lived nuclides are among the most significant from the biological standpoint [1]. It is important to know the background concentrations of plutonium on the earth's surface due to global radioactive fallout resulting from the conduct of experimental nuclear explosions and the crashes of air or space vehicles carrying nuclear power units [2, 3]. Data on the plutonium content of soils in a number of countries are known today [2-17]. The purpose of the present study is to obtain similar information for the soils of the Soviet Union.

Specimens of a number of types of virgin soil were collected in July and August of 1982 in open areas down to a depth of 15 cm. The plutonium content was determined by a radiochemical method [18], using 50-g weights of soil; the radioactivity was measured by means of a low-background alpha flow counter (counting efficiency was about 43%, and the background was 0.07 ± 0.017 pulses per minute) and an ionization chamber containing a circuit with a 500-channel LP-4050 analyzer (counting efficiency 32%, background $9.8 \cdot 10^{-3}$ pulses per minute at a threshold of 100 keV and a peak of 5 MeV). The detection limit was $1.7 \cdot 10^{-3}$ Bq.

The average specific activity of ^{239}Pu and ^{240}Pu in the soils of the Soviet Union was 1.15 Bq/kg of air-dried mass, or 188 Bq/m². The average and limiting values obtained for the plutonium concentration in the surface levels of USSR soils are close to the data for other Northern-Hemisphere countries (see Table 1). This indicates that the contamination of the soil cover originates in global radioactive fallout.

We found that the plutonium content of the soils and its distribution are influenced by a number of natural factors: location, type of soil and genetic structure of the soil profile, type of vegetation, etc. Thus, like the thoroughly studied nuclides of strontium and cesium [19], the minimum amount of plutonium was found on slopes, a higher amount in watersheds and low-lying parts of the landscape (the profile extended about 40 m). In soils with a thick layer of turf and occasional growths of gramineous plants the maximum plutonium content is observed in the soil layer down to a depth of 3 (5) cm. If there are no such growths and the turf is not strongly developed, the plutonium becomes concentrated in the upper part of the humus layer.

Thus, taking account of the influence of natural factors on the amount and distribution of plutonium in soils, we must ascertain the laws governing the behavior of this element under specific landscape and geological conditions and take them into consideration in assessing the radiation situation.

TABLE 1. ^{239}Pu and ^{240}Pu Content of the
Soils of Northern-Hemisphere Countries

Country	Activity		Source
	Bq/kg	Bq/m ²	
USSR	0.55-2.67	74-414	Present study data
FRG	0.23-1.45	—	[14]
Denmark	—	23-67	[5]
Italy	0.59-2.37	159-537	[6]
Austria	0.23-6.73	44-566	[12]
Japan	0.14-1.80	55-131	[17]
USA	—	63-192	[8-11, 13]

Translated from *Atomnaya Energiya*, Vol. 59, No. 5, pp. 382-383, November, 1985. Original article submitted March 20, 1985.

1. Ionizing Radiation: Sources and Biological Effects of Atomic Radiation, 1982. Report to the General Assembly, United Nations, New York (1982).
2. R. Perkins and C. Thomas, in: Transuranic Elements in the Environment, Techn. Inform. Center/US DOE, Springfield (1980), pp. 53-82.
3. F. I. Pavlotskaya and G. G. Polikarpov, in: Achievements of Science and Technology. Radiation Biology. Vol. 4. Problems of Radioecology [in Russian], VINITI, Moscow (1983), pp. 99-141.
4. F. I. Pavlotskaya and B. F. Myasoedov, Radiokhimiya, 26, No. 4, 554-567 (1984).
5. A. Aarkrog and J. Lippert, Environmental Radioactivity in Denmark, 1976, Riso Report, No. 361 (1977).
6. M. De Bortoli and P. Gaglione, Health Phys., 17, No. 5, 701-710 (1963).
7. A. Brondi, R. Cigna, A. Pirini, et al., in: Third Int. Symp. Proc.: Radiol. Prot. - Adv. Theory and Pract., Inverness, 6-11 June 1982, Berkley (1982), Vol. 1, pp. 99-105.
8. R. Dahlman, C. Garten, and T. Hakonsen, in: Transuranic Elements in the Environment, Techn. Inform. Center/US DOE, Springfield (1980), pp. 371-380.
9. E. Hardy, P. Krey, and H. Volchok, HASL-257 (1972), p. 95.
10. J. Harley, J. Radiat. Res., 21, No. 1, 83-104 (1980).
11. M. Hume and C. Telsly, Trans. Am. Nucl. Soc., 33, 166-167 (1979).
12. K. Irlweek and F. Steger, RZh Radiats. Biol. (1978), 7.70.261.
13. H. McLendon, Health Phys., 28, No. 4, 347-354 (1975).
14. M. Pimpl and H. Schüttelkopf, Kernforschungszentrum Karlsruhe, Project Nucleare Sicherheit, KfK-2891 (1979).
15. R. Waters, D. Edgington, T. Hakonson, et al., in: Transuranic Elements in the Environment, Techn. Inform. Center/US DOE, Springfield (1980), pp. 1-44.
16. M. Yamamoto, K. Komura, and M. Sakanoue, J. Radiat. Res., 24, No. 3, 237-249 (1983).
17. A. Yamamoto, O. Narita, Y. Katahara, et al., in: Transuranic Elements in the Environment, Techn. Inform. Center/US DOE, Springfield (1980), pp. 489-494.
18. F. I. Pavlotskaya, T. A. Goryachenkova, Z. M. Fedorova, et al., Radiokhimiya, 26, No. 4, 460-467 (1984).
19. F. I. Pavlotskaya, "Forms of occurrence and migration of radioactive products of global fallout in soils," Author's Abstract of a Dissertation in partial fulfillment of the requirements for the degree of Doctor of Chemical Sciences, V. I. Vernadskii Institute of Geochemistry and Analytical Chemistry, Moscow (1981).

TLD MONITORING OF EMERGENCY GASEOUS FISSION PRODUCT DISCHARGES FROM NUCLEAR POWER PLANTS

I. A. Bochvar, T. I. Gimadova,
A. A. Drozdov, I. B. Keirim-Markus,
V. A. Kiyazev, and N. A. Sergeeva

UDC 539.1:535.377

A major task in emergency dosimetry at nuclear power plants is to measure discharges of radioactive gases and aerosols through the stack. In emergency situations, rapid discharge estimation provides valuable information on the scale of the emergency and the radiation hazards.

A simple method is to determine discharges by TLD, which was suggested in 1975 by V. A. Knyazev at the Kurchatov Atomic Energy Institute. A similar method was developed later [1] for monitoring radioactive air discharges from high-energy proton accelerators.

Since 1975, we have made measurements on the VVR-2 [2] by using IKS TLD [3]. Ten detectors of diameter 8 mm and height 1 mm made of IS-7 glass were arranged around the diameter of the extraction stack of diameter 0.8 m and height 41 m at the level of 20 m, for which purpose a special hole was made in the chimney wall. The detectors were in cassettes sealed into polyethylene film jackets and were placed at various distances apart. The IKS dosimeter readings decline slightly with time, for which corrections can be applied [4], which enabled us to expose them for 12 ± 2 months. At the end of the exposure, the detectors were extracted, and measurements were made with an IKS-A instrument. Table 1 compares the data with the annual discharge from the stack as measured independently from the readings of DBG-1 detectors and from dosimetric and technological monitoring of Sistema type [5].

Table 1 shows that the γ -ray dose due to radionuclide discharge is 30-270 mGy (mean error of measurement about 10%), which is 20-300 times larger than the doses due to the natural radiation background, which were 1.0-1.5 mGy during the exposure. Error in discharge determination about 30%. The ratios of the measured doses to the discharges were close to the mean value of 1 fGy/Bq within the error limits. In an emergency, one can record the dosimeter readings directly and use the coefficient to determine approximately the total activity discharged into the atmosphere. The IKS dosimeters can measure up to 10 kGy [3], which in this particular case provides for determining discharge activities up to 10 EBq (10^8 Ci), where the routine apparatus may go off scale.

These results were obtained under normal working conditions with the γ -emitting radionuclides normally occurring. In emergency situations, the discharges may be enriched in short-lived nuclides, and the ratio of dose to discharge may be different. This coefficient needs to be refined by the use of emergency gas-aerosol radionuclide mixtures.

TABLE 1. Radioactive Gas Discharge Measurements

Year	Discharge TBq/y	γ -ray dose, mGy/y	Ratio of dose to discharge, fGy/Bq
1975	21 ± 6	31 ± 7	1.5 ± 0.8
1976	55 ± 16	46 ± 7	0.8 ± 0.4
1977	74 ± 22	45 ± 5	0.6 ± 0.3
1978	50 ± 15	36 ± 4	0.7 ± 0.3
1979	44 ± 13	39 ± 3	0.9 ± 0.3
1980	24 ± 7	29 ± 3	1.2 ± 0.5
1981	140 ± 40	170 ± 20	1.2 ± 0.5
1982-1983	200 ± 60	270 ± 30	1.4 ± 0.5
Mean	—	—	1.0 ± 0.4

Translated from Atomnaya Energiya, Vol. 59, No. 5, pp. 383-384, November, 1985. Original article submitted May 8, 1985.

In addition to use on the stack, the IKS detectors of size $15 \times 15 \times 4$ mm were exposed on the balconies of houses at various distances from the stack in the direction of the prevailing winds. In all the years examined, we found no difference between the measured values and the dose level previously known for the locality within the errors of measurement.

LITERATURE CITED

1. J. Tuyn, "Radiation protection monitoring around high energy photon accelerators using thermoluminescence dosimeters," Radiat. Protect. Dosimetry, 2, No. 2, 69-74 (1982).
2. Yu. G. Nikolaev, "An experimental nuclear reactor using light water and enriched uranium," in: Proceedings of the International Conference on the Peaceful Uses of Atomic Energy [in Russian], Vol. 2, Izd. Akad. Nauk SSSR, Moscow (1955), p. 461.
3. I. A. Bochvar, T. I. Gimadova, and I. B. Keirim-Markus, IKS Dosimetry Methods [in Russian], Atomizdat, Moscow (1977).
4. I. A. Bochvar, T. I. Gimadova, and I. B. Keirim-Markus, "The decay of IKS dosimeter readings on storage after irradiation," Prib. Tekh. Éksp., No. 6, 34 (1978).
5. B. V. Nemirovskii et al., "Multichannel radiation monitors of the Sistema 8004-01 type," in: Experimental and Repair Equipment for Measuring Ionizing Radiation [in Russian], Atomizdat, Moscow (1972).

CHANGING YOUR ADDRESS?

In order to receive your journal without interruption, please complete this change of address notice and forward to the Publisher, 60 days in advance, if possible.

(Please Print)

Old Address:

name

address

city

state (or country)

zip code

New Address

name

address

city

state (or country)

zip code

date new address effective

name of journal

THE LANGUAGE OF SCIENCE
Plenum
PUBLISHING CORPORATION

233 Spring Street, New York, New York 10013

MEASUREMENT TECHNIQUES

Izmeritel'naya Tekhnika
Vol. 27, 1984 (12 issues) \$520

MECHANICS OF COMPOSITE MATERIALS

Mekhanika Kompozitnykh Materialov
Vol. 20, 1984 (6 issues) \$430

METAL SCIENCE AND HEAT TREATMENT

Metallovedenie i Termicheskaya Obrabotka Metallov
Vol. 26, 1984 (12 issues) \$540

METALLURGIST

Metallurg
Vol. 28, 1984 (12 issues) \$555

PROBLEMS OF INFORMATION TRANSMISSION

Problemy Peredachi Informatsii
Vol. 20, 1984 (4 issues) \$420

PROGRAMMING AND COMPUTER SOFTWARE

Programmirovaniye
Vol. 10, 1984 (6 issues) \$175

PROTECTION OF METALS

Zashchita Metallov
Vol. 20, 1984 (6 issues) \$480

RADIOPHYSICS AND QUANTUM ELECTRONICS

Izvestiya Vysshikh Uchebnykh Zavedenii, Radiofizika
Vol. 27, 1984 (12 issues) \$520

REFRACTORIES

Ogneupory
Vol. 25, 1984 (12 issues) \$480

SIBERIAN MATHEMATICAL JOURNAL

Sibirskii Matematicheskii Zhurnal
Vol. 25, 1984 (6 issues) \$625

**SOIL MECHANICS AND
FOUNDATION ENGINEERING**

Osnovaniya, Fundamenty i Mekhanika Gruntov
Vol. 21, 1984 (6 issues) \$500

SOLAR SYSTEM RESEARCH

Astronomicheskii Vestnik
Vol. 18, 1984 (6 issues) \$365

SOVIET APPLIED MECHANICS

Prikladnaya Mekhanika
Vol. 20, 1984 (12 issues) \$520

SOVIET ATOMIC ENERGY

Atomnaya Energiya
Vols. 56-57, 1984 (12 issues) \$560

**SOVIET JOURNAL OF GLASS PHYSICS
AND CHEMISTRY**

Fizika i Khimiya Stekla
Vol. 10, 1984 (6 issues) \$235

**SOVIET JOURNAL OF
NONDESTRUCTIVE TESTING**

Defektoskopiya
Vol. 20, 1984 (12 issues) \$615

SOVIET MATERIALS SCIENCE

Fiziko-khimicheskaya Mekhanika Materialov
Vol. 20, 1984 (6 issues) \$445

SOVIET MICROELECTRONICS

Mikroelektronika
Vol. 13, 1984 (6 issues) \$255

SOVIET MINING SCIENCE

*Fiziko-tekhnicheskie Problemy Razrabotki
Poleznykh Iskopaemykh*
Vol. 20, 1984 (6 issues) \$540

SOVIET PHYSICS JOURNAL

Izvestiya Vysshikh Uchebnykh Zavedenii, Fizika
Vol. 27, 1984 (12 issues) \$520

**SOVIET POWDER METALLURGY AND
METAL CERAMICS**

Poroshkovaya Metallurgiya
Vol. 23, 1984 (12 issues) \$555

STRENGTH OF MATERIALS

Problemy Prochnosti
Vol. 16, 1984 (12 issues) \$625

THEORETICAL AND MATHEMATICAL PHYSICS

Teoreticheskaya i Matematicheskaya Fizika
Vol. 58-61, 1984 (12 issues) \$500

UKRAINIAN MATHEMATICAL JOURNAL

Ukrainskii Matematicheskii Zhurnal
Vol. 36, 1984 (6 issues) \$500

Send for Your Free Examination Copy

Plenum Publishing Corporation, 233 Spring St., New York, N.Y. 10013

In United Kingdom: 88/90 Middlesex St., London E1 7EZ, England

Prices slightly higher outside the U.S. Prices subject to change without notice.

RUSSIAN JOURNALS IN THE PHYSICAL AND MATHEMATICAL SCIENCES

AVAILABLE IN ENGLISH TRANSLATION

ALGEBRA AND LOGIC

Algebra i Logika
Vol. 23, 1984 (6 issues) \$360

ASTROPHYSICS

Astrofizika
Vol. 20, 1984 (4 issues) \$420

AUTOMATION AND REMOTE CONTROL

Avtomatika i Telemekhanika
Vol. 45, 1984 (24 issues) \$625

COMBUSTION, EXPLOSION, AND SHOCK WAVES

Fizika Goreniya i Vzryva
Vol. 20, 1984 (6 issues) \$445

COSMIC RESEARCH

Kosmicheskie Issledovaniya
Vol. 22, 1984 (6 issues) \$545

CYBERNETICS

Kibernetika
Vol. 20, 1984 (6 issues) \$445

DIFFERENTIAL EQUATIONS

Differentsial'nye Uravneniya
Vol. 20, 1984 (12 issues) \$505

DOKLADY BIOPHYSICS

Doklady Akademii Nauk SSSR
Vols. 274-279, 1984 (2 issues) \$145

FLUID DYNAMICS

Izvestiya Akademii Nauk SSSR, Mekhanika Zhidkosti i Gaza
Vol. 19, 1984 (6 issues) \$500

FUNCTIONAL ANALYSIS AND ITS APPLICATIONS

Funktsional'nyi Analiz i Ego Prilozheniya
Vol. 18, 1984 (4 issues) \$410

GLASS AND CERAMICS

Steklo i Keramika
Vol. 41, 1984 (6 issues) \$590

HIGH TEMPERATURE

Teplofizika Vysokikh Temperatur
Vol. 22, 1984 (6 issues) \$520

HYDROTECHNICAL CONSTRUCTION

Gidrotekhnicheskoe Stroitel'stvo
Vol. 18, 1984 (12 issues) \$385

INDUSTRIAL LABORATORY

Zavodskaya Laboratoriya
Vol. 50, 1984 (12 issues) \$520

INSTRUMENTS AND EXPERIMENTAL TECHNIQUES

Pribory i Tekhnika Eksperimenta
Vol. 27, 1984 (12 issues) \$590

JOURNAL OF APPLIED MECHANICS AND TECHNICAL PHYSICS

Zhurnal Prikladnoi Mekhaniki i Tekhnicheskoi Fiziki
Vol. 25, 1984 (6 issues) \$540

JOURNAL OF APPLIED SPECTROSCOPY

Zhurnal Prikladnoi Spektroskopii
Vols. 40-41, 1984 (12 issues) \$540

JOURNAL OF ENGINEERING PHYSICS

Inzhenerno-fizicheskii Zhurnal
Vols. 46-47, 1984 (12 issues) \$540

JOURNAL OF SOVIET LASER RESEARCH

A translation of articles based on the best Soviet research in the field of lasers
Vol. 5, 1984 (6 issues) \$180

JOURNAL OF SOVIET MATHEMATICS

A translation of Itogi Nauki i Tekhniki and Zapiski Nauchnykh Seminarov Leningradskogo Otdeleniya Matematicheskogo Instituta im. V. A. Steklova AN SSSR
Vols. 24-27, 1984 (24 issues) \$1035

LITHOLOGY AND MINERAL RESOURCES

Litologiya i Poleznye Iskopaemye
Vol. 19, 1984 (6 issues) \$540

LITHUANIAN MATHEMATICAL JOURNAL

Litovskii Matematicheskii Sbornik
Vol. 24, 1984 (4 issues) \$255

MAGNETOHYDRODYNAMICS

Magnitnaya Gidrodinamika
Vol. 20, 1984 (4 issues) \$415

MATHEMATICAL NOTES

Matematicheskie Zametki
Vols. 35-36, 1984 (12 issues) \$520

continued on inside back cover